



METASENSING

**Technical Assistance for the Development and
Deployment of an X- and Ku- Band
MiniSAR Airborne System**

Final Report

Contract no.: 4000101697/10/NL/FF/ef

Doc. No.: MS-Snowsar-D7

Issue: 2.0

Date: 5th September 2011

Authors:

Christian Trampuz

Alex Coccia

Ernesto Imbembo

Approved:

Adriano Meta



Fig. 1: SnowSAR in action during the measurement campaign in Finland, March 2011. The typical Lappish landscape can be appreciated.

Index

1	Introduction	4
1.1	Outline of the report.....	4
2	Background	5
2.1	Instrumentation test.....	6
3	Corner reflectors	12
3.1	Physical description	13
3.2	Electrical characterization.....	14
4	Measurement campaign in Finland	20
4.1	Corner reflectors deployment	21
4.2	SnowSAR antennae configuration.....	23
5	Radiometric calibration	25
5.1	Internal calibration	25
5.1.1	Temperature monitoring	25
5.1.2	Transmitted power tracking	26
5.1.3	Receiving gain tracking	31
5.2	External calibration.....	32
5.2.1	Antenna characterization	32
5.2.2	Elevation plane pattern	33
5.2.3	Azimuth plane pattern.....	34
6	Error analysis	38
6.1	Aircraft attitude.....	38
6.2	Antenna pattern.....	39
6.2.1	Elevation plane.....	40
6.2.2	Azimuth plane.....	44
6.2.3	Systematic error from DEM inaccuracy	48
7	Data take initial analysis	54
7.1	General considerations.....	54
7.2	Data take example.....	56
7.2.1	DEM knowledge	57
7.3	Signal-to-Noise Ratio.....	58
7.4	First calibration analysis on VV at Ku-band.....	58

8	Technical performance	61
8.1	Radiometric performance.....	61
8.2	Geometric performance	63
8.3	Performance summary	64
9	Conclusions.....	66
9.1	Lessons learned.....	67
10	References.....	69

1 Introduction

In the framework of its Earth Observation Envelope Programme, the European Space Agency (ESA) has commissioned to MetaSensing the development of a dual frequency, X- and Ku-bands, dual polarization mini-SAR airborne system (SnowSAR) and its deployment within an ESA-coordinated campaign in support of the candidate Earth Explorer mission CoReH2O (Cold Regions Hydrology High-Resolution Observatory).

The present document represents the Final Report of the project, describing the results of the SnowSAR airborne campaign which has been performed in the Lappish region of Finland between the 12th and the 19th of March 2011. It includes details about campaign execution, information on data acquisition and data processing, and a preliminary analysis of results.

1.1 Outline of the report

Besides this first introductory section, the document is structured as follows. Chapter 2 represents a background survey of the project, giving an overview of the already available documentation about technical assistance for the SnowSAR development and deployment. In chapter 3 the corner reflectors used for calibration purposes during the testing phase and during the measurement campaign are described in detail. Chapter 4 characterizes the SnowSAR measurement campaign, showing the corner reflectors deployment and the radar and GPS antennae configurations on board of the airplane. Chapter 5 describes the main factors to take into account within the SnowSAR image calibration process. In chapter 6 an error analysis is performed, relatively to the uncertainty about the aircraft attitude determination and about the antenna pattern reconstruction. In chapter 7 an initial data take analysis is presented. In chapter 8 the technical performance of the SnowSAR is given, as result of the Finnish measurement campaign. In chapter 9 the conclusions are drawn, together with some important lesson learnt.

2 Background

As documented in the Statement of Work (SoW) document [1], main objective of the project is the provision of radiometric calibrated airborne SAR data needed to characterize the backscattering signatures of snow and other terrain types (e.g. trees). The aim is testing theoretical backscatter models and validating retrieval algorithms to support the Earth Explorer mission CoReH₂O. In order to obtain this, different work-packages have been executed by MetaSensing in the last months, as briefly summarized and/or referenced in the following.

In [2] the preliminary design of the SnowSAR instrument is described in detail, analyzing its different subsystems, including antennae, digital part and RF part. Also information about complementary subsystems like navigation (GPS-IMU) and cooling unit (Peltier module) are given, together with a basic description of the chosen aircraft and of the adopted corner reflectors. The procedures for testing the sensor itself are also included in the document.

After the design of the SnowSAR has completed, a full-testing phase has followed, including bench tests of sub-system and test flight campaigns for global assessment of the SnowSAR system. Both testing procedures have been documented in two presentations already delivered to the Agency. In the next section 2.1 they are briefly summarized for convenience of the reader.

In [3] an overview of the experiment implementation plan is given, together with a draft report of the flight campaign in Lapland. In particular the installation of the SnowSAR system within the chosen aircraft is described. The operational area over the site of Sodankyla has been delineated: the adopted flying trajectories during the campaign are shown in relation to the ground measurements which were simultaneously taken. A record of the accomplished actions-achievements during the campaign is listed on a daily basis.

2.1 Instrumentation test

The SnowSAR and all its main single components passed the testing phase in the MetaSensing labs, during December 2010 - January 2011. The digital subsystem, the DC power supply unit, the RF subsystem: each of these subsystems has been individually tested before being integrated and assembled into the rack.

Besides conventional bench tests, particular attention has been paid to the calibration and radiometric stability of the instrument, peculiar characteristics among the SnowSAR requirements.

Figure 2 shows a screenshot taken during an internal calibration monitoring phase. The waveform on the top shows the noise floor as measured by the power meter, while the waveform on the bottom shows the power of the calibration chain. Good power stability is achieved in operational conditions.

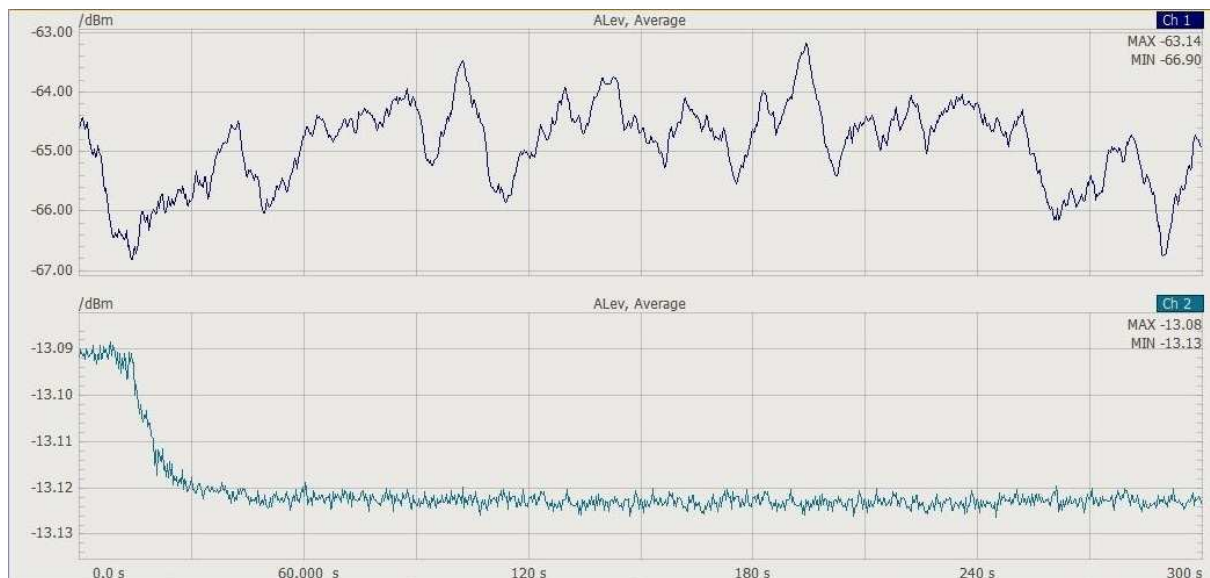


Fig. 2: Internal calibration monitoring of the SnowSAR, by mean of power meter measurements: top, noise floor; bottom, calibration chain, over an observation period of 5 minutes.

Once all the bench tests have been successfully completed, the system has been integrated and assembled in its rack. Figure 3 shows the SnowSAR sensor in its final embodiment. The RF subsystem is positioned on the bottom stage, where the Peltier cooling/heating module can be appreciated. On the top stage the digital subsystem is cooled by a double fan system.



Fig. 3: The SnowSAR sensor, ready for the Finnish campaign.

Following the SnowSAR system assembly and laboratory testing, a measurement campaign in the air has been planned with the system integrated on the aircraft, to test the SnowSAR overall performance with respect to the initial requirements.

The flight tests have been performed in Teuge, The Netherlands, base of the selected company supplying the airborne platform, a Cessna 208 Grand Caravan, see Figure 4. Main reasons for this choice include the availability of a wide cargo door behind which mounting the SnowSAR antennae, and of instrumentation equipment allowing flying even in low vision and in icing conditions.



Fig. 4: SnowSAR airborne platform, a Cessna 208 Grand Caravan from the National Paracentrum Teuge.

The test measurement campaign has been performed during the second week of February 2011. Different issues have been checked, as listed in the following.

- Antenna mounting structure. Vibrations have been noticed during taking off at the Lexan protecting door, making the antennae instable. Improvements have been implemented after the first flight in terms of antenna support position re-arrangement.
- Temperature and humidity tracking. While in a laboratory environment the Peltier element was considered under-dimensioned to keep temperature constant, in operational airborne conditions the situation is much better due to a lower environment temperature. The resulting internal temperature was nearly constant during the entire flight acquisitions, around 28° C.
- Transmitted power tracking. The transmitted power for both the polarizations is tracked by means of 2 power meters, one per each frequency band. Every four seconds, each power meter switches between polarization amplifiers. The two polarization channels have different attenuation values in the chain (around 13 dB difference), so that an unequivocal discrimination is possible among the two signals during the post-processing phase.

Figure 5 shows the output amplifier power (through a 30 dB coupler) for the X-band subsystem within two different acquisitions (left and right sub-plots), for the two polarizations (top and bottom sub-plots); the same testing device (power meter) has been used for the measurements of the two polarizations, by switching channel every 4 seconds. A very stable (variation within 0.02 dB) and repeatable transmitted power is shown.

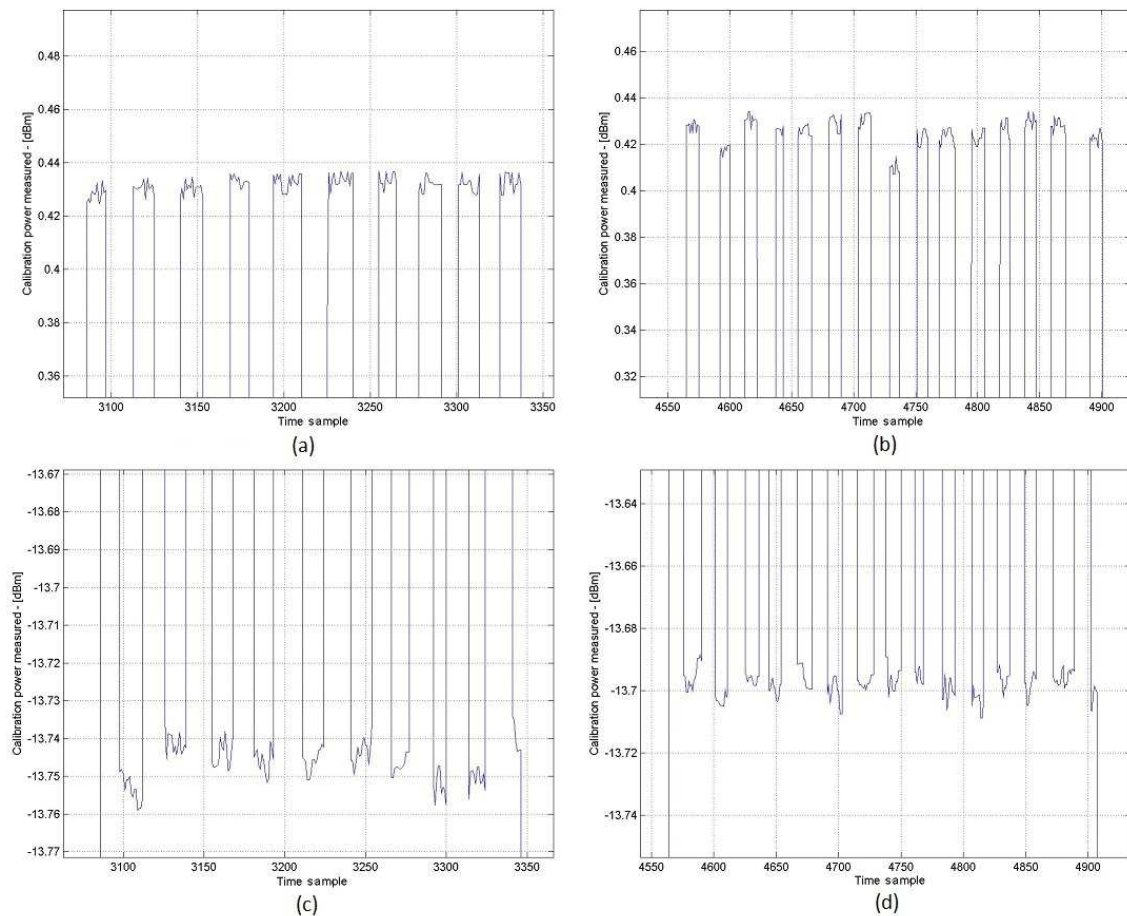


Fig. 5: SnowSAR tests, X-band subsystem: transmitted power tracking: (a) vertical polarization, acquisition 1; (b) vertical polarization, acquisition 2; (c) horizontal polarization, acquisition 1; (d) horizontal polarization, acquisition 2. See section 5.1.2 for further details about power measurements.

Figure 6 shows the output amplifier power (through a 30 dB coupler) for the Ku-band subsystem, within two different acquisitions (left and right sub-plots), for the two polarizations (top and bottom sub-plots). Ku-band amplifier shows a power drop after beginning the acquisition presumably due to the component stabilization after starting-up. However after the first seconds the drop is well behaved and keeps below

0.2 dB variation. It has been understood that Ku band transmitted power can potentially be reduced of 1 dB to bring the power amplifier farther away from the 1 dB compression point.

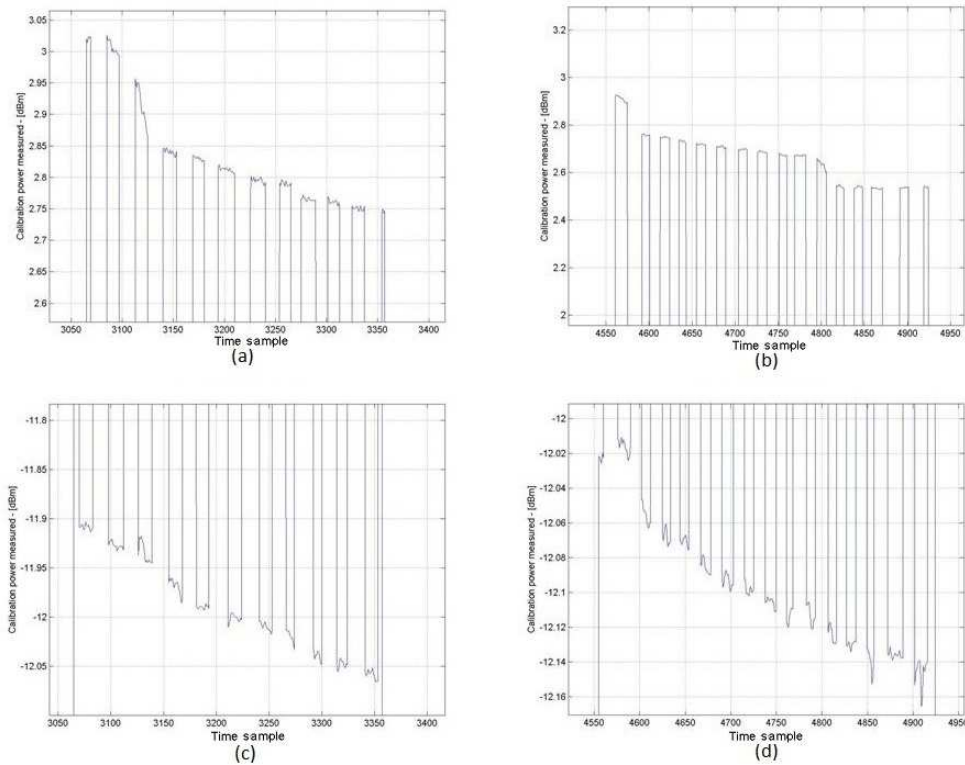


Fig. 6: SnowSAR tests, Ku-band subsystem, transmitted power tracking in two different acquisitions: (a) vertical polarization, acquisition 1; (b) vertical polarization, acquisition 2; (c) horizontal polarization, acquisition 1; (d) horizontal polarization, acquisition 2.

- Several spurious peaks have been localized in the power range profiles, deteriorating the acquired images. By changing power supply configuration the problem has been solved.
- The potential problem of interference between X- and Ku-bands antennae has been solved by introducing in both the receiving chains a band-pass filter removing out-of-band noise. Different antenna configurations have been tested and their performance compared in terms of phase noise levels originating from the antennae coupling of the same band. The final configuration has been chosen based on empirical data.

After the testing phase it has been concluded that the SnowSAR system's behavior is stable in terms of transmitted power and temperature. System synchronization has worked properly. Polarization switching, waveform generation, GPS marker generation and data acquisition was ok. The GPS acquisition performed properly. Radar data recorded properly. No data loss observed when acquiring the 4 channel and two polarizations simultaneously. Figure 7 shows the first SnowSAR unfocused images from the test campaign, relative to both the frequency bands. On the right part of the plot the runways of the Teuge airport can be noticed, with the four corner reflectors placed in a line, see Figure 9.

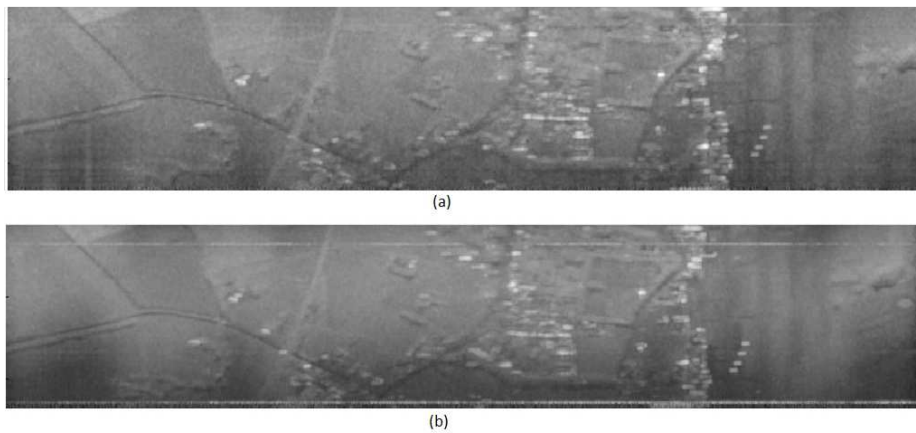


Fig. 7: First SnowSAR un-focused images from the test campaign: a strip of about 2200 meters per 200 meters over the airport of Teuge is represented. The four corner reflectors used for calibration can be pointed out on the right part of the plot. (a) X-band, (b) Ku-band.

3 Corner reflectors

The radiometric calibration represents an important requirement for the SnowSAR system. Radar calibration is needed when absolute measurements of one or more characteristics of the observed scenery are of interest. In the calibration process of a radar system, the digital values of a remotely sensed image are related to physical quantities of the observed scene, such as for example reflectivity, phase and location. By means of radiometric calibration, a relationship between radar backscatter and geophysical parameters can be properly established.

For the SnowSAR system, the absolute value of the reflectivity from the monitored scenarios has been calibrated. To this end, a number of targets with a strong and well-known response (i.e. corner reflectors) has been used. Among possible strong reflectors, a trihedral reflector is a passive radar calibration device, composed of three flat surfaces of a specific shape (square, triangular, circular), and arranged to form a corner with the sides intersecting at 90 °. Such a device is commonly used to calibrate signal strengths in radar surveys or to check the location of specific points in the processed image. For purposes of radar calibration, MetaSensing has fabricated and deployed on the field across the swath 4 trihedral reflectors, which are characterized in the following paragraphs.

In particular the electrical characterization of the adopted corner reflectors has been performed by means of an FDTD-based numerical electromagnetic method, which, in view of its Cartesian orthogonal mesh, is extremely suited and accurate for determining the RCS of the objects at hand. Simulation results are discussed in section 3.2. The in-flight antenna pattern is reconstructed from measured data, based on the known position and response of the trihedral reflectors.

3.1 Physical description

The shape of the reflecting faces is chosen square, in order to maximize the RCS response for a certain given side size. This comes at the cost of a slightly narrower angular response of the reflector, a triangular side giving a broader angular response. The fabricated reflectors are made of 1 cm thick aluminum, providing a good trade off between weight and robustness.

The side of the square face is 30 cm long, resulting in a RCS in excess of 20 dBm² at X-band and of 25 dBm² at Ku-band. The total weight of each reflector is 7.8 Kg. In Figure 8 a square-faced trihedral reflector is simulated, as the ones used during the campaign. For convenience the adopted reference system is also indicated.

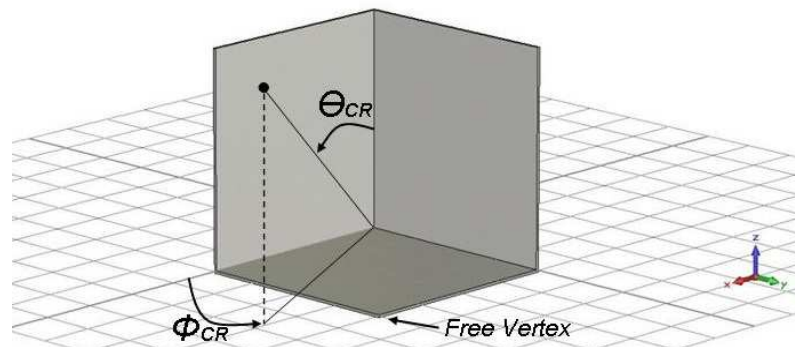


Fig. 8: Simulated trihedral corner reflector with square faces and relative coordinate system (θ elevation, Φ azimuth angles; the subscript CR means Corner Reflector). The free vertex (corresponding to the vertex at $\Phi_{CR}=45^\circ$) has been used to orient the reflectors during their deployment (see section 3.3). In the remaining of this document for “nose-up” is intended a rotation of the corner reflector free vertex in the negative sense of θ .

In Figure 9 the adopted corner reflectors are shown in an operational scenario (test campaign in Teuge).



Fig. 9: Square-faced trihedral corner reflectors adopted for SnowSAR calibration: deployment during the test measurement campaign of the SnowSAR in Teuge, The Netherlands, February 2011.

3.2 Electrical characterization

For a proper calibration of the acquired radar data, the RCS of the trihedral corner reflectors must be accurately characterized for:

- both the operative frequencies of the mission (9.6 GHz and 17.25 GHz) and in the operative bands (+/- 50 MHz about the central frequencies above specified);
- both vertical and horizontal polarizations, as applicable for the mission;
- a number of illumination angles of interest, based on the relative positions and orientation between the antenna system on the aircraft and the corner reflectors on the ground.

To this end, a numerical solver based on the finite-difference time-domain (FDTD) method is employed. In this software, the orthogonal Cartesian mesh grid and the flexibility in the parametric definition of quantities relative to the electromagnetic problem at hand allow an accurate analysis (better than 0.08 dB of RCS accuracy) of the corner reflectors, maintaining the computational domain manageable.

Considering the relative position and orientation of the corner reflectors on the ground with respect to the antenna system on-board the aircraft, a characterization of the RCS of the reflectors across the whole frontal domain ($0^\circ < \theta_{CR} < 90^\circ$, $0^\circ < \Phi_{CR} < 90^\circ$, see Figure 9) is not regarded as necessary. By narrowing the angular domain of interest, the simulation time can be reduced drastically, without affecting the results of interest.

Consequently, the RCS investigation can be limited to a narrower angular region. In view of the relative orientation corner reflectors - antenna system, the range of investigated solid angles is $33.5^\circ \leq \theta_{CR} \leq 47.5^\circ$, $25^\circ \leq \Phi_{CR} \leq 65^\circ$, with an angular step of 1° , for a total number of 615 angular directions of illumination. For angles in between two calculated grid points, the RCS value may be interpolated, since the RCS is a slowly varying function of the illuminating angle and the grid if well refined.

Fig. 10, shows, for each central frequency of the two bands of interest (9.60 GHz and 17.25 GHz for the X- and the Ku-band, respectively) the trihedral reflector RCS variation with the illumination angle, for the angles of interest.

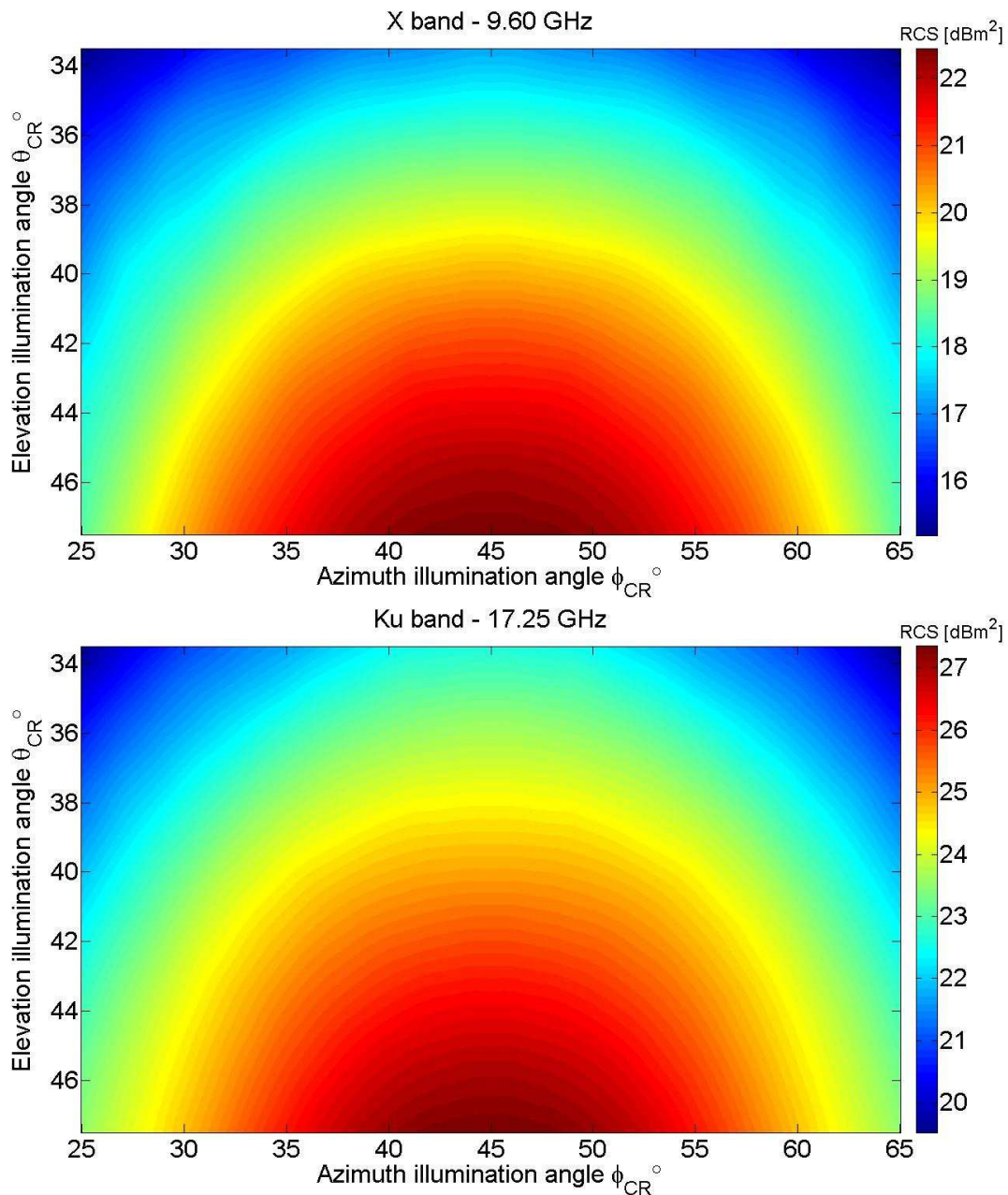


Fig. 10: Adopted trihedral corner reflector: simulated Radar Cross Section (RCS) in the angular range of interest, for the X- and for Ku-bands, respectively on top and bottom plots.

A similar behavior of the RCS as a function of the illuminating angle can be observed at the two considered frequencies. It is to be noted, however, how the absolute RCS values change for the two cases. As proved by Figure 10, the RCS of a target is a function of the operating frequency [4]. In particular, for a given target, the RCS value grows up by increasing the operating frequency. Since the SnowSAR system transmits a 100 MHz bandwidth, an evaluation study has been performed, to assess the approximation error in assuming the RCS of the reflectors as the one calculated for the central frequency instead of considering it over the entire transmitted bandwidth.

In Figure 11 the differences between the RCS values of the corner reflector calculated at two different punctual frequencies are shown: in particular, in the top subplot the RCS value calculated at the central frequency (9.6 GHz) of the transmitted bandwidth (100 MHz) and the RCS value calculated at the lower extreme (9.55 GHz) of the transmitted bandwidth are compared (subtracted) for the X-band case. Similarly, on the bottom subplot the higher extreme (9.65 GHz) is considered. Because RCS variations below 0.07 dB are observed across both half transmitted bandwidths (similar results are obtained at the Ku-band) it can be considered fair the above mentioned assumption of considering the RCS of the corner reflector as the one calculated for the central frequency of the transmitted bandwidths.

All the hereby presented case studies are referred to the horizontal polarization of the radar. Similar results can be obtained for the vertical polarization. As a confirmation of this, Figure 12 shows the reflector RCS difference between vertical and horizontal polarizations at Ku band for different illumination angles. RCS variations below 0.1 dB are observed for the vast majority of the investigated angles and certainly for the angles of interest, as far as the radar illumination of the reflector is concerned.

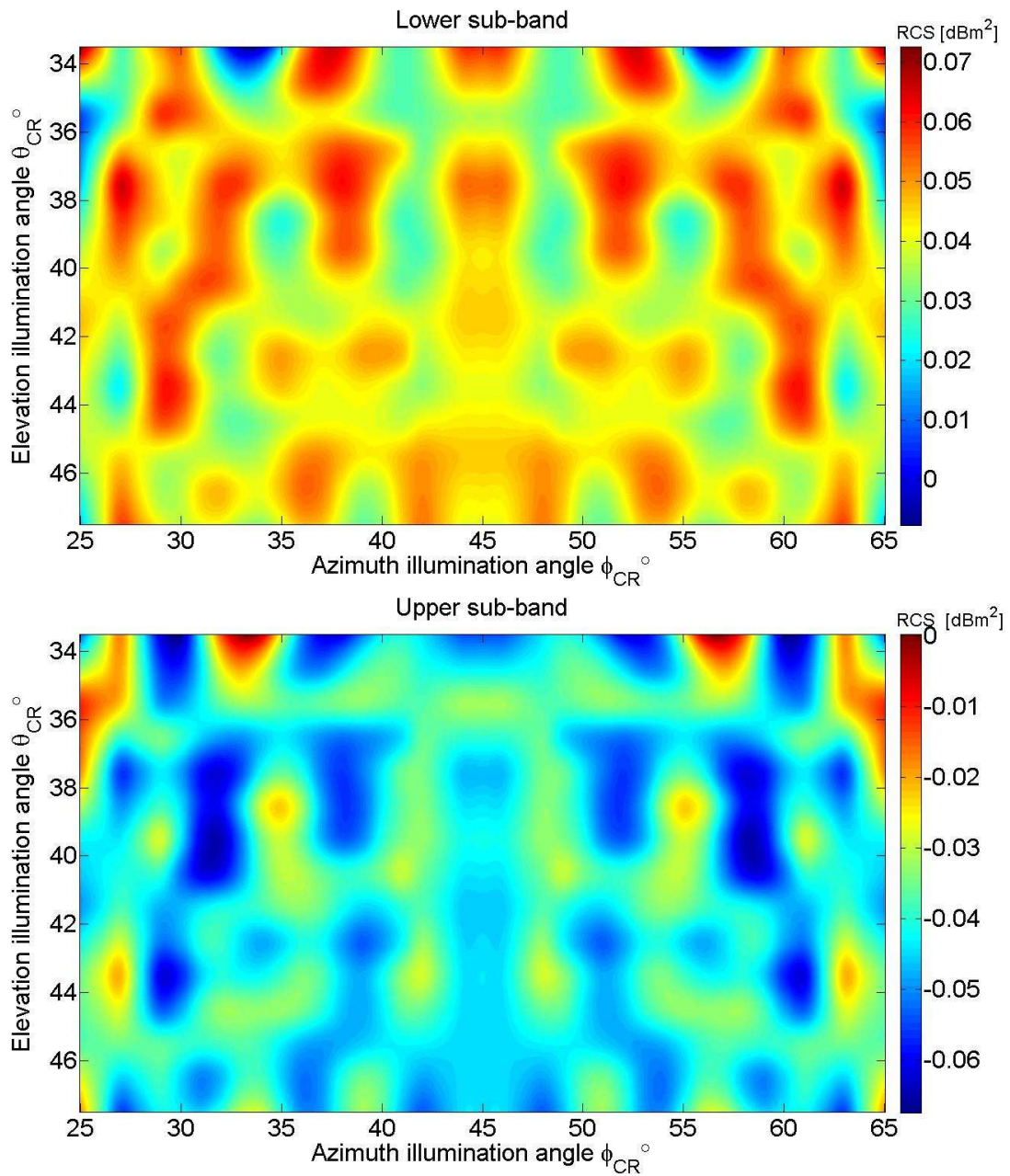


Fig. 11: Differences between the RCS values simulated for the corner reflector at mid-band and those calculated at the two extremes (lower and upper) of the transmitted bandwidth (X-band).

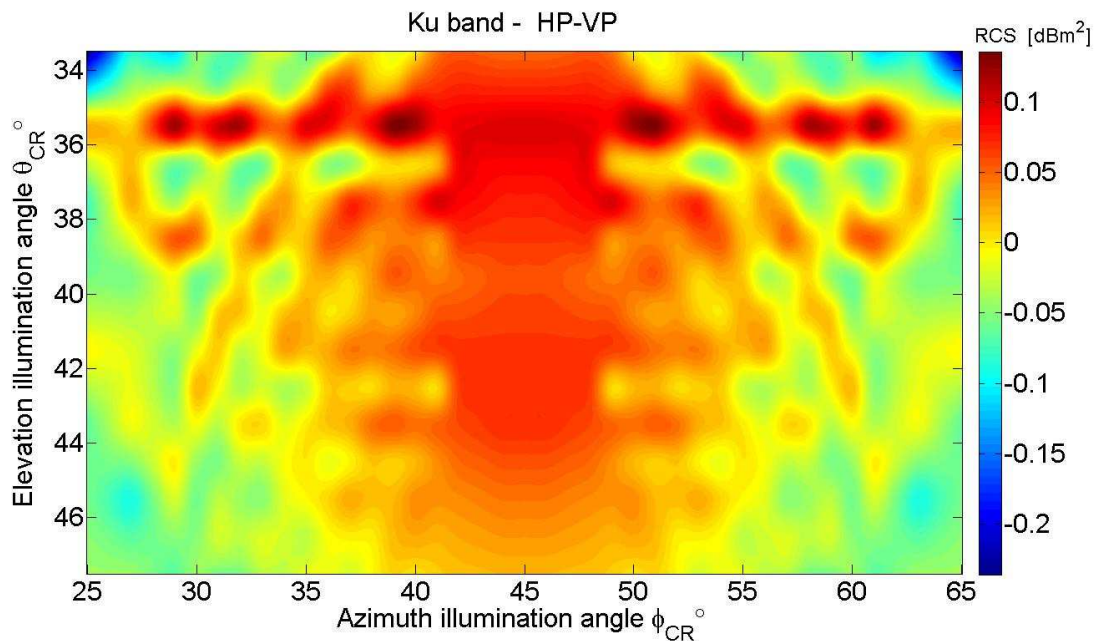


Fig. 12: Reflector RCS difference between the values for horizontal and vertical polarizations at the Ku-band. Variations in absolute value below 0.1 dB are observed for the vast majority of the illumination angles.

The effects of a variation in the direction of linear polarization of the illuminating wave in the reflector estimated RCS have been taken into account. This kind of polarization rotation may correspond to a situation when a pitch angle is present during the motion of the airplane, or equivalently, it may be representative of a roll tilt in the deployment of the corner reflector. Figure 13 shows the reflector RCS variation with a polarization rotation of $\pm 6^\circ$ at X and Ku band for horizontal and vertical polarizations, respectively. The illumination angle is chosen to be $\theta_{CR} = 45^\circ$ and $\phi_{CR} = 45^\circ$. This RCS deviation is shown in figure to be negligible (lower than 0.001 dB) and this situation holds for all illumination angles and directions of linear polarization.

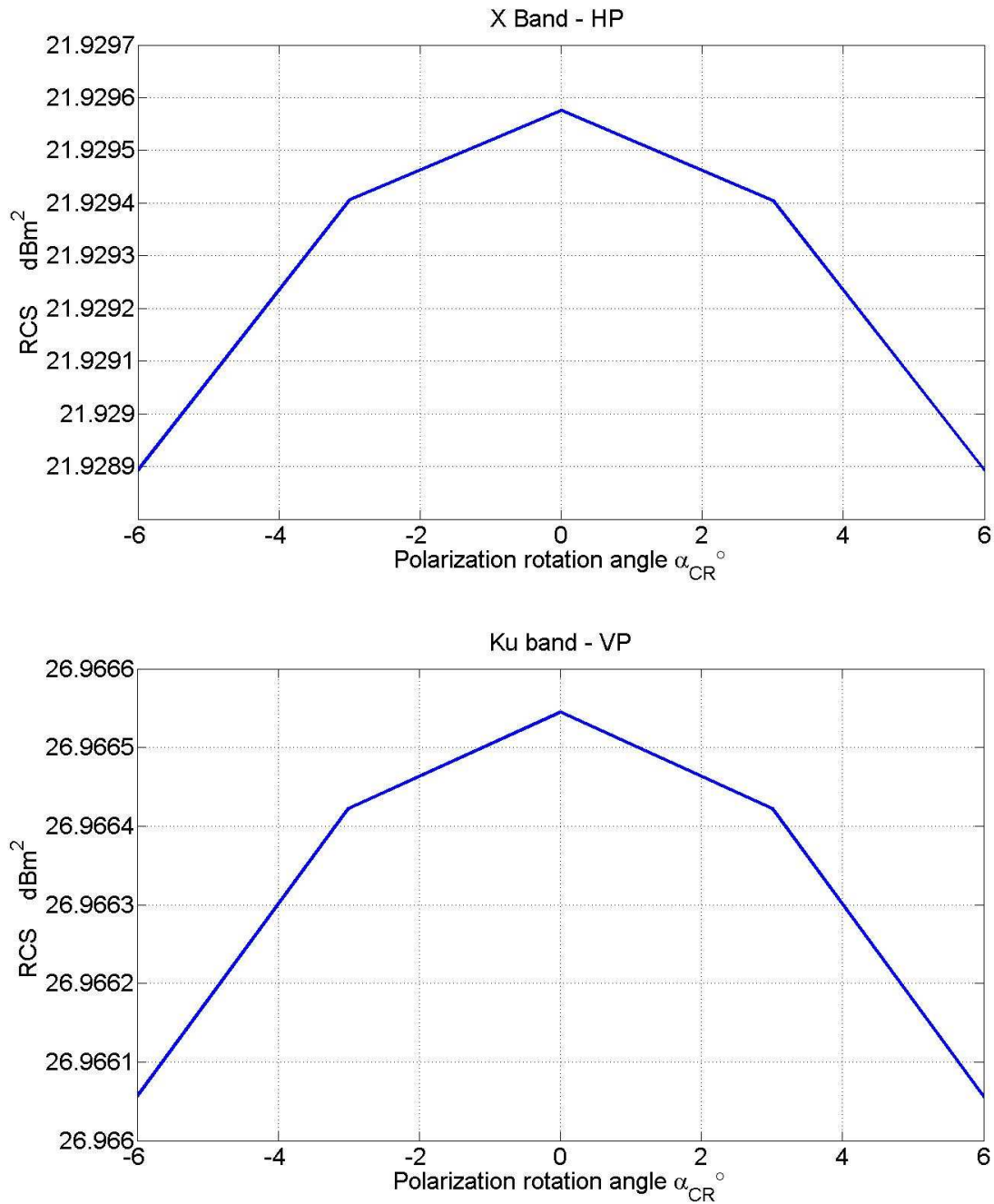


Fig. 13: Reflector RCS variation due to a 3 degree step polarization rotation of the incident wave. The observed RCS deviations, lower than 0.001 dB over a +/-6° polarization rotation (possibly induced by a pitch angle in the airplane motion or a roll tilt in the deployed reflector) can be considered negligible.

4 Measurement campaign in Finland

The SnowSAR measurement campaign has been performed in the Lappish region of Finland, between 12th and 19th of March 2011. It mostly interested the area close to the town of Sodankylä, where the Artic Research Centre is located. A detailed description of the performed acquisitions can be found in [3]. In parallel with the SnowSAR airborne campaign, additional measurements have been performed over the same area, suitable for comparison and validation within the ongoing ESA's NoSREx extension project. Besides satellite observations (AMSR-E, TerraSAR-X), also ground measurements (detailed snow depth, SWE, SD) have been carried out by the Finnish Meteorological Institute, FMI. As an example, in Figure 16 (from Google Earth) the transect Nr. 2 is shown, the one passing by the Artic Research Centre (ARC) Intensive Observation Area (IOA) area, close to the corner reflectors displacement place during the measurement campaign. In Figure 14 (a) the red line represents the ideal 7.5 Km long flight trajectory, the yellow line represents the correspondent trajectory on the ground (centre of swath), and the yellow shade represents the designed 400 metres-wide SnowSAR acquisition strip. The airplane was flying from south to north direction, being the radar left side-looking. Figure 14 (b) is a zoom-in of Figure 14 (a), showing a SnowSAR preliminary result relative to the same area: a crop of the first uncalibrated Ku band VV/HV image is over imposed to the Google Earth map. The four corner reflectors are distinguishable on the SnowSAR image as four bright spots along the river.

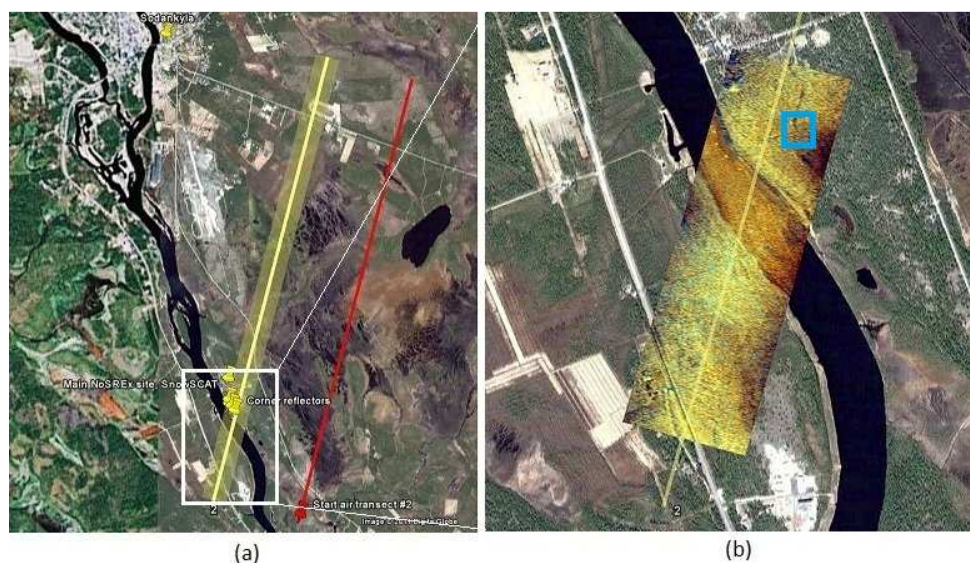


Fig. 14: SnowSAR measurement campaign. (a) Transect nr. 2 is shown in the proximity of Sodankylä: in red the ideal flight trajectory, in yellow the correspondent ground strip. (b) Zoom in of the highlighted area of (a): a SnowSAR image acquired on the 15th of March 2011 is overlapped to the Google Earth image. The ARC - IOA is represented as a blue square; the four corner reflectors are visible on the river.

4.1 Corner reflectors deployment

During the measurement campaign the corner reflectors have been deployed so that their geographical locations fall within the designed swath (yellow shade in Fig. 17) of the transect Nr. 2 (yellow line in Fig. 15). The trihedral reflectors on the ground were oriented azimuthally to maximize their RCS in the direction that is orthogonal to the flight track.

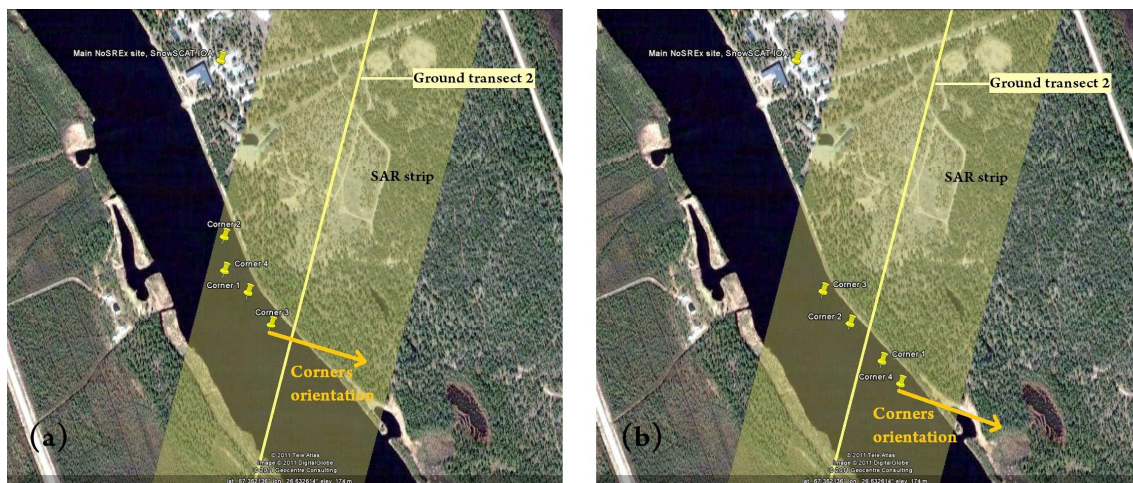


Fig. 15: Corner reflector deployment in proximity of the SnowSCAT site, during two different flights: (a) 15th March 2011; (b) 16th and 17th March 2011. The yellow line represents the centre of the 400 m radar swath (yellow shade) [3]. The azimuthal orientation of the corner reflectors (free vertex) is meant to be perpendicular to the direction of flight for maximum RCS.

The flight trajectories (and corresponding swaths) were defined by a start and an end points, given in geographical coordinates (GPS latitude and longitude), where a Geographic (or true) North (N_G) direction can be identified (refer to Figure 16). The chosen trajectories resulted in a flight direction equal to 15° from N_G and, therefore, the trihedral reflectors had to be oriented in direction $15^\circ + 90^\circ = 105^\circ$ East from N_G . However, the heading of the corner reflectors on the ground was realized by means of a magnetic compass. This means that the free-vertex (see Figure 10) of the reflectors was oriented to 105° East from the Magnetic North (N_M) direction, as indicated by the alignment instrument, instead of from the Geographic North (N_G).

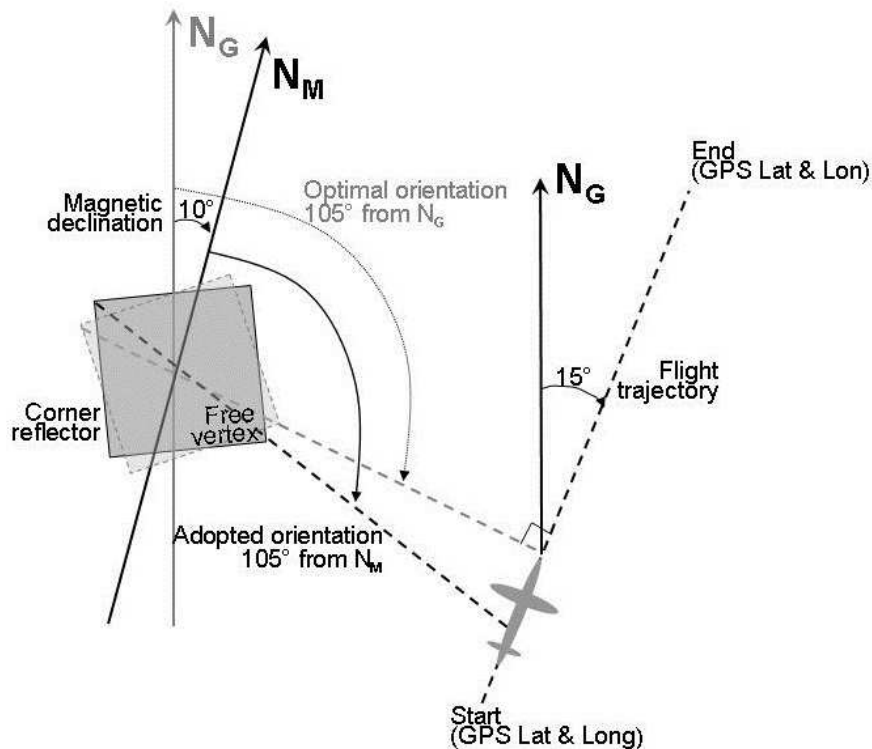


Fig. 16: Orientation of the free vertex of the corner reflectors (estimated by a magnetic compass) and of the airplane flight trajectory (designed by a GPS system) during the measurement campaign. The magnetic declination has been taken into account within the SAR image calibration process.

The direction of geographic North may be different from the direction of magnetic North. This phenomenon, called *magnetic declination*, varies with latitude, longitude and in time and it results in a correction that must be applied to the direction indicated by a compass, when searching the geographic north. This correction can be quite important at arctic latitudes. The day of the campaign (March 15th), in Rovaniemi (the closest location with available correction data), the magnetic declination is estimated in 10° East [5]. However, during the placement and orientation of the corner reflectors the magnetic declination was not taken into account. This resulted in a 10° offset rotation of the direction of maximum RCS with respect to the direction that was orthogonal to the flight track. This direction resulted then orthogonal to $\Phi_{CR}=55^\circ$, instead of the direction of maximum RCS $\Phi_{CR}=45^\circ$, in the reference system of the corner reflectors (see Figure 8). As a consequence, the measured reflector RCS was slightly reduced and more variable across the illumination time. However, this misalignment does not impact significantly the radar data calibration as far as it is taken into account.

When accommodated on the terrain covered in snow and ice, the corner reflectors were also affected by other misalignments, such as a roll tilt and a pitch tilt of the free-vertex, with respect to the surface of deployment. The roll and pitch tilts were measured respectively 0° ($\pm 1^\circ$) and 1.5° ($\pm 1^\circ$) nose-up. The corner reflectors have been positioned by local scientists of the Finnish Meteorological Institute, Arctic Research Centre (FMI-ARC).

4.2 SnowSAR antennae configuration

In this section the GPS and SnowSAR antennae configurations on the airplane are described with respect to the IMU position, since they represent important factors which have to be taken into account in the SnowSAR image calibration process. Drawings of the GPS-IMU and SnowSAR antennas location and orientation onboard the employed Cessna 208 Caravan aircraft are shown in the next Figures.

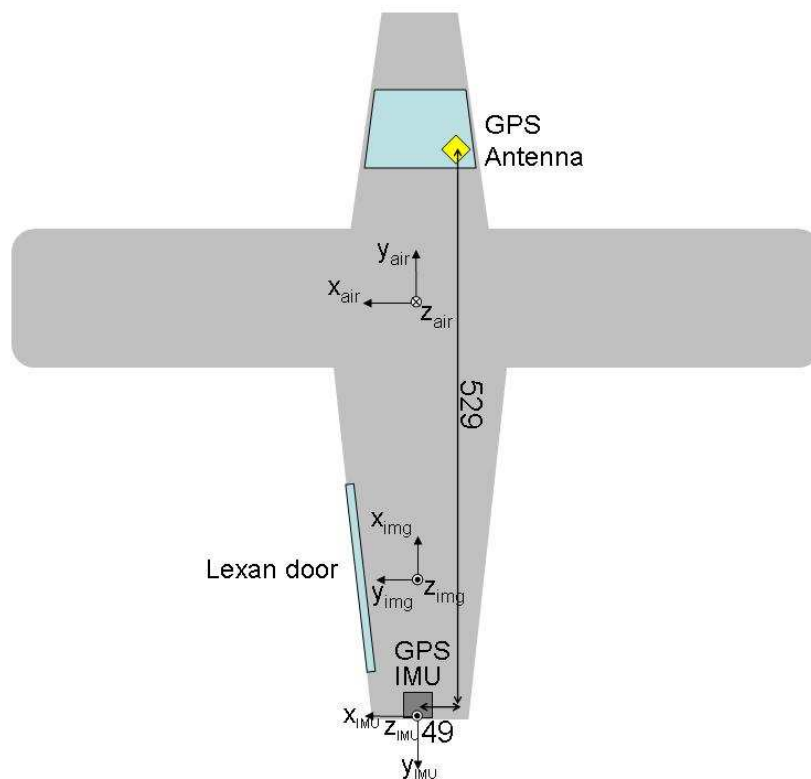


Fig. 17: Top view representation of the aircraft configuration. 3 reference systems are adopted for convenience, relative to the aircraft (air), to the IMU unit (IMU) and to the radar image and to the airplane trajectory (img). Distances between GPS antenna and GPS-IMU unit are in cm (height difference 109 cm).

In Figure 17 an overview is given about the reference systems adopted within this document, relative to the aircraft (air), to the image (img) and to the IMU (IMU). The displacement of the GPS antenna with respect to the IMU system is also indicated, with lengths expressed in centimetres.

The SnowSAR antennae set-up on board of the aircraft is sketched in Figure 18, where lengths are given in centimetres. Figure 18 (a) shows the antennae configuration on the mounting frame. For each of the two bands, X and Ku, both the transmitting (TX) and receiving (RX) antenna are shown, together with their (square) aperture dimension and relative spacing. This configuration has been chosen (based on antennae coupling minimization) among different options which have been tried during the testing phase in Teuge. Figure 18 (b) represents a top view of the tail of the aircraft, where the distances between IMU unit and antenna mounting frame can be appreciated. It has to be noted how the pointing direction of the SnowSAR antennas onboard the aircraft were not perpendicular to the direction of flight: an estimated squint angle of 5° toward the rear of the airplane is introduced, to follow the shape of the airplane fuselage and to minimize the blockage of the luggage door and of the airplane floor.

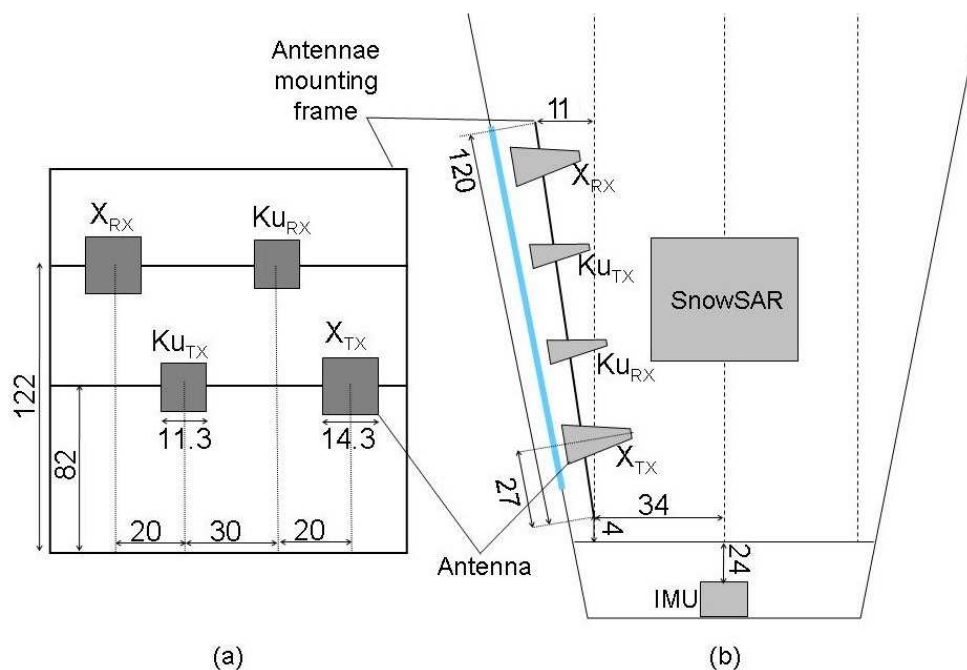


Fig. 18: SnowSAR antennae set up on board the aircraft: (a) mounting configuration from a side view; (b) top view of the tail of the aircraft, where displacement between SnowSAR antennae and IMU can be estimated. Dimensions are in cm.

5 Radiometric calibration

The radiometric calibration defines and corrects system-induced errors to provide a known relation between the SAR image pixel brightness and the physical parameter under observation, in this case the normalized backscatter coefficient. When calibrating a SAR image the influence of possible error contributions throughout the whole system have to be accounted for. The fluctuations in the transmitted power, in the receiver gains and the system noise in general, all together referred as to internal calibration, are discussed in section 5.1.

An adequate radiometric calibration of SAR data also requires the knowledge of the in-flight antenna pattern. To this end, the RCS responses of the corner reflectors, provided in the previous sections of this document, are used. By deploying the trihedral reflectors across the radar swath, the elevation antenna pattern can be reconstructed. Furthermore, the RCS response of the corner reflector at different angles is de-embedded from the range bins acquired during the pass, in order to determine the azimuth antenna pattern. The complete procedure, referred as to the external calibration, and is covered in section 5.2.

5.1 Internal calibration

In this section two main aspects are considered, related to the SnowSAR internal calibration: the monitoring of important parameters, like internal temperature and transmitted power, useful to identify correction factors in the post-processing phase, and the definition of internal calibration loops, to ensure the stability of the receiver.

5.1.1 *Temperature monitoring*

The major internal radiometric error source in a SAR sensor is the gain modification caused by temperature variations within the system. As already mentioned, two counter-measures are adopted in the SnowSAR system: firstly, the radar is enclosed in a thermally stabilized box by a Peltier unit; second, an internal calibration loop is used in order to monitor gain variations with temperature and time. Figure 19 shows the SnowSAR measured internal

temperature during an observation window of more than one hour and a half: an overall variation of less than 2 degrees is shown.

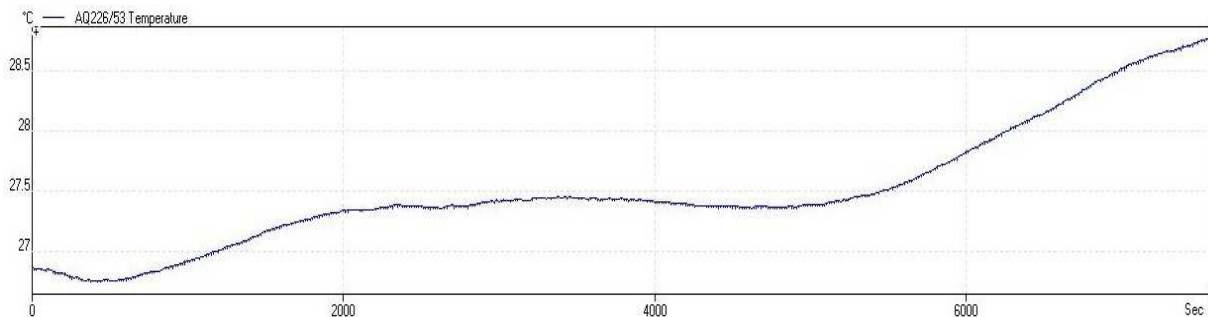


Fig. 19: SnowSAR internal temperature monitored during repeated acquisitions.

5.1.2 Transmitted power tracking

The power tracking of the transmitted RF signal is a fundamental element in the SnowSAR image synthesis process, because it allows for calibration corrections. The SnowSAR power levels have been monitored during all the acquisitions by means of periodic measurements of the transmitted power. Two power meters are used for this scope, one for the X-band and one for the Ku-band subsystems. Every 4 seconds each power meter switches between polarization channels. In order to be unequivocally discriminated during the post-processing phase, the two polarizations have different attenuations (13 dB difference) in the calibration lines.

In Figure 20 the tracked power as a function of time is given as an example. Within a total duration of approximately 35 minutes, a number of SnowSAR data takes acquired over Sodankyla on the 15th of March are represented. The two curves, black and red, represent the measured power, respectively for the X-band and Ku-band. For each band the higher measured levels are relative to the horizontal polarization, while the lower to the horizontal polarization.

To better appreciate the dynamics of the measured power for the considered frequency bands and for the polarization modes, the same data of Figure 20 are plotted in Figure 21, case by case. In particular Figure 21 (a) shows the tracked power consequentially, i.e. without breaks

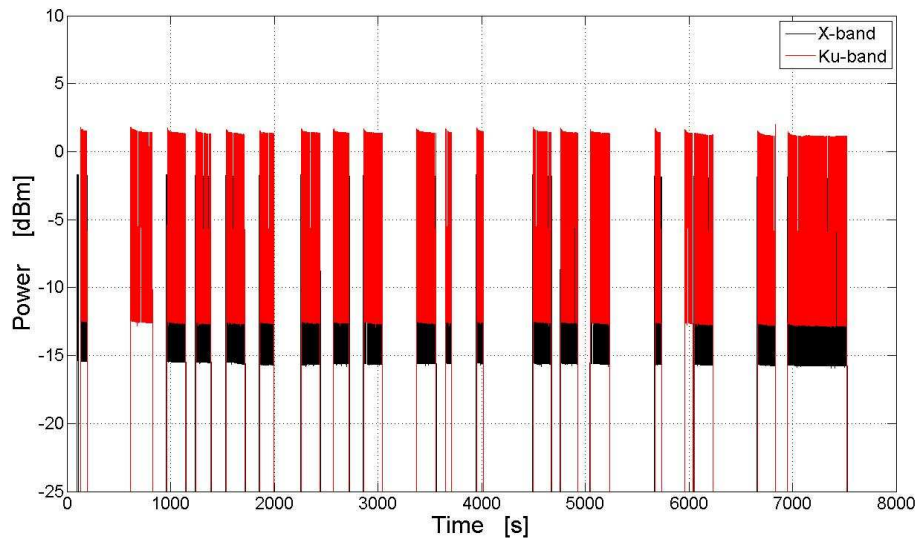
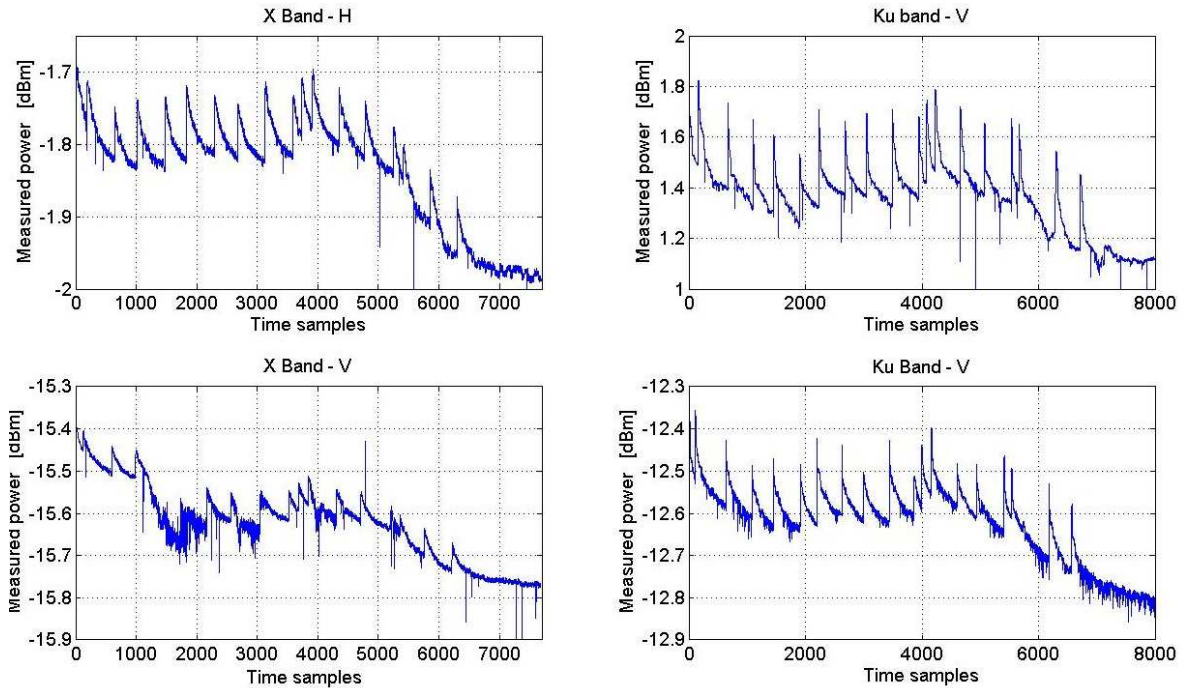


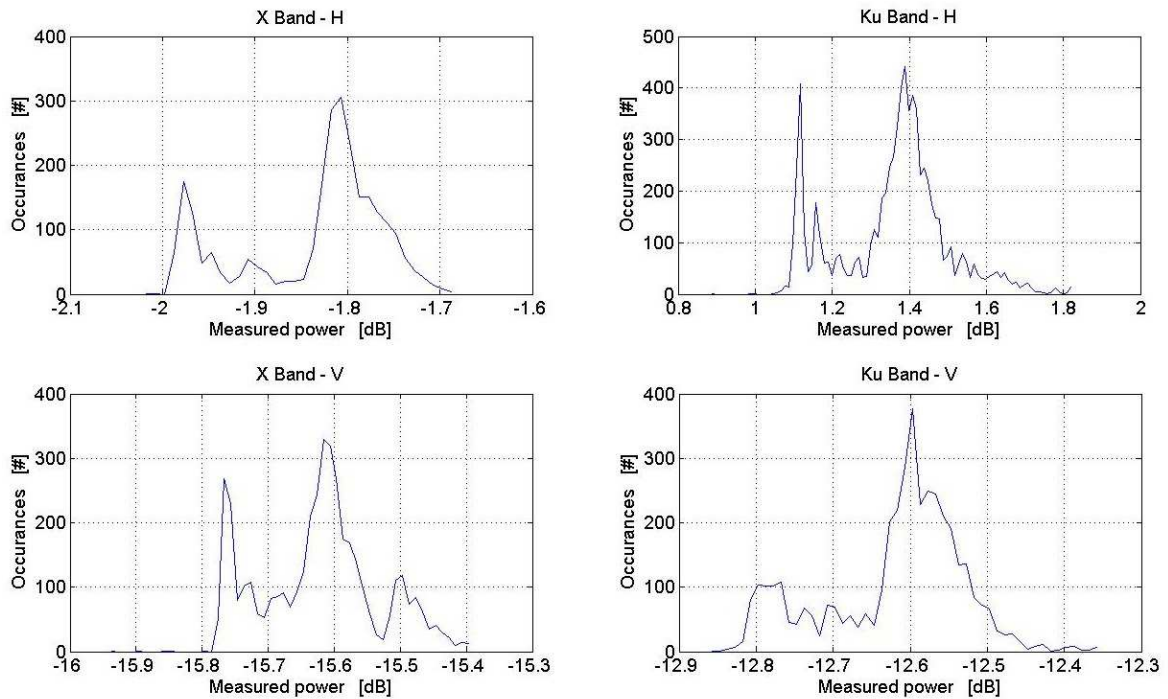
Fig. 20: SnowSAR transmitted power tracking for the X- and Ku- frequency bands, in black and red respectively, during following acquisitions. The accuracy of the adopted power meter is 0.1 dB.

in between following acquisitions. Power spikes can be noticed, corresponding to the beginning of each acquisition. However, the measured power tends to shortly stabilize within the acquisition interval. In Table I the main statistics of the plotted data are summarized, acquisition by acquisition. In particular the power variation within the single acquisition is represented by the ‘Delta’ parameter. From its analysis it can be seen that the total power variation within each acquisition remains limited, about 0.15 dB for most of the cases.

Figure 21 (b) shows the occurrences of events related to the all tracked power plots of Figure 21 (a). It can be seen how the power levels remain globally constant all over repeated acquisitions. However, two main lobes can be appreciated; this fact can be explained with a transitory start-up phase followed by a more stable phase, in which a substantial power level equilibrium is reached. From Table I it can be seen that the last acquisition is in absolute the longest (more than 10 minutes) among all (average acquisition duration is less than 3 minutes), and it is the one responsible for the secondary lobes in Figure 21 (b); within the acquisition the tracked power is reasonably stable.



(a)



(b)

Fig. 21: SnowSAR transmitted power tracking for the X- and Ku- frequency bands and for both polarization channels, during following acquisitions over Sodankyla on the 15th of March. (a) Measured power. (b) Occurrences of the measured values.

Table I – SnowSAR measured power

			H pol					V pol				
Acq Nr.	Duration [s]		Min	Max	Delta	Mean	St. Dev	Min	Max	Delta	Mean	St. Dev
1	30		-1.7	-1.68	0.03	-1.69	0.01	-15.4	-15.39	0.01	-15.4	0.01
2	80		-1.81	-1.69	0.12	-1.75	0.12	-15.45	-15.4	0.05	-15.43	0.01
3	200		-1.84	-1.71	0.12	-1.8	0.17	-15.51	-15.4	0.11	-15.46	0.24
4	175		-1.84	-1.75	0.09	-1.82	0.11	-15.52	-15.44	0.08	-15.49	0.02
5	200		-1.84	-1.74	0.1	-1.81	0.04	-15.65	-15.45	0.2	-15.53	0.2
6	150		-1.83	-1.73	0.09	-1.81	0.2	-15.69	-15.57	0.1	-15.65	0.03
7	200		-1.82	-1.72	0.1	-1.8	0.19	-15.72	-15.57	0.16	-15.63	0.07
8	190		-1.82	-1.73	0.09	-1.8	0.14	-15.74	-15.54	0.2	-15.59	0.21
9	200		-1.83	-1.74	0.09	-1.82	0.22	-15.71	-15.55	0.16	-15.6	0.33
10	220		-1.84	-1.71	0.13	-1.81	0.19	-15.62	-15.55	0.07	-15.6	0.02
X Band	11	70	-1.8	-1.73	0.06	-1.79	0.21	-15.63	-15.55	0.09	-15.53	0.44
	12	80	-1.78	-1.71	0.07	-1.77	0.24	-15.71	-15.53	0.18	-15.54	0.3
	13	210	-1.81	-1.7	0.12	-1.79	0.21	-15.7	-15.51	0.19	-15.58	0.18
	14	250	-1.83	-1.72	0.11	-1.8	0.16	-15.64	-15.54	0.09	-15.59	0.02
	15	280	-1.94	-1.74	0.2	-1.84	0.22	-15.64	-15.43	0.21	-15.6	0.17
	16	110	-1.86	-1.78	0.08	-1.85	0.23	-15.73	-15.58	0.15	-15.6	0.34
	17	240	-2.02	-1.8	0.22	-1.9	0.19	-15.73	-15.6	0.13	-15.67	0.03
	18	210	-1.96	-1.84	0.12	-1.95	0.23	-15.74	-15.64	0.11	-15.71	0.03
	19	620	-2.01	-1.87	0.14	-1.98	0.16	-15.94	-15.67	0.27	-15.74	0.26
Average in 3715 s					0.11	-1.82	0.17			0.13	-15.58	0.15

			H pol					V pol				
Acq Nr.	Duration [s]		Min	Max	Delta	Mean	St. Dev	Min	Max	Delta	Mean	St. Dev
1	80		1.49	1.78	0.29	1.54	0.08	-12.53	-12.35	0.18	-12.47	0.05
2	250		1.39	1.82	0.44	1.48	0.11	-12.61	-12.36	0.25	-12.53	0.04
3	200		1.31	1.74	0.43	1.41	0.08	-12.66	-12.43	0.23	-12.57	0.04
4	175		1.28	1.67	0.38	1.37	0.07	-12.65	-12.49	0.16	-12.6	0.03
5	200		1.24	1.61	0.37	1.35	0.07	-12.67	-12.47	0.2	-12.6	0.03
6	150		1.32	1.53	0.21	1.37	0.05	-12.63	-12.48	0.14	-12.59	0.03
7	200		1.35	1.71	0.35	1.42	0.06	-12.62	-12.42	0.2	-12.57	0.04
8	190		1.36	1.66	0.3	1.43	0.06	-12.62	-12.44	0.19	-12.58	0.03
9	200		1.32	1.69	0.37	1.4	0.07	-12.63	-12.5	0.13	-12.59	0.03
10	220		1.34	1.71	0.36	1.42	0.07	-12.63	-12.43	0.2	-12.57	0.04
Ku Band	11	70	1.42	1.68	0.26	1.48	0.08	-12.6	-12.51	0.09	-12.55	0.02
	12	85	1.46	1.75	0.28	1.54	0.07	-12.56	-12.44	0.12	-12.52	0.03
	13	210	1.4	1.79	0.39	1.48	0.08	-12.6	-12.4	0.2	-12.54	0.04
	14	200	1.35	1.72	0.37	1.44	0.08	-12.62	-12.48	0.13	-12.57	0.03
	15	280	1.3	1.65	0.35	1.39	0.06	-12.66	-12.48	0.17	-12.61	0.03
	16	80	1.34	1.67	0.34	1.44	0.09	-12.61	-12.46	0.15	-12.57	0.04
	17	90	1.34	1.65	0.31	1.4	0.07	-12.64	-12.49	0.15	-12.6	0.04
	18	190	1.15	1.37	0.22	1.26	0.05	-12.75	-12.62	0.14	-12.68	0.02
	19	210	1.15	2.01	0.39	1.24	0.1	-12.74	-12.53	0.21	-12.69	0.04
	20	620	1.06	1.45	0.4	1.14	0.05	-12.86	-12.58	0.28	-12.77	0.04
Average in 3900 s					0.34	1.4	0.07			0.18	-12.59	0.03

Table I - SnowSAR measured power, see Figure ACQ. Both the polarizations are considered for each frequency band. Each row corresponds to a single acquisition, for which the following parameters are given: duration, minimum and maximum measured power, power excursion, mean value and standard deviation. Last row gives an average of the considered parameters over all the performed acquisitions. Values are in dBm.

The power behavior within the single acquisition is given in Figure 22 (a), relative to the X-band subsystem, vertical polarization. As already mentioned, a decaying trend of the measured power values can be noticed. This feature characterizes many other acquisitions (for instance see Figure 6, obtained during tests). To avoid this, the instrument should be

warmed up for some time before beginning the acquisition, so that stable working conditions are ensured. For convenience, a fitting curve of the measured power data is used within the calibration process instead of the measured data themselves. An example of fitting curve is shown in red in Figure 22 (a). Figure 22 (b) represents the error which follows by introducing this approximation: it can evidently be neglected.

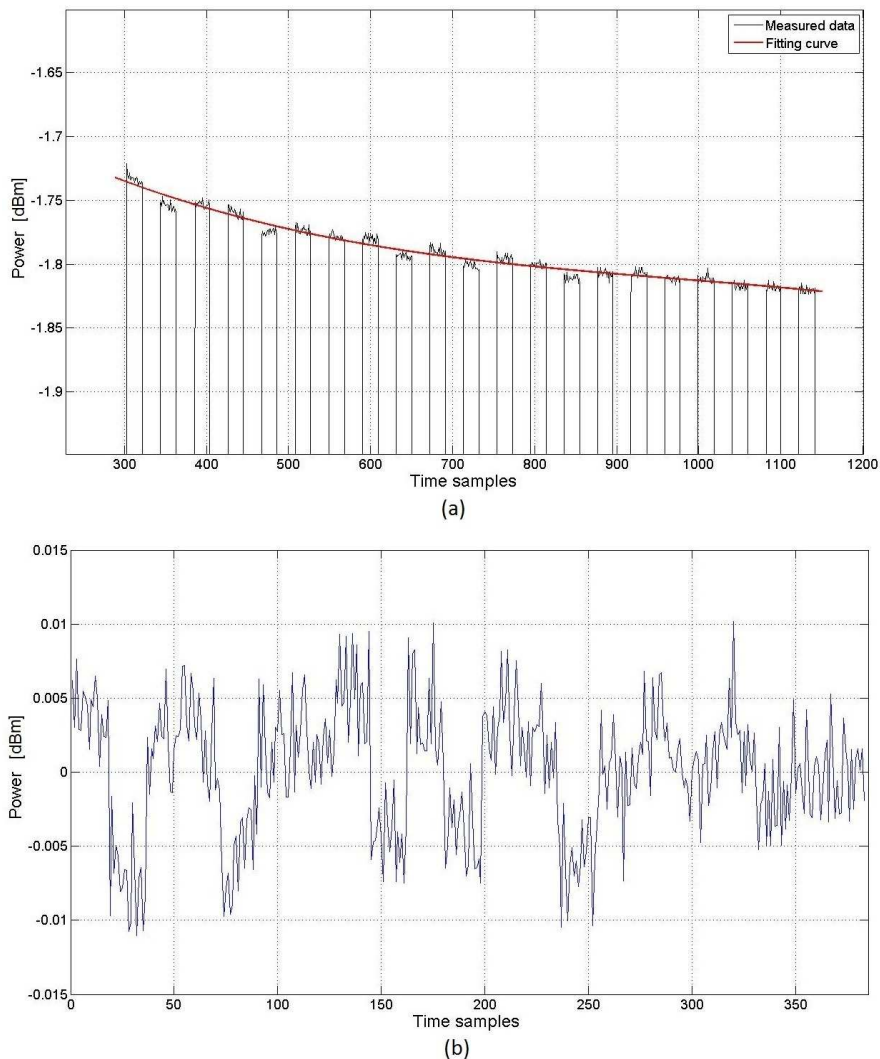


Fig. 22: SnowSAR transmitted power tracking during a single acquisition for the X- band, vertical polarization. (a) Measured values and fitting curve (only the significant, i.e. non-zero, intervals of the measurement period are taken into account within the interpolation). (b) Approximation error due to the adoption of the fitting curves instead that the measured values within the radiometric calibration.

5.1.3 Receiving gain tracking

The SnowSAR receiving gain has been tracked during the acquisitions. Figure 23 (a) shows a block diagram with the tracking strategy implemented within the SnowSAR: periodically the TR-RX module is switched off, a part of the generated signal is collected by a 30 dB dual coupler and it is routed back to the receiving chain to track possible gain variations. As represented in Figure 23 (b), within 256 generated pulses 3 are used for calibration.

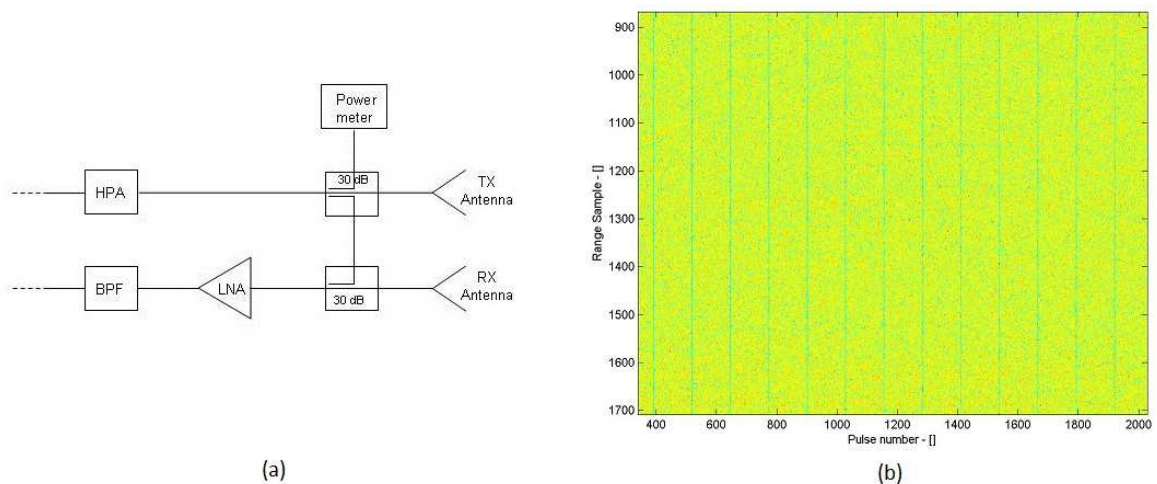


Fig. 23: SnowSAR receiving gain tracking: (a) block diagram of the implemented strategy; (b) example of radar raw data showing the calibration pulses.

As an example, Figure 24 shows the monitored receiver gain of the SnowSAR system in two different acquisitions during the Finnish measurement campaign, from which the radiometric stability can be appreciated.

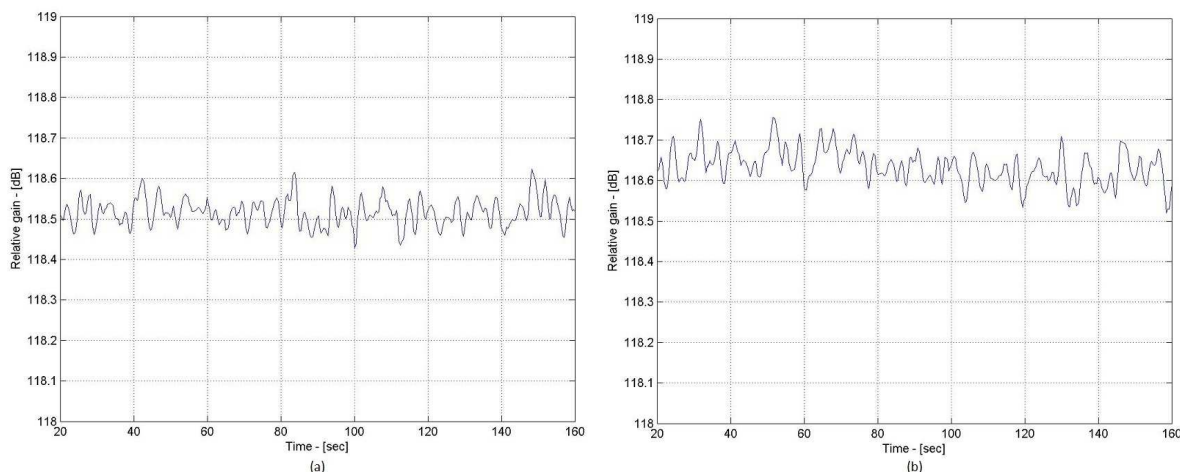


Fig. 24: SnowSAR receiver gain monitoring during different acquisitions, (a) and (b), for the Ku band subsystem, VV polarization mode.

5.2 External calibration

As already mentioned, the SAR antenna patterns must be known very precisely for the radiometric calibration. To a certain degree, this has been achieved by test-lab measurements before the flight campaign. However, once mounted on the aircraft platform the antenna patterns may change, due to changed working conditions, introducing antenna mutual coupling and blockages, reflections and diffractions of the aircraft structures. The antenna patterns must be therefore, re-assessed in flying conditions.

The external radiometric calibration method used in the framework of the SnowSAR project is based on the comparison between the response of the trihedral corner reflectors and the response extracted from the acquired data, which include both the responses of the corner reflectors and of the antenna patterns.

The implemented methodology for SnowSAR external calibration during the Finnish campaign is the subject of the present section: in particular section 5.2.1 summarizes the antenna pattern as it has been characterized on ground before the flight campaign. Sections 5.2.2 and 5.2.3 focus on the elevation and azimuth planes of the antenna pattern, respectively.

5.2.1 *Antenna characterization*

The SnowSAR radar antennae has been characterized “on the ground” by measurements in the anechoic chamber. For both the frequency bands the radiation patterns in the main planes have been measured. As an example, in Figure 25 two measured patterns are given, relatively to the X-band subsystem.

Concerning the characterization of the antennae in their final configuration, the level of cross-polarization introduced by external structures (other antennae and aircraft structures) has been estimated. Taking into account that a corner reflector does not introduce any polarization distortion in the reflected radar signal, by analyzing the cross-polar response

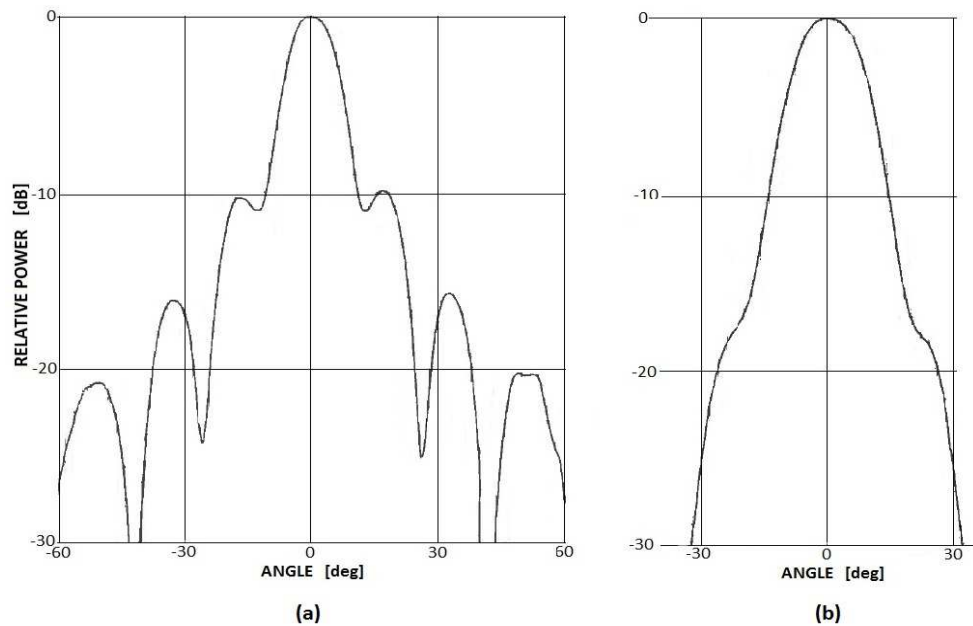


Fig. 25: SnowSAR antenna characterization: patterns measured in the anechoic chamber for the X-band subsystem (measurements performed at 9.6 GHz). (a) E-plane, horizontal polarization; (b) H-plane, vertical polarization.

from the corner reflectors when a linear polarization is applied to the transmitting antenna, it is possible to estimate the level of cross polarization introduced. During a test flight in Teuge this has been estimated to be 20 dB for the chosen configuration.

5.2.2 Elevation plane pattern

During the acquisition flight of the 15th of March the corner reflectors were not placed optimally, meaning that only half of the radar swath was covered by them, see Figure 15. For this reason it has not been possible to exploit them for the in-flight antenna pattern determination in the elevation plane, and a complementary method has been adopted, using acquired data. An area is considered in which the measured backscatter propriety is as uniform as possible. From this it is possible to synthesize the elevation antenna pattern, by using radar scattering model for the terrain typology under consideration (wet snow in this case) which takes into account the variation of the backscattering coefficient as a function of the incident angle [6].

As an example, Figure 26 shows the achieved elevation pattern for the Ku-band subsystem, for the VV polarization mode. As expected the pointing direction is 40°.

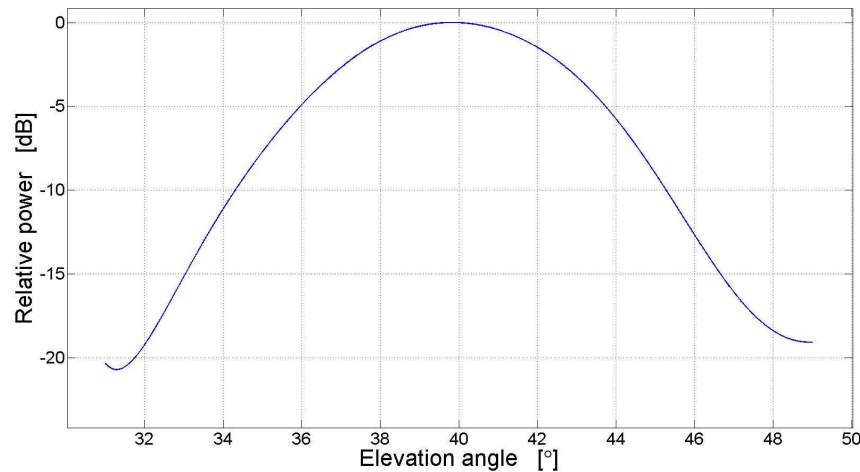


Fig. 26: SnowSAR external calibration, synthesized antenna elevation pattern for the Ku band, VV polarization mode.

5.2.3 Azimuth plane pattern

The methodology used for deriving the in-flight azimuth antenna pattern is presented in this section. As first step, the acquired raw data are processed, in order to obtain a set of range-compressed data. From the range-compressed unfocussed SAR image, the area containing the corner reflectors is selected and extracted, as described in Figure 27.

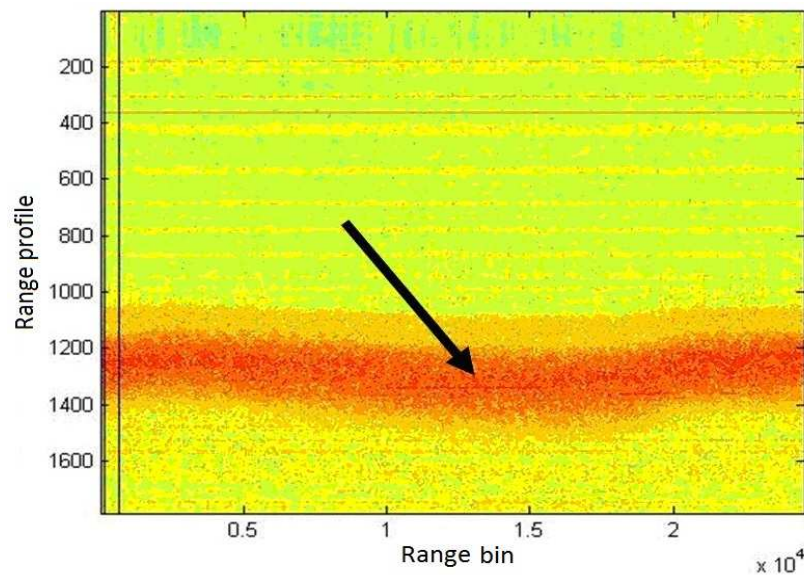


Fig. 27: Determination of the part of the image containing the corner reflectors.

By combining the position of the corner reflectors (measured on the ground with GPS) and the GPS-IMU data of the aircraft location associated with every acquisition, the image containing the corner reflectors is extracted; different sub-slices are subsequently singled out, each one centered at the corner reflector of interest. Within this process, the range migration correction is also applied and the groups of range bin lines containing the single corner reflector responses are determined. Figure 28 shows an example of a sub-slice image, centered at the second corner reflector.

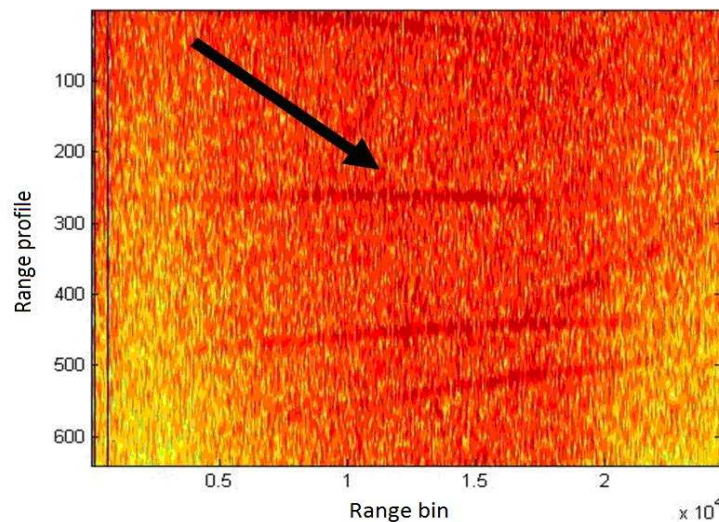


Fig. 28: Sub-slice image centered at the second corner reflector

A digital spotlight process is then performed for clutter suppression to better focus on the selected corner reflector. Then, the power values resulting from the previously selected range bin lines are added up, giving a single power value for each range bin, as represented in Figure 29. At this point, the values exceeding a certain threshold (75 dB for example) are selected and stored, together with their positions. The following steps of the calibration process will be focused only on these points.

By fitting the points found as above described, it is possible to determine the radar response of each corner reflector from the acquired data, as represented in Figure 30.

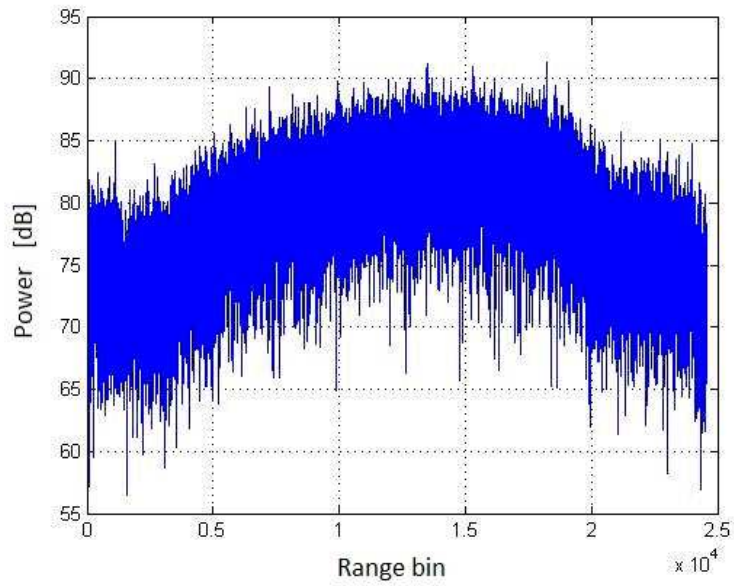


Fig. 29: Example of range profile relative to the selected trihedral reflector.

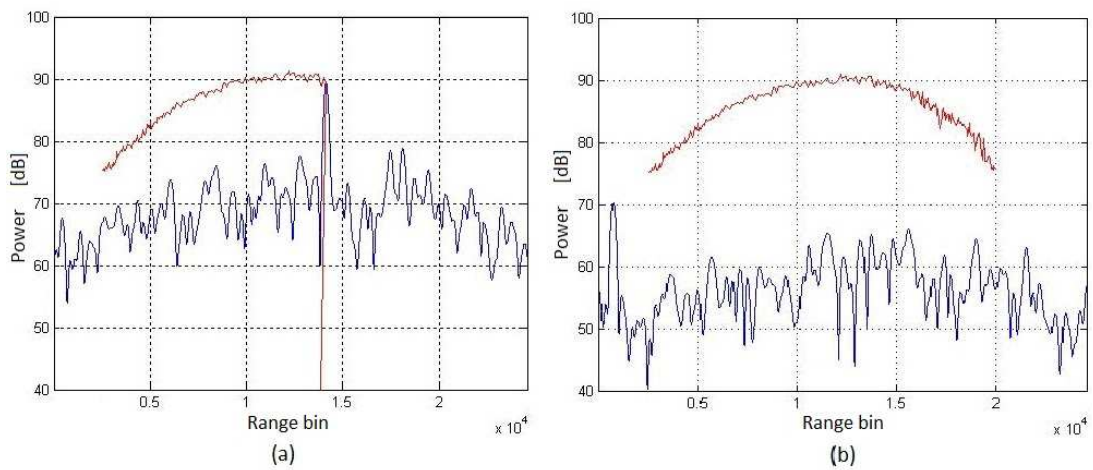


Fig. 30: Corner reflector response determination. (a) Tracking of the values of interest from the range profile; (b) obtained response from the data, after filtering of outlier values.

The next step consists in the estimation of the geometric angles (elevation and azimuth) between the aircraft and the corner reflectors. This is obtained by using the GPS-IMU data and the reflector positions. The estimation of the geometric angles is then corrected by a factor taking into account the effective aircraft orbit heading during the acquisition, the difference between the Magnetic and the Geographic North and the tilt angles of the corner reflectors. By using these angles and the RCS values of the corner reflector for the angle ranges of interest, the radar responses of the corner reflector themselves are estimated.

After calculating the slant range distances between the aircraft and the corner reflectors along the image, the antenna patterns are estimated by de-embedding the contribution of the corner reflector, previously described in this document, to the response extracted from the data. The extracted response contains also contributions of different look angles (Figure 31).

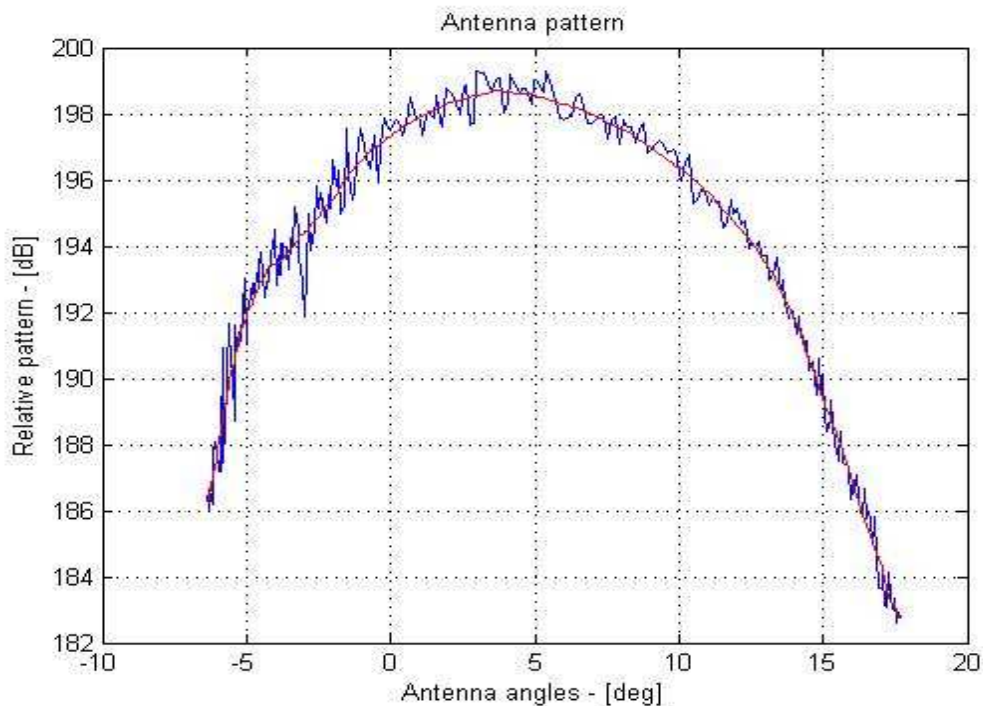


Fig. 31: Estimated antenna pattern as result of the calibration process.

6 Error analysis

Some of the potential error sources within the calibration process are hereby taken into consideration. Potential effects of possible GPS-IMU errors on the radiometric precision are given in section 6.2. The error introduced in the antenna pattern determination is described in section 6.3.

6.1 Aircraft attitude

An important error source in the image calibration is represented by the motion errors in the aircraft trajectory. The aircraft attitude translates in a disturbed radar antenna pointing direction, which is not following the ideal strip line of the SAR technique. In particular, the aircraft roll motion impacts mostly the boresight direction in the antenna elevation plane. The yaw angle affects principally the boresight direction in the azimuth plane. The pitch orientation chiefly influences the transmitted and received polarizations. These issues have been tackled by means of an accurate GPS-IMU system [7]. Positions (geographic coordinates) and attitude (yaw, pitch and roll angles) of the airplane during the flights were recorded synchronously to the radar data.

As an example, throughout the radar acquisitions in Finland during the 15 of March, due to wind conditions, the airplane pitch angle was between 5° and 8° , the positive sign indicating that the tail of the aircraft was going down and its nose pointing upward. The major consequence of flying with a non-zero pitch angle is a rotation in the radar polarization. This aspect has been investigated by means of simulations for the Ku Band. Figure 32 shows the nominal radiation E- and H-planes in the case of an ideal flight, and in the case of a 7° pitch tilt of the aircraft (and consequently of the radar antennae) during the flight. The main beams of the antenna radiation patterns remain practically unchanged, meaning that the modification of the horns antenna radiation pattern, induced by small pitch rotations of the aircraft, is insignificant in the main beam angular region.

The yaw angle was influenced mostly by the direction of the wind during the acquisitions. Angles between -10° and -5° were recorded in the analyzed acquisitions, the minus sign representing a rotation of the airplane nose toward the left wing.

In order to compare GPS-IMU data with information derived from radar data, the Doppler centroid was estimated as the barycentre of the radar returns in the range-Doppler plane. The Doppler centroid gives an indication of the antenna pointing direction. This value was used as an initial check to verify, from the measured data, the consistency of the angles computed from the GPS-IMU data.

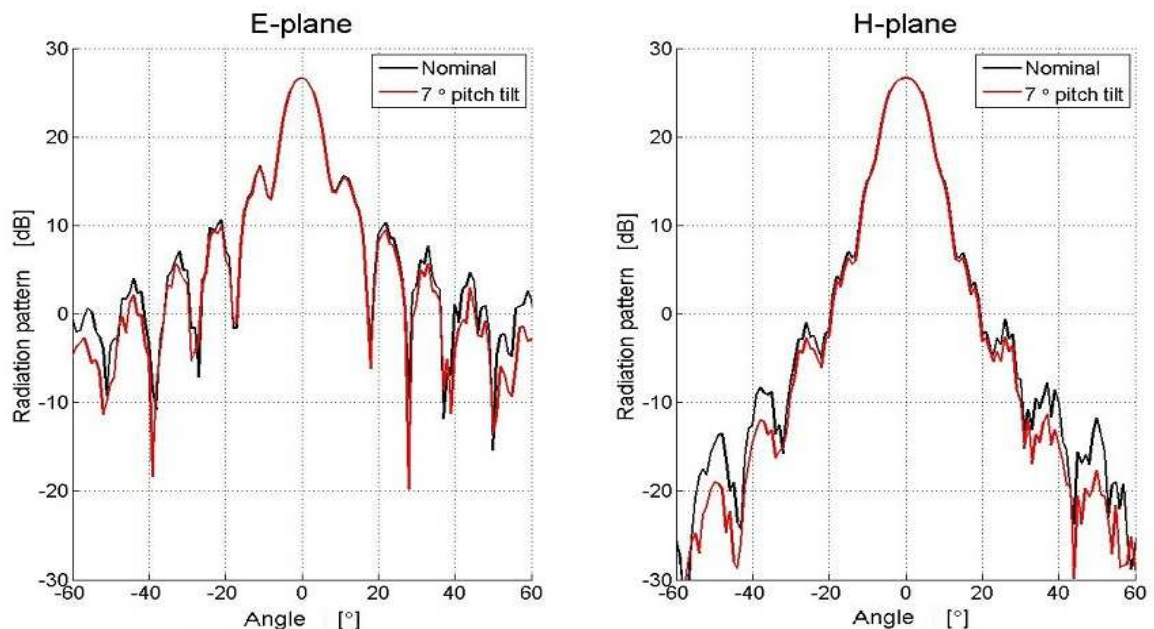


Fig. 32: Influence on the antenna radiation patterns of an aircraft tilt angle during the acquisitions of 7° in the pitch for the Ku band.

6.2 Antenna pattern

In order to evaluate the radiometric error introduced by an improper correction of the antenna pattern, simulations have been performed and the results are hereby given. The radiometric inaccuracy, resulting from an antenna pointing imprecision, is derived and quantified. Main causes of antenna pattern reconstruction errors are the accuracies of the GPS-IMU and of the Digital Elevation Model (DEM) available.

6.2.1 Elevation plane

The main cause of antenna pattern reconstruction errors in the elevation plane is the airplane roll angle inaccuracy. In Figure 33, the radiometric error (power in dB), across the main beam in the elevation plane (nominal elevation angle), associated with an antenna pointing shift (as in legend) is represented, at the X-band. In the elevation plane, at X-band, the one-way 3dB beamwidths are 12° and 17° for the vertical and horizontal polarization, respectively.

It should be noted how every curve in the plot relates an airplane roll inaccuracy to a consequent radiometric error. It results that, for roll shifts below the GPS-IMU accuracy RMS¹, the radiometric error is below 0.05 dB, in all three polarization configurations studied and for all the angles in the main beam of the elevation antenna pattern.

More relevant antenna pattern errors can be induced by possible inaccuracies in the knowledge of the ground topography. A flat terrain is assumed while processing the acquired SAR data; this is not always the case, and this un-ideality in the DEM model may result in antenna pointing shift angles in the order of some decimal fractions of degree, up to 1° (see paragraph 6.2.3). When increasing the angle shift error up to higher values, the radiometric error starts to become larger, particularly at the edges of the antenna beam.

For a shift angle of 0.5°, in the VV case, the error reaches 0.3 dB already at 1° off the nominal elevation angle and it increases up to more than 1 dB at the beam edges. The error in the HH is smaller than that in the VV, because of the larger antenna beamwidth in the elevation plane; the cross-polar configuration gives an error that is in between the ones found for the co-polar configurations, because it is given by a combination of both the V and H antenna patterns.

This analysis of the radiometric error, as function of the antenna pointing inaccuracy in the elevation plane, demonstrates the importance of having available an accurate DEM of the area where a calibrated SAR image is being acquired.

¹ 0.028° is the roll accuracy RMS of the RTK positioning mode with an outage duration of 60 seconds [7].

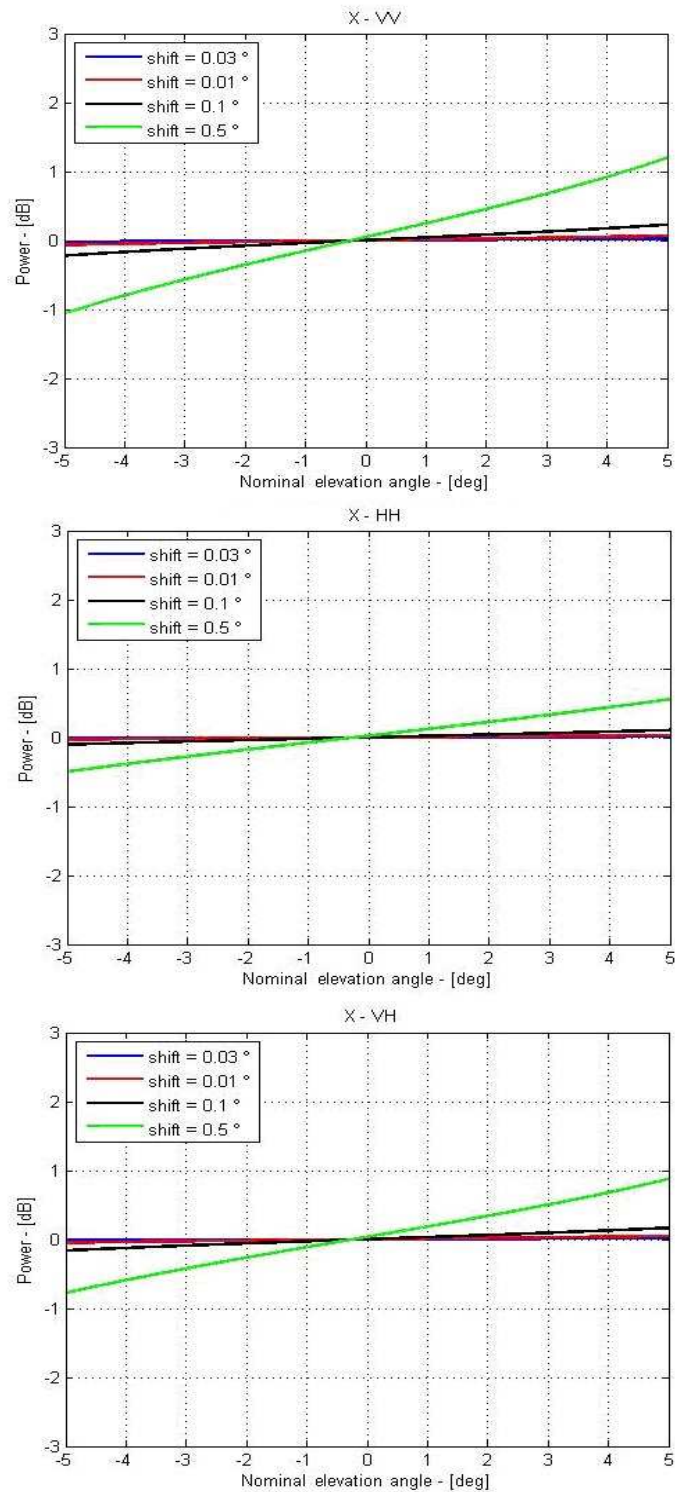


Fig. 33: SnowSAR radiometric errors at X-band for different inaccuracy roll shift values and for different TX-RX polarization configurations: top VV, middle HH, bottom VH.

At Ku-band, in the elevation plane, the one-way antenna 3dB beamwidths are 8° and 12° for the vertical and the horizontal polarization, respectively. Simulated results of the radiometric errors for the Ku-band are given in Figure 34. Regarding the VV configuration, the radiometric errors for small inaccuracy roll angle shifts (in the order of the GPS-IMU roll accuracy RMS) are below 0.07 dB in the elevation main beam, so still limited, even if not negligible. The same cannot be stated for shifts in the order of 0.1° and higher, typical range of errors in case of DEM uncertainties. For example, in the VV case, considering a 0.1° inaccuracy roll shift, the simulated radiometric error increases up to more than 0.5 dB at 5° of nominal elevation (at the edge of the main beam). This behavior is even more evident for the 0.5° shift case, which is still a small antenna pointing misalignment. Here the radiometric error increases up to more than 0.5 dB at 1° in the nominal elevation beam (well beyond the set tolerance limit of 0.5 dB) and rises up to 3 dB at the edge of the antenna beam. Similar behaviors are observable for the other two polarization configurations, even if showing minor errors than with the VV case, as it happens for the X-band case.

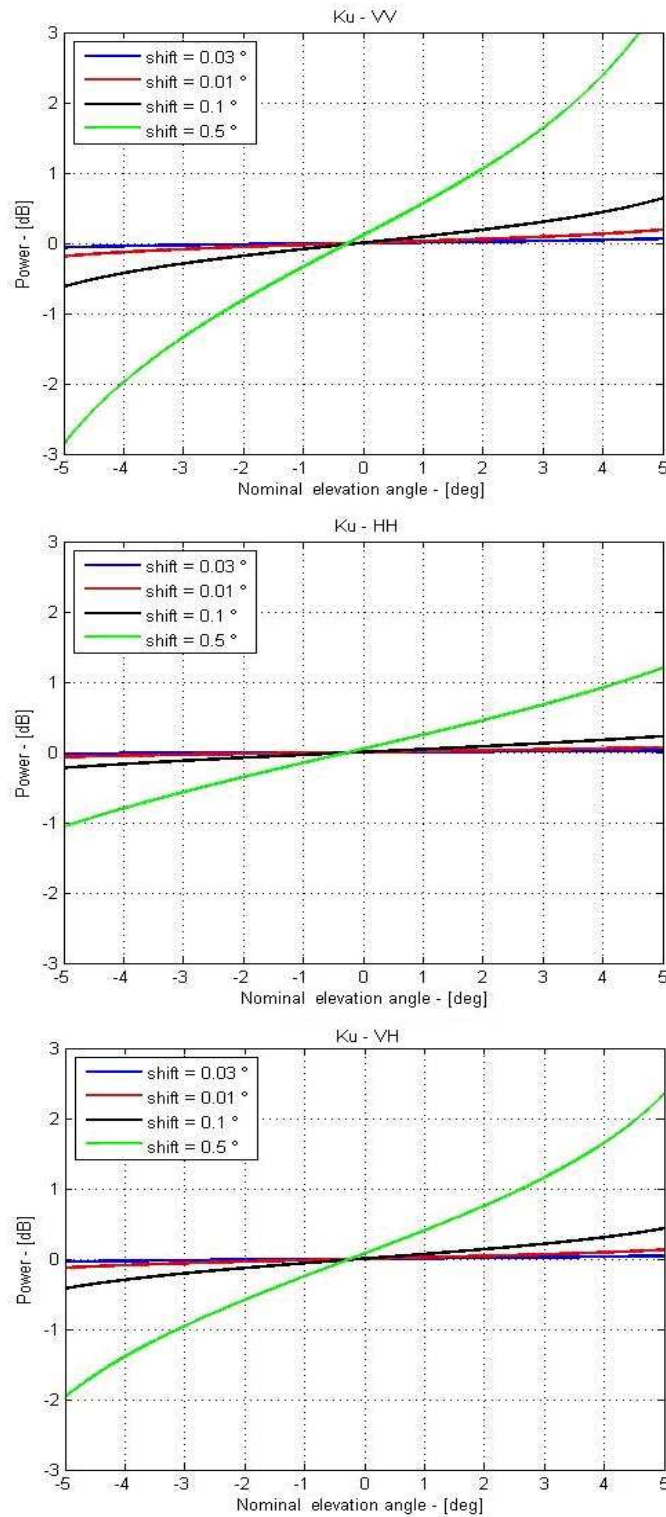


Fig. 34: SnowSAR radiometric errors at Ku-band for different inaccuracy roll shift values and for different TX-RX polarization configurations: top VV, middle HH, bottom VH.

6.2.2 Azimuth plane

Two main parameters influence the accuracy of the reconstructed azimuth antenna pattern, namely the processed Doppler bandwidth and the Doppler centroid shift. The considered Doppler bandwidths range from ± 100 Hz up to ± 700 Hz, for the X- and Ku- band respectively. The Doppler centroid shifts range from 10 Hz up to 200 Hz.

In X-band, the presence of Doppler centroid shifts causes radiometric errors that can be considered negligible for the three considered polarization configurations, at least for shifts in the order of 40 Hz, representing a plausible value in a real-case scenario. For these Doppler centroid shift values the radiometric error is below 0.05 dB (Figure 35, left). For larger amounts of Doppler shifts, these errors reach higher values. In particular, for Doppler centroid shift values higher than 50 Hz, the radiometric error reaches values in the order of 0.15 dB or 0.2 dB, depending on the amount of processed Doppler bandwidth, and on the polarization configuration. The radiometric error is still under the set tolerance limit of 0.5 dB at 80 Hz Doppler shift, for processed Doppler bandwidths larger than 500 Hz in the VV case and for processed Doppler bandwidths larger than 600 Hz in the HH and VH case.

A similar trend of the radiometric error can be observed in the results derived at the Ku-band (Figure 35, right). In fact, also at this frequency, for Doppler centroid shifts lower than 50 Hz, the amount of radiometric error in all the three polarization configurations can be considered negligible, for all the considered values of processed Doppler bandwidth. For higher Doppler centroid shift values, the behavior changes from one polarization configuration to another. In the VV configuration, at 100 Hz, the radiometric error is in the order of 0.25 dB for all processed bandwidths, whereas large radiometric errors in the order of 0.35 dB occur for the HH and VH configuration.

From the results obtained from the previous simulations, we can recognize that processing Doppler bandwidths in the order of 600 Hz - 650 Hz at X-band, and Doppler bandwidths in the order of 700 Hz at Ku band, for Doppler centroid shifts within the 80 Hz, the radiometric error that is caused, is quite limited (around 0.25-0.3 dB) and, anyway, under the set tolerance limit of 0.5 dB.

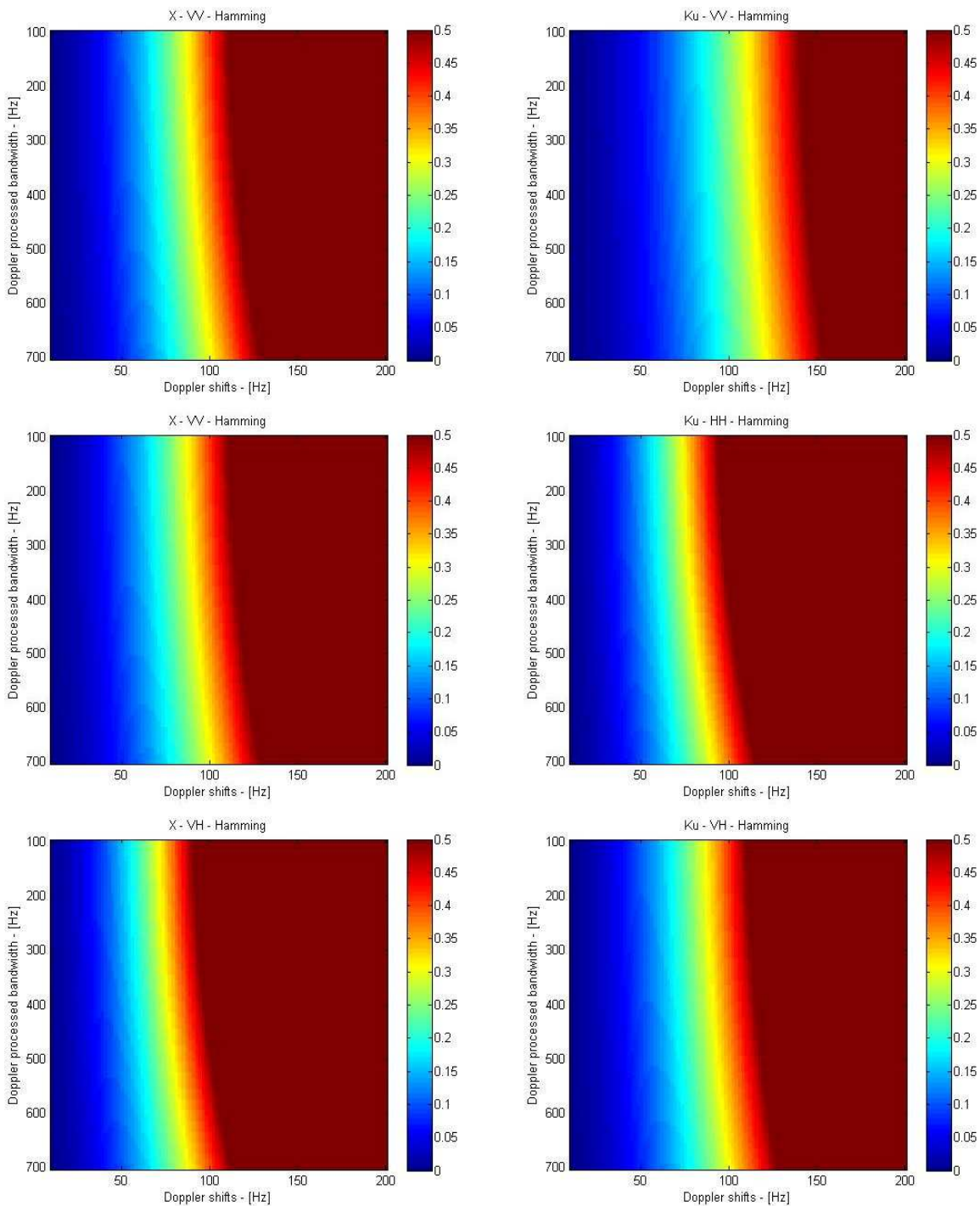


Fig. 35: SnowSAR X-band (left) and Ku-band (right) radiometric error [dB] for different polarization configurations (top to bottom), induced by the considered Doppler centroid shifts for different processed Doppler bandwidths. A Hamming filter is applied for side-lobes suppression.

The plots of Figure 35 are obtained using a Hamming window as large as the processed Doppler bandwidth. Concerning the filtering process, a multi-look method can be used instead of the Hamming one.

By using a 350 Hz large Hamming window and shifting it into the processed Doppler bandwidth, it can be seen in Figure 36 that the radiometric error due to Doppler centroid shifts is reduced. In particular, the curves in the plots refer to the case in which the overlapping between two following Hamming windows is half (175 Hz) of the Hamming window for the Ku- frequency band. In the case of 700 Hz processed Doppler bandwidth there are 3 Hamming "looks", while in case of 1050 Hz processed bandwidth the number of Hamming "looks" rises up to 5.

This multi-look processing approach leads to a smaller radiometric error, as shown by the following example for the Ku-band frequency, for which the radiometric error obtained with the two approaches is compared for a fixed Doppler shift (i.e. 100 Hz) and for 700 Hz processed Doppler bandwidth. By considering both the solutions of one large Hamming window (Figure 35, right top) and of 3 Hamming windows, the radiometric error reduces from 0.25 dB in the first case to 0.2 dB in the last case (Figure 37 top). The error reduces even more, up to very small values (0.02 dB) if the processed bandwidth is increased up to 1050 Hz.

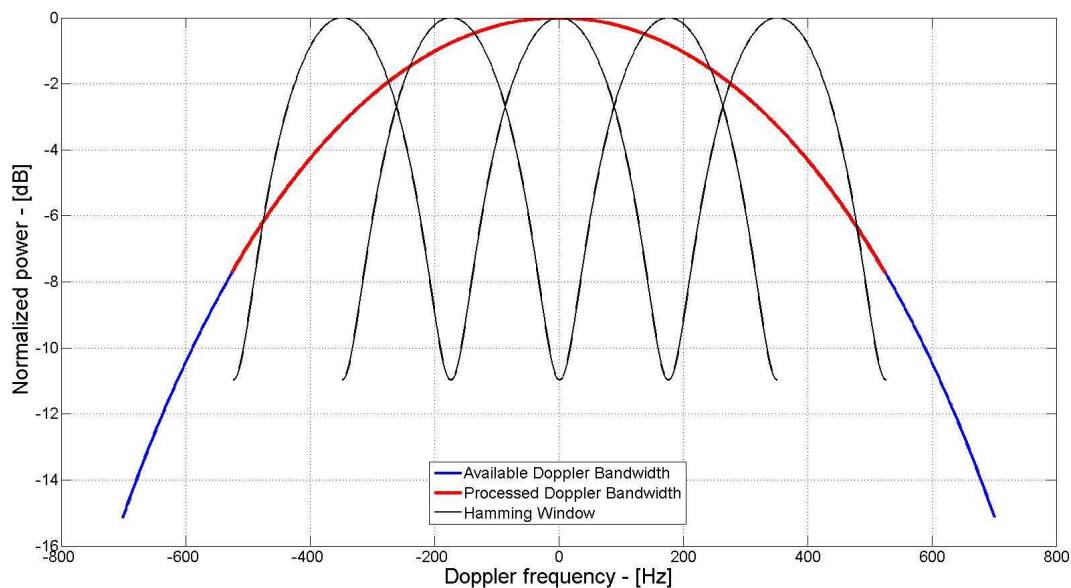


Fig. 36: Hamming multi-look filtering in case of 1050 Hz processed Doppler bandwidth.

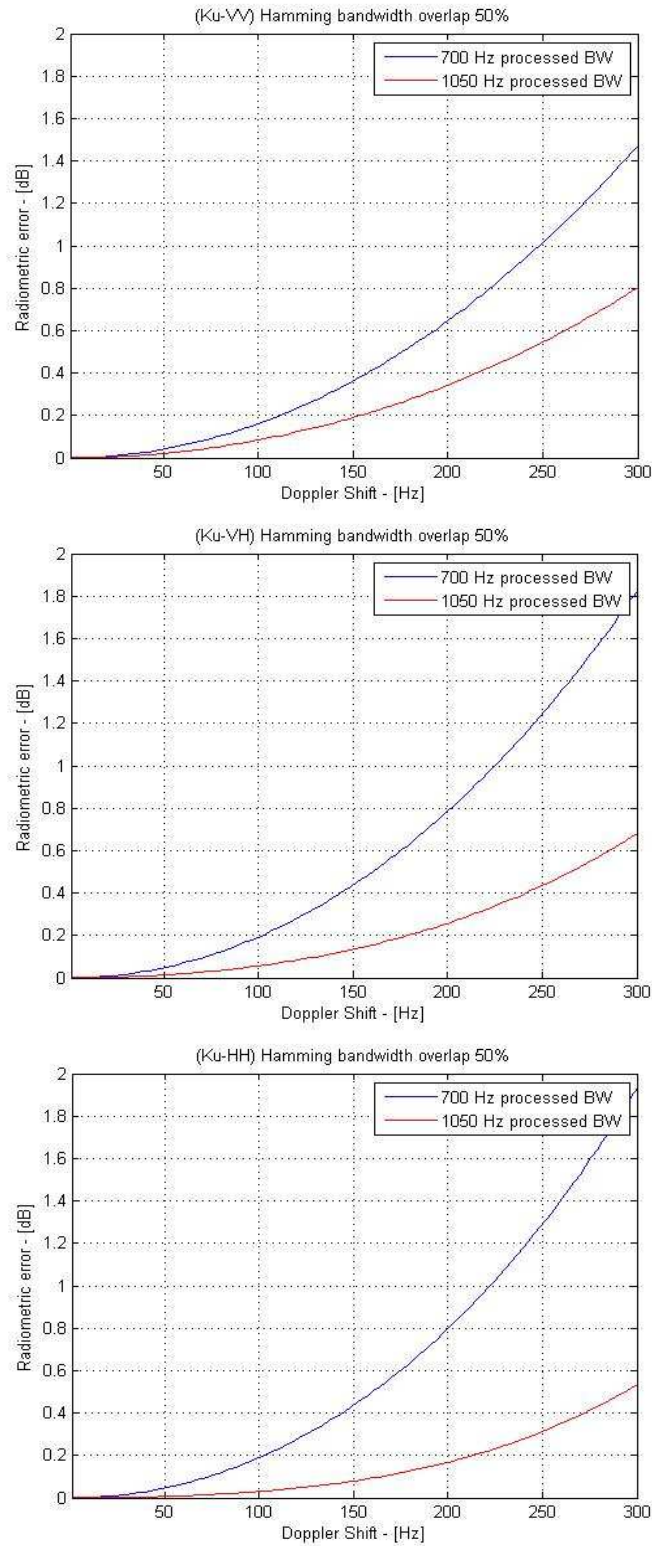


Fig. 37: Radiometric Errors using a shifting hamming window 350 Hz large with an overlapping of the 50% of the window bandwidth (175 Hz) for the Ku-band frequency

6.2.3 Systematic error from DEM inaccuracy

A proper knowledge of the ground topography is required in order to perform an optimal radiometric antenna pattern correction. However, due to the lack of a DEM model of the area under investigation, the assumption of a perfectly flat land at a quote of 200 meters has been taken into account. Simulations have been performed to estimate the amount of *systematic* radiometric errors introduced by the above mentioned hypothesis.

Based on acquisition look angle of 40°, on elevation beamwidth of 10° and on a nominal topography height of 200 m, the relative slant range distances have been estimated for a flight altitude of 1600 m. It is to be noted that aircraft altitude variations within few tens of meters (as the typical ones happening during an acquisition) do not introduce important differences with respect to what is here shown; moreover the flight quote is accurately known by the GPS-IMU recorded data.

Assuming a maximum variation of ± 20 m within the considered topography, the induced elevations offset angles and the consequent radiometric errors have been simulated for the X- and Ku- frequency bands (characterized by different beamwidths), and results are given in Figures 39 and 40.

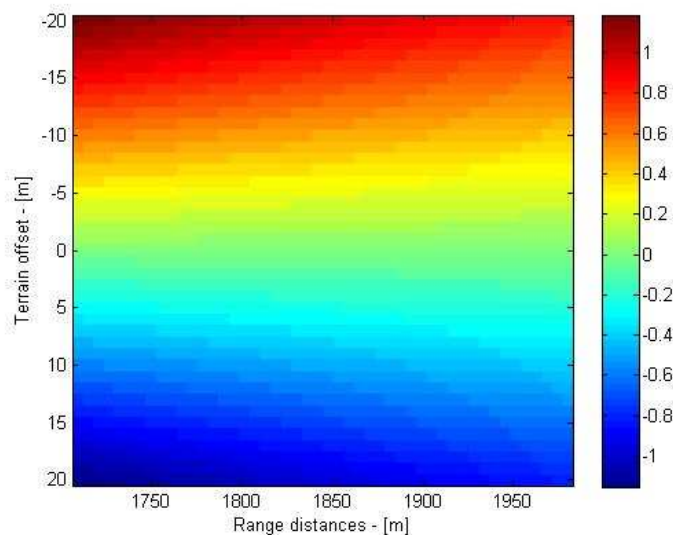


Fig. 38: Elevation angle offsets [°] induced by DEM altitude errors.

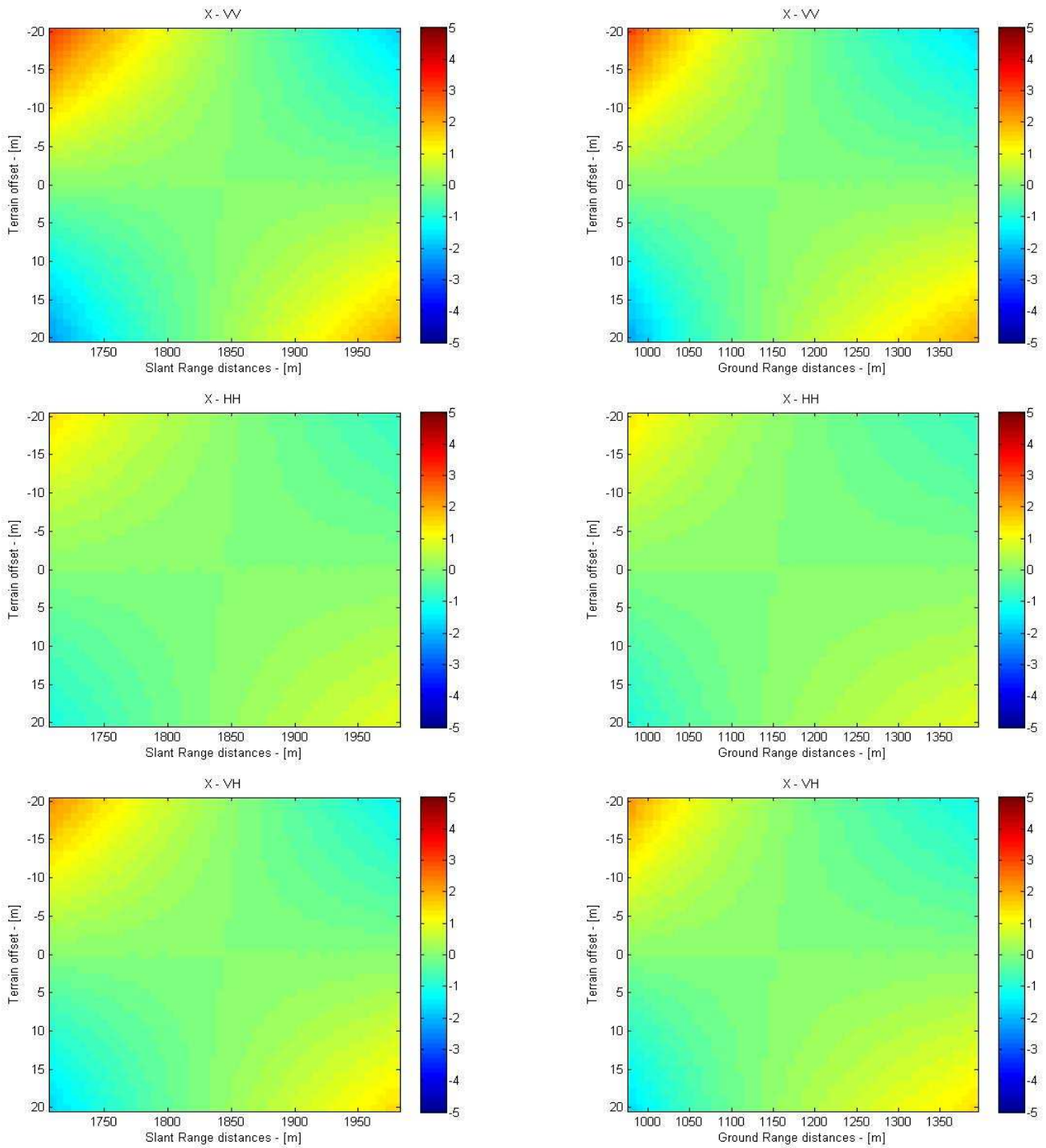


Fig. 39: SnowSAR X-band - Radiometric errors [dB] caused by topographic variations, in terms of slant range distances (left) and of ground range resolution cells (right) for different TX-RX polarization configurations: top VV, middle HH, bottom VH.

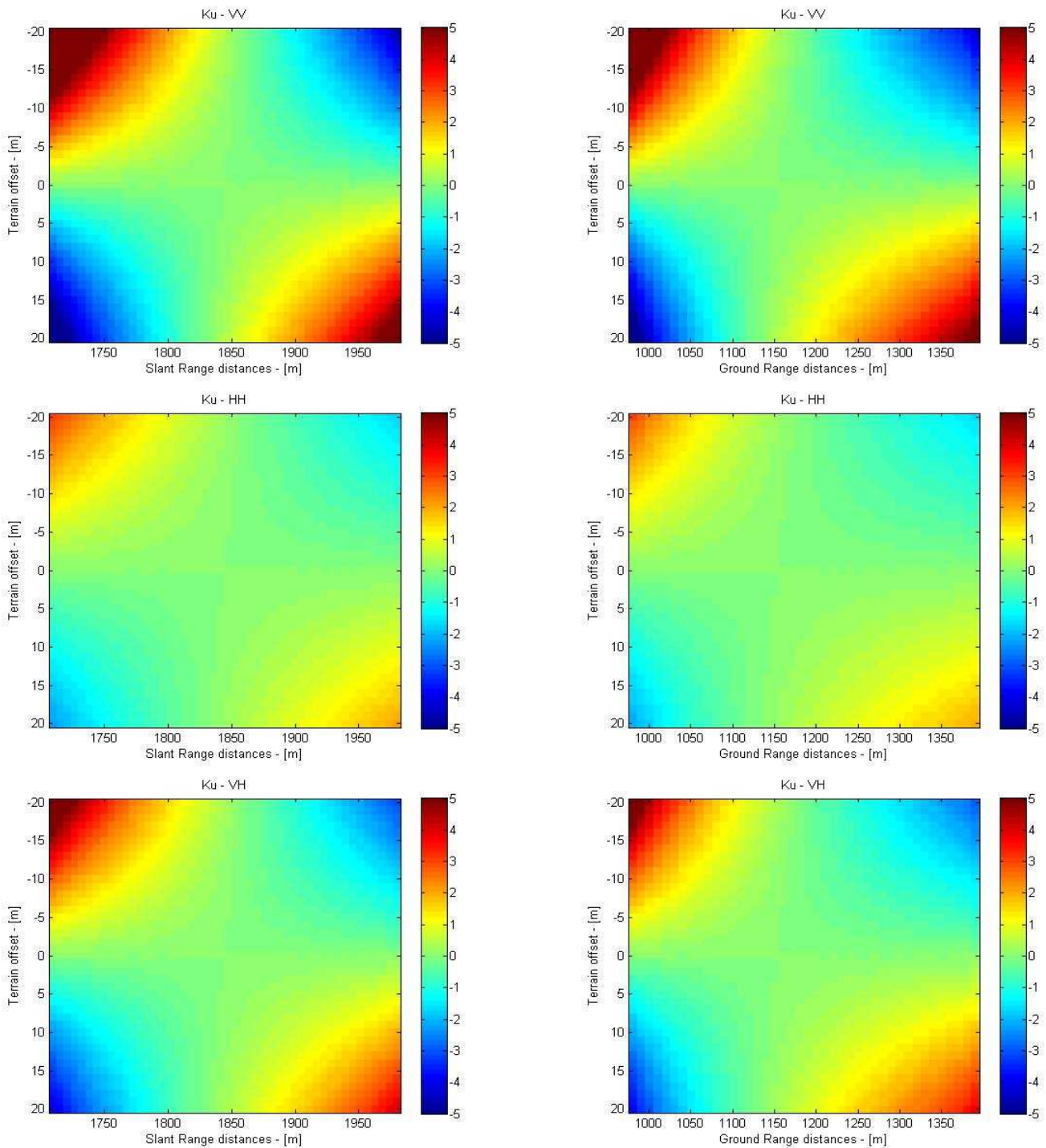


Fig. 40: SnowSAR Ku-band - Radiometric errors [dB] caused by topographic variations, in terms of slant range distances (left) and ground range resolution cells (right) for different TX-RX polarization configurations: top VV, middle HH, bottom VH.

In particular, in Figure 39 the elevation angle offsets induced by changes of topography altitude are shown. The angle offsets are in the order of 0.2° - 0.4° already for 'modest' 5 m variations, increasing up to more than 1° for altitudes errors of 20 m. The obtained elevation offset values are important, potentially causing remarkable radiometric error. As an example let consider the VV configuration at X-band (Figure 39, top): for a 5 m error in the DEM estimated altitude, a radiometric error of 0.7 dB in the far range is obtained. Radiometric errors of 1.8 dB or 2.4 dB can be reached when the topography errors increase to 15 m or 20 m, respectively. The same can be observed for the other analyzed polarization configurations, HH and VH, where the maximum radiometric errors are slightly smaller with respect to the VV case (because of the bigger beamwidth, less sensitive to small offset angles).

Even a worst scenario is observed for the Ku-band, where the radiometric errors are larger than those found for the X-band, see Figure 40. As an example, for the VV case the radiometric error is more than 1 dB for 5 m altitude variation, and it rises up fast to 6 dB for the far range in case of a 20 m height error of the DEM (Figure 40, top). Similarly, the other two polarization configurations show that the amount of the radiometric error increases by increasing the topographic error.

An important conclusion from these simulations is that even smaller topographic variations which are not taken into account within the DEM can strongly affect the radiometric calibration, causing very large errors. It is evident the importance of an as accurate as possible DEM. Topographic variations in the same order of the simulated one characterize the landscape which has been measured by the SnowSAR during the Finnish campaign. This can lead to potential radiometric errors beyond the required limits.

The radiometric errors considered up to now can be defined as *absolute*, since they remain constant within acquisitions over repeated passes. On the other hand, next analysis deals with *relative* radiometric error, arising by different data takes acquired within a trajectory lying in 40 m diameter orbit tube. Figure 41 shows that, by adopting flight trajectories into such an orbit tube, the relative radiometric error caused at X-band by a topographic variation of 5 m are quite limited for both the considered polarization configurations. In the case of 10 m topographic variation the relative radiometric error increases, reaching values in the order of 0.2 dB.

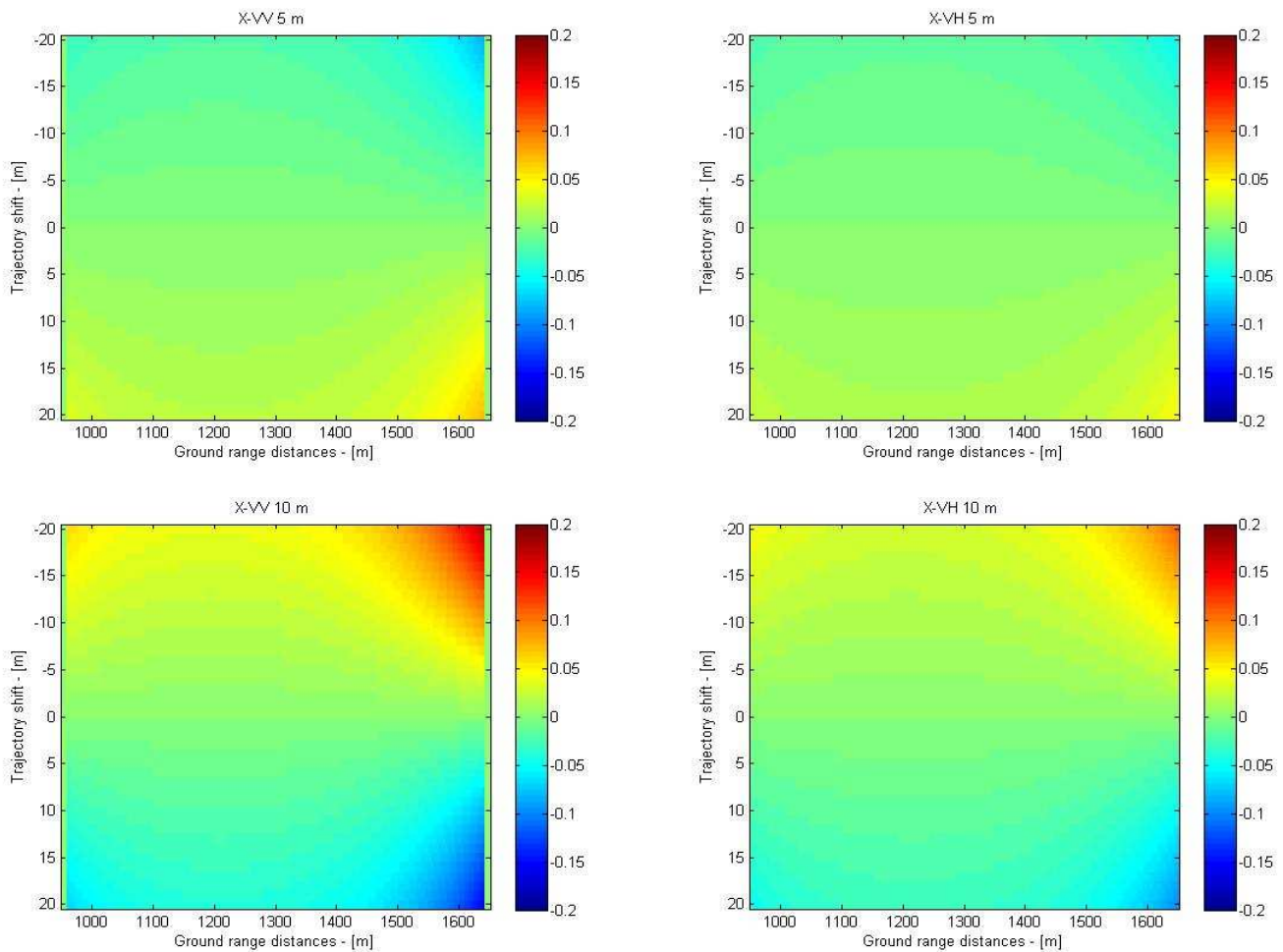


Fig. 41: SnowSAR X-band - Relative radiometric errors [dB] caused by topographic variations, for horizontal trajectory shifts up to 20 m and for topographic variations of 5m (up) and 10 m (down).

Similar analysis has been carried out for the Ku-band, and the correspondent results are shown in Figure 42. In the previous figures it can be observed that, for trajectory shifts smaller than 10 m, the relative radiometric error due to a 5 m topographic variation is quite limited. However, for trajectory shifts larger than 10 m, this error can be more relevant. This trend is even more evident for the 10 m topographic variation case, where already for small trajectory shifts the relative radiometric error is in the order of 0.5 dB.

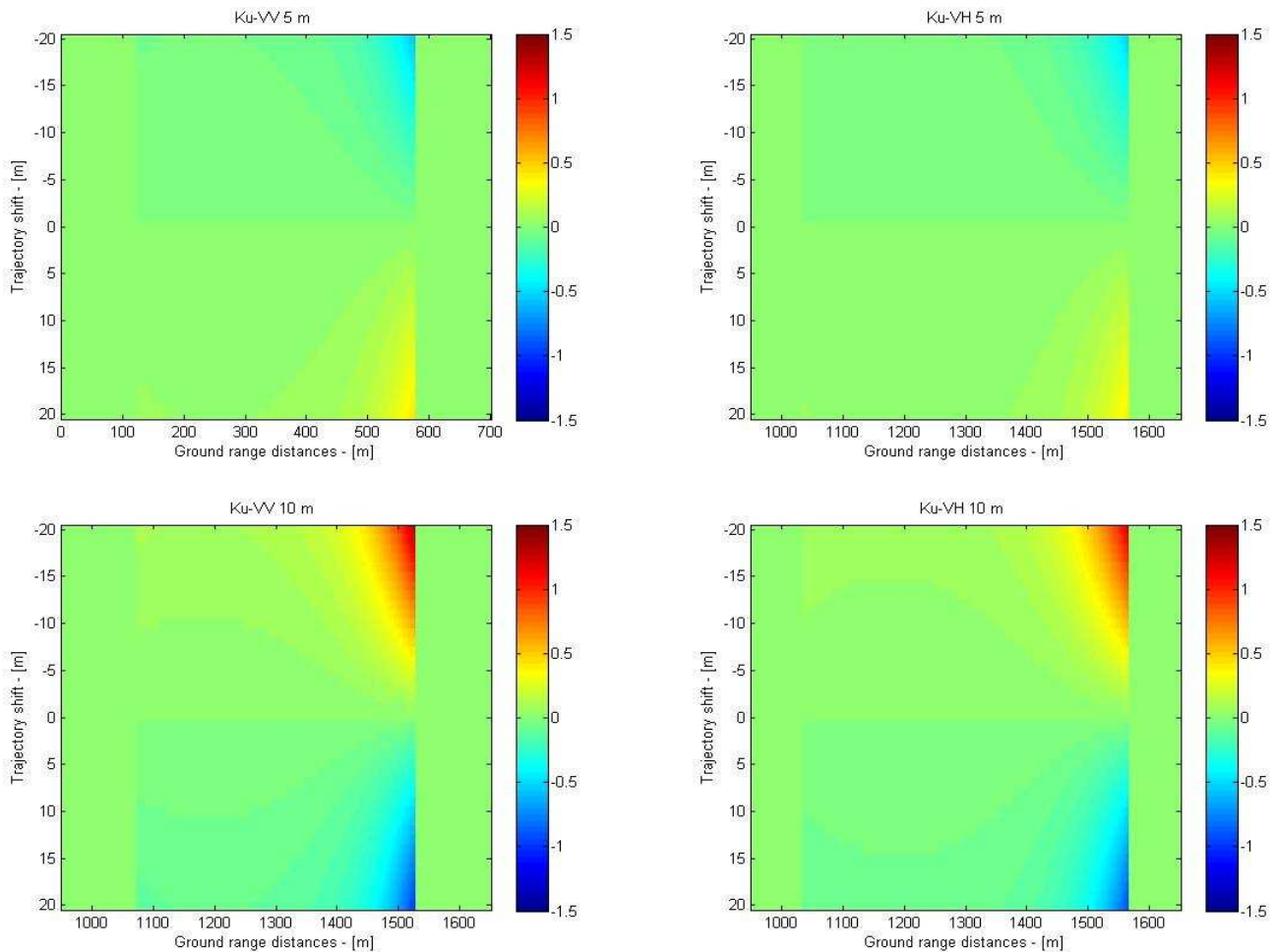


Fig. 42: SnowSAR Ku-band - Relative radiometric errors [dB] caused by topographic variations, for horizontal trajectory shifts up to 20 m and for topographic variations of 5 m (up) and 10 m (down).

However, keeping the focus on the antenna 3 dB beamwidth and considering a maximum possible trajectory shift of 10 m, the magnitude of these kind of error is limited. In the Ku-band, the relative radiometric error is slightly larger than the X-band case.

7 Data take initial analysis

In this section, a preliminary analysis is performed, of the data acquired with the SnowSAR during the campaign of March 2011 in Lapland. The analysis is carried out on one data take at Ku band, obtained on Tuesday March 15th during the flight trajectory 2 [3]. Radar images, a SNR analysis and a first calibration study on VV at Ku-band are presented in this section. No data is available at Ku- band from the flights of the 16th and the 17th of March. At X band, data are available on 15th, 16th and 17th March.

7.1 General considerations

The image analysis is carried out as follows: for each data take, a detected geo-coded picture is generated. Associated with each image, there is a co-registered image, in which each pixel indicates the index of the airplane's orbit when the corresponding SAR pixel has been focused. Both matrices are shown in Figure 43, top and bottom, respectively.

By combining the detected image with the orbit index information (see Figure 43), other information like the antenna elevation and azimuth pointing angle (see Figure 44) during the data take can be derived.

From Figure 44 (top), it can be observed that during the data take a generic point at a certain ground range was seen under different angles, due to the airplane roll motion. This variation, which can be quantified in a couple of degrees, points out the necessity of a larger beamwidth in the elevation plane for covering a larger swath with the antenna beam.

In Figure 44 (bottom), a variation of the azimuth antenna look angle during the acquisition is visible, compatible with the yaw angles recorded during the data take. The vertical stripes in figure show that, as expected, points at different ground range but corresponding to the same acquisition bin during the trajectory are illuminated under the same azimuth angle.

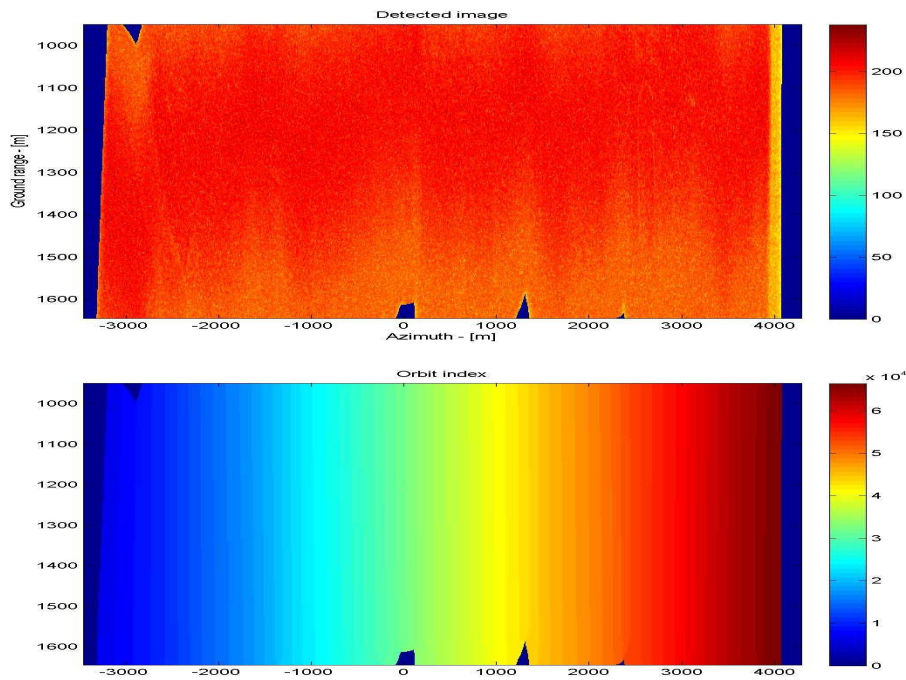


Fig. 43: Detected image relative intensity [dB] and corresponding orbit index for each focussed point in the detected image. The considered radar swath is more than 600 m and the acquisition strip is longer than 7 km. By combining this information, more features can be derived. Azimuth and ground range correspond to the X_{img} and Y_{img} indicated in Figure 17.

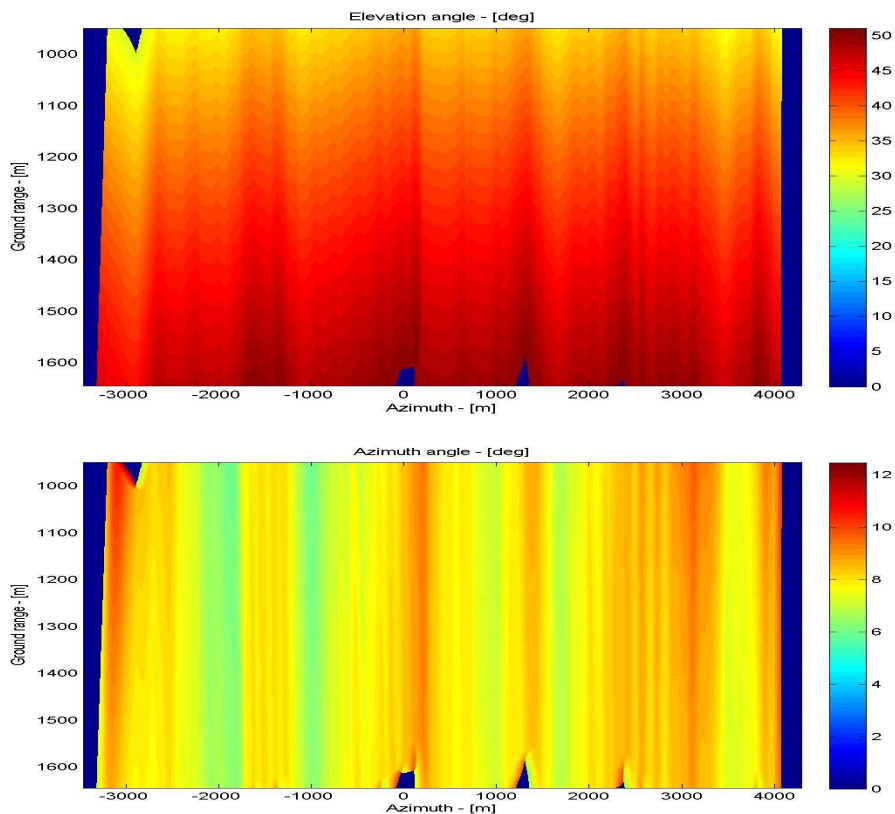


Fig. 44: Antenna pointing direction, in elevation (a) and azimuth (b), during the considered data take and for the different ground ranges. Azimuth and ground range correspond to the X_{img} and Y_{img} indicated in Figure 17.

An important remark is relative to the importance of having an accurate DEM available for the images generation. Laser scanning data have been purchased from the National Land Survey of Finland (NLS), characterized by a grid resolution of 2 meters, and by an elevation accuracy of the points up to 15 centimeters, to be included in the SnowSAR processing chain. Due to delivery time issues, however, this information has not been included in the preliminary analysis discussed in the following sections, whose images are generated by assuming an almost flat terrain, characterized by a ± 20 m variation around an altitude of 200 metres. Nevertheless, an example of the same image achieved by using the DEM information is given in section 7.2.1.

7.2 Data take example

As a first example of Ku-band calibrated image achieved without knowledge of the terrain altitude, a data take over the SnowSCAT centre is shown in Figure 45. The processed area covers an extension of 6.5 Km in azimuth, and 600 m in ground range. The elevation beam has been limited to the $[35^\circ, 45^\circ]$ range. Both co-polar and cross-polar images present a high SNR. Even if from a SNR point of view it results ok, the calibration at the edge is worsened.

A number of features can be distinguished: the corner reflectors are clearly visible (bright white dots) in the bottom-left part of the image. The EISCAT parabolic dish antenna (32 metres of diameter) is located within the Artic Research Centre of Sodankyla, and it can be pointed out in the figure as a white dot in proximity of the corner reflectors (see arrow). The bright area on the top-right image is a consequence for the lack of a DEM, as explained in the following sub-section 7.2.1.

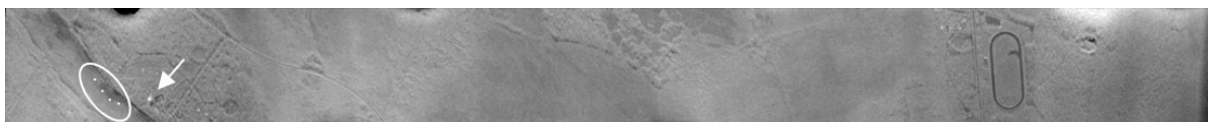


Fig. 45: Ku-band co-polar (VV) image relative to the analyzed data take (transect Nr. 2), obtained without knowledge of an accurate terrain model. The four corner reflectors placed along the frozen river are clearly visible as bright white dots in the left part of the images. Also, the EISCAT parabolic dish antenna (32 metres of diameter) of the ARC is easily identifiable on the figure (see arrow).

For each data take at a certain polarization, 6 sub aperture images are generated by processing 350 Hz of Doppler bandwidth centred at different Doppler centroids. The different sub-apertures are overlapping 50 % in Doppler bandwidth. The images are incoherently averaged and then multi-looked to obtain a resolution of 10x10 meters.

It can be seen from Figure 45 how the trihedral reflectors do not cover the entire radar swath. Consequently, they provide only limited information about the antenna elevation pattern and a different method had to be adopted for the antenna elevation pattern estimation (see Section 5.2.2).

7.2.1 DEM knowledge

An accurate knowledge of the area topography allows for an enhanced image calibration. Figure 46 shows an actual DEM of the area monitored in Figure 45, from NLS.

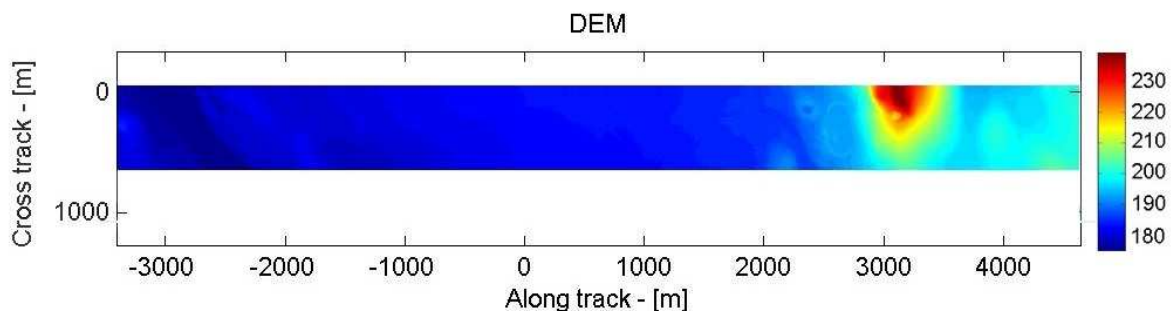


Fig. 46: DEM of the monitored area of Figure 45, from the National Land Survey of Finland.

A difference in altitude of more than 50 meters can be noticed in the right part of the DEM: the assumption of about ± 20 m variation around the 200 metres is not realistic, and it represents the cause for the bright area of Figure 45. By taking into account the DEM shown in Figure 46, the image in Figure 47 has been generated. In this image, the bright area on the right part, due to an altitude variation of the terrain at near range, is no longer visible.



Fig. 47: Ku-band polarimetric image relative to the analyzed data take (transect Nr. 2), obtained with knowledge of terrain model (see Figure 46). The same features of figure 45 can be noticed, but the bright area on the right.

Figure 48 shows an X-band co-polar (VV) image of the same area, acquired simultaneously with the Ku image presented in Figure 47. The correction taking into account the DEM information is being applied in the displayed picture.



Fig. 48: X-band co-polar (VV) image relative to the analyzed data take (transect Nr. 2), obtained with knowledge of terrain model.

7.3 Signal-to-Noise Ratio

One crucial design requirement for the SnowSAR was a Signal-to-Noise Ratio (SNR) level sufficient to achieve a noise equivalent sigma naught less than 28 dB (see Table IV). Figure 49 gives an indication of the obtained SNR at the Ku-band. In the figure, for each polarization mode, a profile of the radar returns at different slant ranges is derived from the range-Doppler spectrum of the image of Figure 45, by applying an averaging along the Doppler. A SNR between 25 and 30 dB is observed for all polarization configurations. It is remarkable how also cross-polar images have very high SNR. Other processed images at Ku-band show similar levels of SNR. The achieved SNR levels are to be considered very satisfactory and they comply entirely with the desired requirements of the SnowSAR project.

7.4 First calibration analysis on VV at Ku-band

In order to provide a radiometric calibration of a SAR picture like the one shown in Figure 47, the responses of the corner reflectors are used. The samples corresponding to the trihedrals locations are identified in the image, and the reflectivity of the overall image is normalized per unit area (called σ_0): in Figure 50 a zoom-in of the area where the trihedral reflectors are deployed is shown. From this plot, by employing the orbit index matrix, the look angles in elevation and in azimuth are derived in Figure 51, relatively to a pixel of the corner reflector number 2.

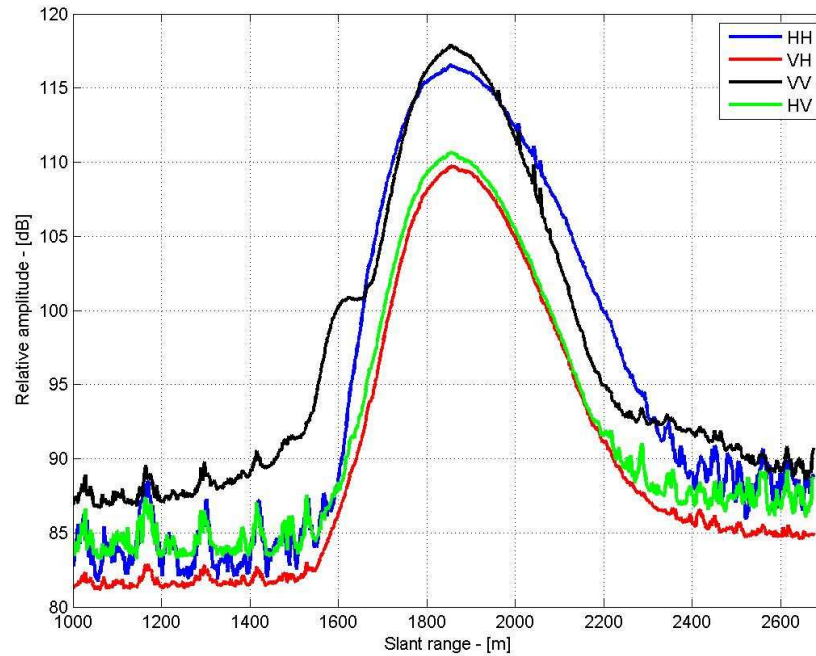


Fig. 49: A profile of the radar returns, at Ku-band, derived for all the polarization configurations from the range-Doppler matrix by applying an averaging in Doppler. SNRs between 25 dB and 30 dB are shown.

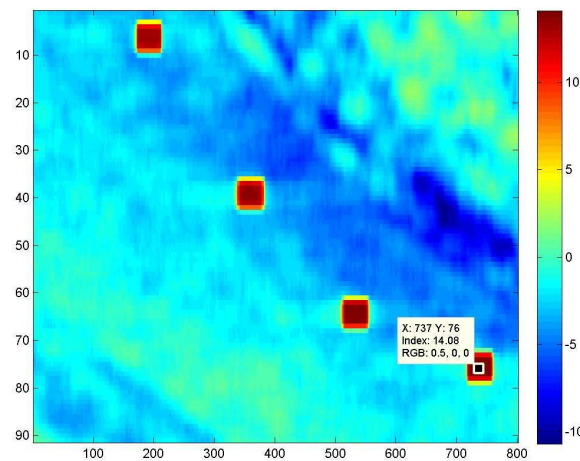


Fig. 50: Zoom-in of the intensity image on the area of the corner reflectors deployment. The colour bar indicates the backscattering coefficient, normalized per unit area (σ_0). The x and y axes represent samples in the azimuth and ground range directions, respectively. From the top to the bottom of the image, corner reflectors 3, 1, 4, 2 are shown.

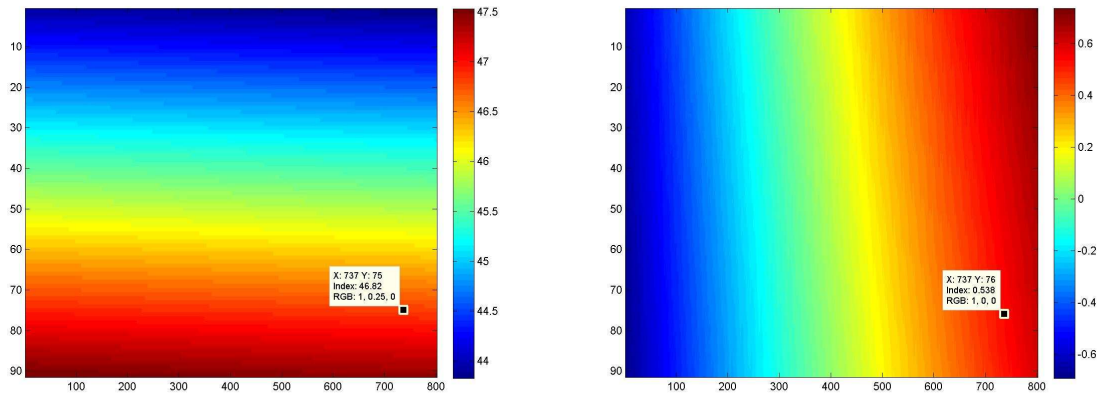


Fig. 51: Look angles [$^{\circ}$] between the ground pixels and the aircraft in elevation (left) and azimuth (right). The data tips relative to the corner reflector 2 are shown. The x and y axes represent samples in the azimuth and ground range directions, respectively, whereas the colour bar indicates the look angles in elevation (left) and azimuth (right).

Table II summarizes the azimuth and elevation angles [$^{\circ}$] between the ground pixels where the corner reflectors are located on the intensity image and the aircraft. Furthermore, the measured reflectivity per unit area σ_0 [dB] in the image and the expected reflectors RCS [dB] for the computed look angle are given.

Table II: Characteristics of trihedral reflectors

Trihedral reflector	[#]	3	1	4	2
Corner φ	[$^{\circ}$]	34.8	35.02	35.27	35.56
Corner θ	[$^{\circ}$]	44.13	45.5	46.43	46.82
Measured σ_0	[dB]	13.1	13.37	14.06	14.08
Expected σ	[dBm ²]	25.44	25.77	26.04	26.19

The profile of the measured σ_0 follows the predictions of the expected reflectors RCS. Moreover, the difference between the measured σ_0 and the expected trihedral RCS is practically constant for the different corner reflectors. It can be concluded that the correspondence, obtained in the results of the preliminary analysis so far shown, confirm that the adopted methodology would allow a reliable radiometric calibration of the acquired SnowSAR images.

8 Technical performance

The radiometric and geometric performances of the SnowSAR system have been estimated according to the results achieved within the Finnish measurement campaign, and they are summarized in this chapter.

8.1 Radiometric performance

The radiometric resolution γ was estimated from the measured mean value μ and standard deviation σ of the image intensity, by taking into account a distributed target, i.e. by using the following equation [8]:

$$\gamma = 10 \cdot \log\left(\frac{\mu + \sigma}{\mu}\right)$$

Figure 52 shows the selected distributed target areas used for the measurement, the results of which are listed in Table III.

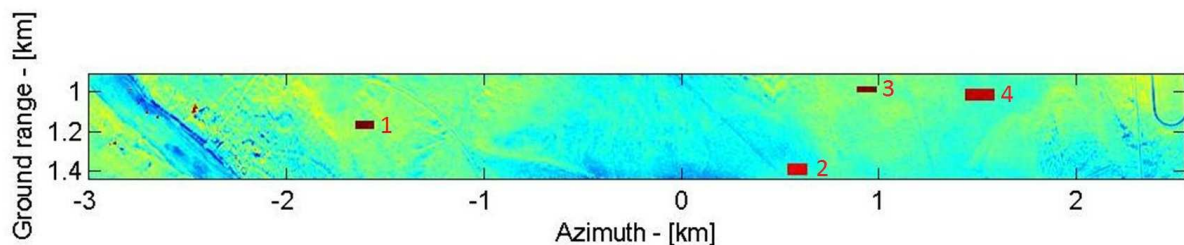


Fig. 52: Image used for the radiometric resolution verification. The rectangular areas in red (numbered from 1 to 4 in table III) have been selected for the analysis.

Table III: Selected areas: characteristics

	Area 1	Area 2	Area 3	Area 4
Azimuth extension [m]	100	100	100	150
Ground range extension [m]	40	60	28	56
Surface [m ²]	4000	6000	2800	8400
Radiometric resolution [dB]	0.879	0.642	0.98	0.7

Two acquisitions have been performed flying the same nominal track (nr.2). The produced images have been analyzed in order to compare their radiometric values. An elevation mask has been applied to the data in order to limit the produced SAR image to an antenna elevation interval from 37° to 43°, see Figure 53.

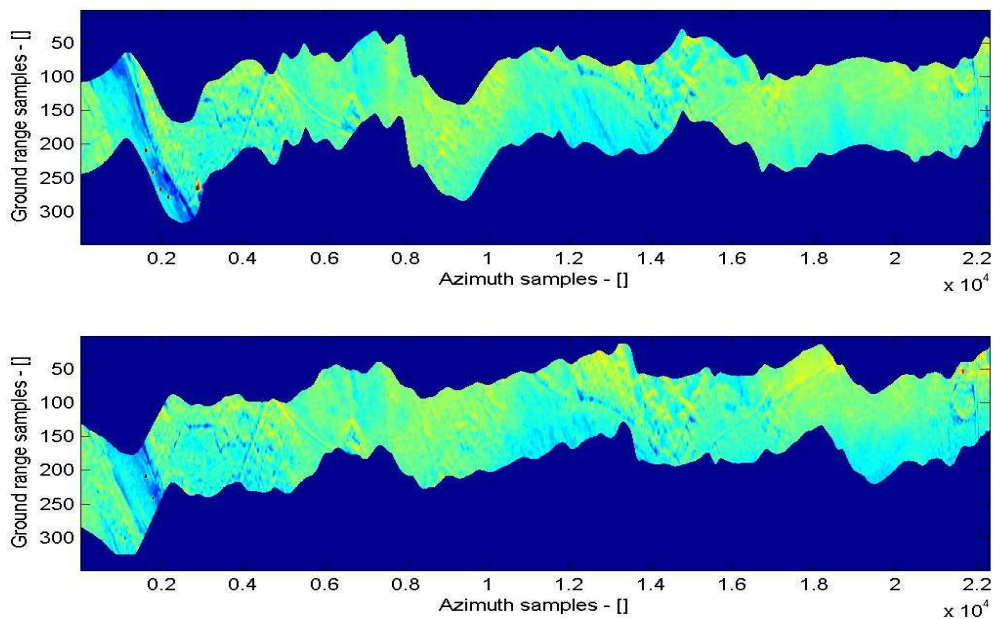
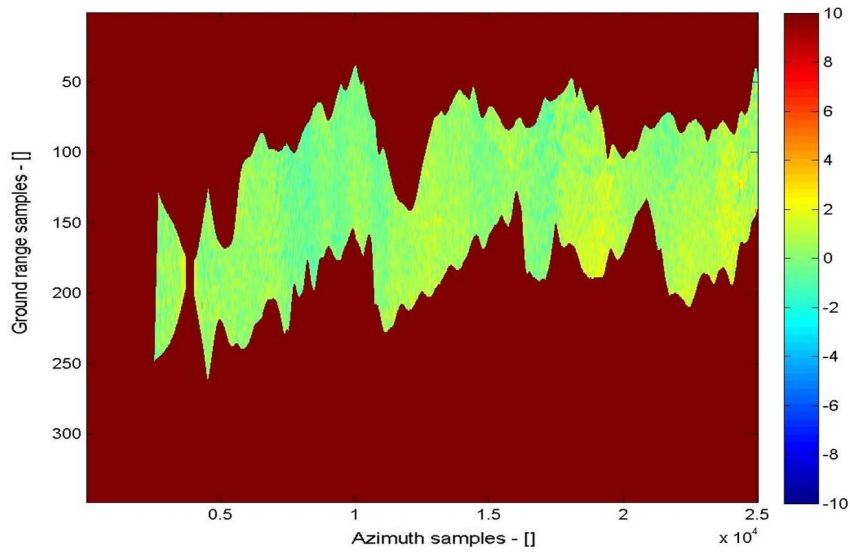
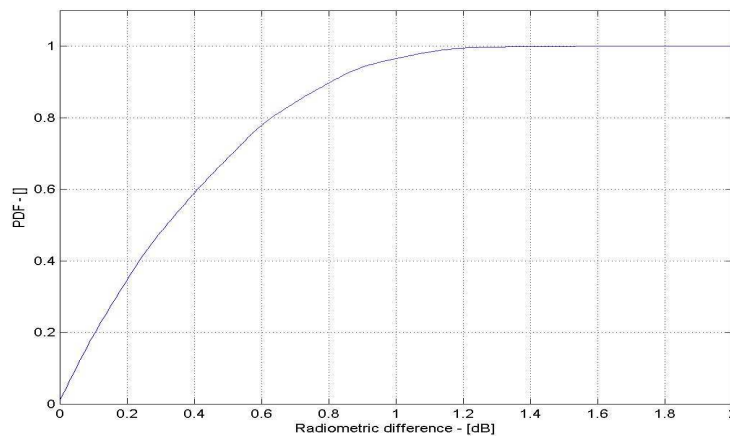


Fig. 53: Images used for the radiometric stability analysis of the SnowSAR.

The radiometric difference between the two plots of Figure 53 and the corresponding statistical cumulative distribution are illustrated in Figure 54. From the statistical distribution it can be estimated that the 60% of the radiometric difference between the two images is below 0.4 dB, while the 80% is below 0.8 dB. However, from the image of the radiometric differences, see Figure 54 (a), one can see that there are areas where those errors are concentrated. This is due to the fact that in those areas the cross-track difference of the trajectories during the two acquisitions is too high. This phenomenon can be minimized by using a wider antenna beamwidth in elevation, as the one that will be adopted in future missions (see section 9.1).



(a)



(b)

Fig. 54: Radiometric stability for the SnowSAR system. (a) Difference [dB] between the plots of Figure 53; (b) corresponding cumulative density function.

8.2 Geometric performance

The data collected by the SnowSAR are delivered with a resolution of 10 m x 10 m (ground range x azimuth). Before generating the image of the radiometric difference, the two SAR images have been geometrically co-registered. During this operation the offset in the two dimensions of small sub-patches are calculated, and subsequently the second image is re-sampled. The plots in Figure 55 illustrate the results of the co-registration process, as an indication of the relative geometric accuracy achieved during the SnowSAR focusing step.

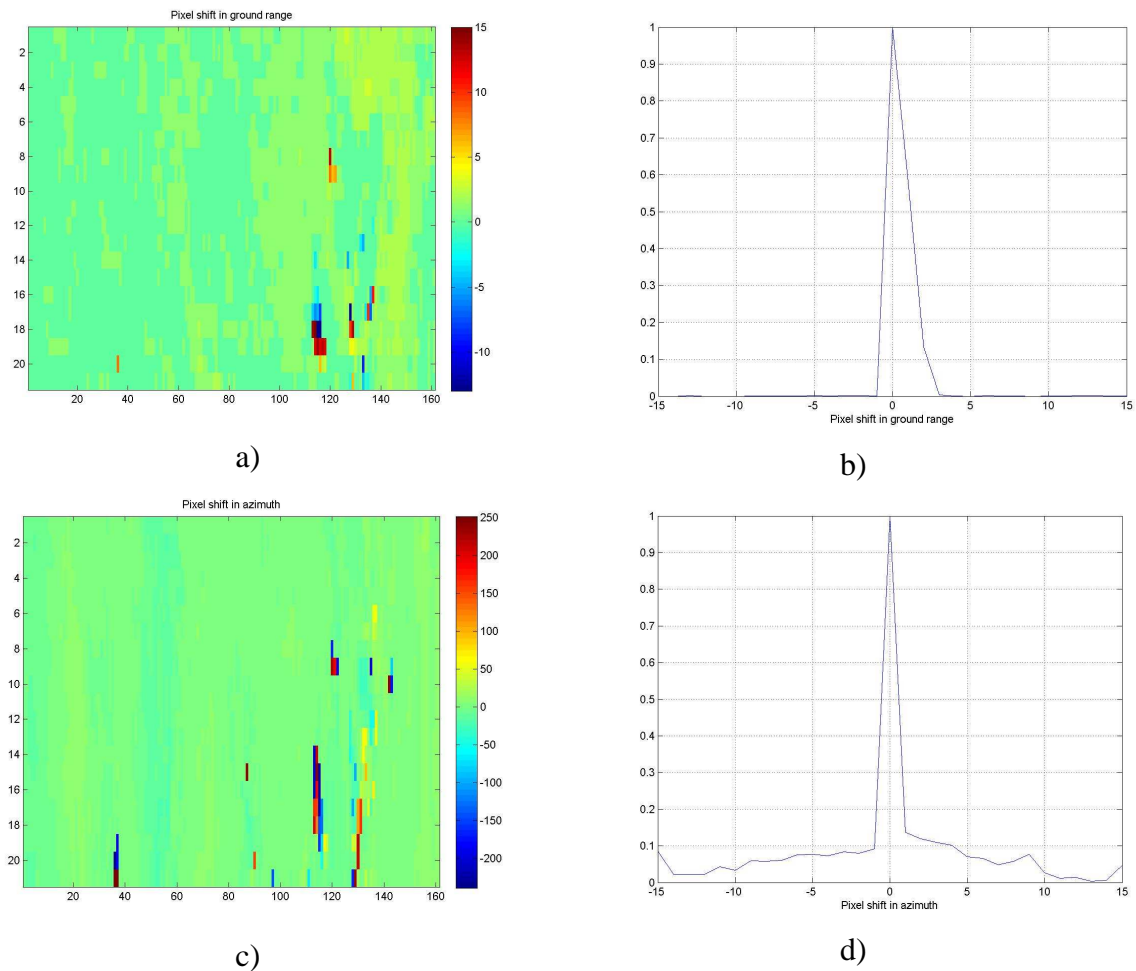


Fig. 55: Co-registration process: a) and c) calculated pixel shifts in ground range and azimuth respectively; b) and d) corresponding histograms.

A ground range pixel corresponds to 2 m, while each azimuth pixel is 25 cm. From the calculated histograms, a statistical relative geometric accuracy of less than 2 m in ground range and azimuth is estimated.

8.3 Performance summary

In the following table IV the original Agency requirements given in the Statement of Work (appendix A of [1]) for the SnowSAR system are given, together with the estimated performance of the system. Performance numbers which are not definitive are discussed more in at the bottom of the table.

Table IV: SnowSAR: Agency requirements and actual performance

System Parameter	Agency requirement	Actual performance
Minimum incidence angle range	30 ° – 45 °	Mean ant. look angle: 40 °
Frequency	Central frequencies between 9.5 and 9.8 GHz (X-band) and between 17.2 and 17.3 GHz (Ku-band)	Central frequencies 9.6 GHz (X-band) 17.25 GHz (Ku-band)
Spatial and Radiometric Resolution	200 ENL or greater for ground surface area of 10m x 10m	More than 200 ENL over a ground surface area of 10x10 m
Bandwidth	> 6 MHz	100 MHz
Polarization	VV + VH for both frequencies	VV + VH at Ku band (also fully polarimetric) VV + VH at X-band
Radiometric Performance		
Absolute bias	< 1dB	< 1dB *
Inter-channel bias	< 1dB	< 1dB **
Radiometric stability	< 0.5dB	60% < 0.4 dB St. dev 80% < 0.8 dB St. dev ***
Noise equivalent sigma naught	< -28dB	< -28
Swath width (minimum)	400 m	Larger than 400 m (the center of the swath varies with the roll angle of the aircraft) considering the SNR requirements. ****
Operating altitude	500-3000 m	1600 m
Operating conditions	-40° C to 20° C	Components rated for a [-40°, +50°] range; however, the system has been operated within an aircraft whose temperature has varied in the [-10°, +15°] C.

* This requirement has been met relatively to the corner reflectors area. In the remaining area this aspect is under investigation and it has to be verified.

** This parameter has been verified by tracking of the transmitted power at V and H polarizations and of the receiving gain.

*** Relatively to the case analyzed within this report (refer to section 8.1).

**** A proper antenna characterization was not achieved for the Lapland campaign data. The elevation beamwidth for which a proper radiometric calibration is achieved is limited to 250-300 meters. The variation in the swath centre with the roll angle is eliminated with the new antenna attitude stabilization mechanical gimbal.

9 Conclusions

The herewith document represents the final report concerning the technical assistance for the development and deployment of an X- and Ku-band mini SAR airborne system (the SnowSAR), commissioned by the Agency to the contractor (MetaSensing) as a support for further processing and analysis by other parties.

This report documents the airborne campaign performed with the SnowSAR instrument in the Lappish region of Finland during March 2011. Information about campaign execution is given, together with data acquisition and data processing detailed descriptions.

SnowSAR has provided, for the first time ever, coincident X- and Ku- SAR image data of land cover and snow fields from an airborne platform by using an instrument similar to that studied for CoReH2O.

The preliminary results confirm the internal stability and reliability of the SnowSAR instrument and indicate its suitability for investigations about the backscattering signatures of snow and of arctic landscapes in general.

An unforeseen extra-effort has been required in the antenna pattern reconstruction phase for external calibration. The reason is represented by the lack of an optimal corner reflectors configuration during the acquisitions performed with the fully working SnowSAR system (at both X- and Ku- frequency bands), on the 15th of March.

The SnowSAR is a completely innovative system and it is characterized by unique features. For this reason the first field measurement campaign documented in the present report has given many precious inputs to the MetaSensing team. In particular a gained technical and practical skill has been learned on how to operate the system. Most importantly, many indications have been deduced, which are valuable for eventual future optimization of the SnowSAR system. These are recapitulated in the following.

9.1 Lessons learned

In view of the polarimetric characteristics of the SnowSAR system and of the required low sensitivity of the transmitted power to temperature, horn antennas were adopted for the radar front-end, providing good radiation performance and high SNR within a low-risk solution (particularly in short time). However, being the horn aperture a square, they provide a narrow beam in both main planes (azimuth and elevation). This fact is a disadvantage in the elevation plane of the radar, where a larger beam is desirable for a larger swath and for a better radiometric compensation of misalignments due to the airplane motion and terrain irregularities. Microstrip array antennas could provide a suitable solution, with polarimetric capabilities and fan-beam radiation. Four dual-polarization microstrip antennae at X- and Ku-bands are being developed by MetaSensing, and they will be ready for September 2011. Moreover, a gimbal system for stabilization of the antennae pointing direction is now available at MetaSensing for measurement campaigns. In Figure 56 these two SnowSAR system enhancements are depicted.

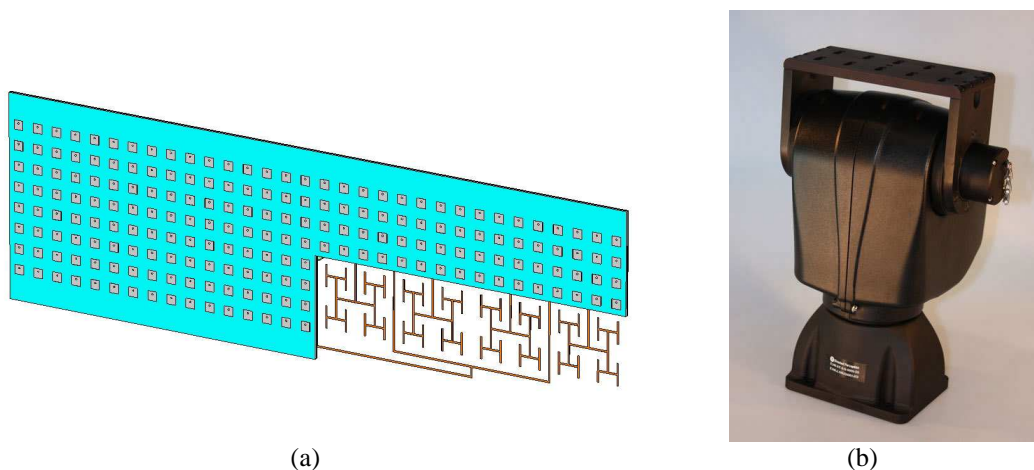


Fig. 56: SnowSAR system enhancements for future missions: (a) micorstrip array antenna with polarimetric capabilities and fan-beam radiation are under development for X- and Ku-bands (expected in September 2011); (b) Gimbal system now available at MetaSensing, characterized by rugged pan-tilt supports, multi-part payloads and internal wiring/slip-ring.

The availability of an accurate Digital Elevation Model (DEM) of the scenario under evaluation is an important tool, when the appropriate elevation angle needs to be determined for correction of the antenna gains in the antenna pattern synthesis process. The DEM of the monitored landscape is an additional way to minimize the radiometric errors.

For being sure of covering entirely the radar swath, the number of corner reflectors deployed on ground for external calibration should be increased. MetaSensing has ordered for additional corner reflectors. Furthermore, the number of flights planned above the area where the trihedral reflectors are deployed should also be increased, in order to have a higher availability of data. In particular, flights should be performed both at the beginning and at the end of the campaign.

At arctic latitudes, and particularly in the Baltic region, the magnetic declination must be taken into account, when orienting the trihedral reflectors with a magnetic compass. A 10° difference in the azimuth alignment of the reflectors may result in a loss of RCS and in an inhomogeneous RCS response across the swath.

Regarding the internal calibration, a good stability of the receiver gain has been demonstrated during the campaign. Since transmitted pulses are not generated when calibration pulses are used, the frequency of these lasts could be decreased, for example to one calibration pulse per second. In this way the influence of the receiving gain tracking on the acquisition process would be reduced.

Building a redundancy in the radar electronic equipment should be considered during the measurement campaigns. This would allow back-up solutions against possible failures. Of course, a trade-off between redundancy and cost cannot be avoided.

10 References

- [1] M. Davidson; *Technical assistance for the development and deployment of an X- to Ku-band mini-SAR airborne system - Statement of Work (SoW)*; ESA ref: EOP-SM/2100/MWJD-mwjd; Issue 2; Rev. 1; 22 Apr. 2010.
- [2] A. Meta, C. Trampuz; *Technical assistance for the development and deployment of an X- to Ku-band mini-SAR airborne system - Instrument Design and Testing Document*; MetaSensing ref. MS-SnowSAR-D1; Issue 1; 17 Nov. 2010.
- [3] A. Coccia, C. Trampuz, A. Meta; *Technical assistance for the development and deployment of an X- to Ku-band mini-SAR airborne system – Experiment Implementation Plan (with draft campaign report)*; MetaSensing ref. MS-SnowSAR-D4; Issue 1; 4 Apr. 2011.
- [4] M.L. Skolnik; *Introduction to radar system*, McGraw-Hill College; 2nd ed. 1980.
- [5] <http://www.ngdc.noaa.gov/geomagmodels/IGRFWMM.jsp>
- [6] F.T. Ulaby, M.C. Dobson, *Handbook of radar scattering statistics for terrain*, Artech House INC.; 1989.
- [7] <http://webone.novatel.ca/assets/Documents/Papers/SPAN-CPT.pdf>
- [8] J. Moreira, *Bewegungsextraktionsverfahren für Radar mit synthetischer Apertur*; Technische Universität München, München, Germany, p. 20, 1992. DLR Forschungsbericht DLR-FB 92-31.



METASENSING

**Technical Assistance for the Development and
Deployment of an X- and Ku- Band
MiniSAR Airborne System**

Data Set Description

Contract no.: 4000101697/10/NL/FF/ef

Doc. No.: MS-Snowsar-D7-Addendum

Issue: 4

Date: 30th October 2011

Authors:

Alex Coccia

Christian Trampuz

Ernesto Imbembo

Approved:

Adriano Meta

Index

1	Introduction.....	2
2	The SnowSAR system	3
2.1	Acquisition geometry.....	5
3	Data format	7
3.1	The Detected Image file.....	7
3.2	The Orbit file.....	7
3.3	The Orbit Image file.....	8
3.4	The Equivalent Number of Look (ENL) Image file	9
3.5	The Normalization Image file.....	10
3.6	Geotiff files	11
4	Digital Elevation Model (DEM)	12
4.1	The Digital Elevation Mode (DEM) file.....	13
5	SAR dataset.....	14
5.1	Corner reflectors	14
5.2	Data take description.....	16
	Table II – Acquisition details.....	17
5.2.1	Delivered files	18
	Table III – File details.....	19
5.2.2	Acquisition track Nr. 1	20
5.2.3	Acquisition track Nr. 2a.....	21
5.2.4	Acquisition track Nr. 2b.....	22
5.2.5	Acquisition track Nr. 20.....	23
5.2.6	Acquisition track Nr. 30.....	24
6	References.....	25
	Annex A - Source codes	26

1 Introduction

In the present document the description is given about the SnowSAR data takes performed in Finland during March 2011, within a measurement campaign in the framework the ESA's NoSREx (Nordic Snow Radar Experiment) extension project.

Particular attention is paid to the SnowSAR dataset format and to the routine files (Matlab codes) adopted for their processing. A number of different airborne SAR data takes at X- and Ku- bands relative to the Finnish measurement campaign is presented as example. Each data take has been processed up to a detected multilooked image and additional ancillary data. These are described in detail in this document. A step by step example description is also included, together with Matlab codes for reading the different type of data.

For convenience, some general information about the campaign is also summarized. However, for a detailed description of the SnowSAR system and for a broad characterization of the Finnish SnowSAR campaign the reader should refer to the previously released documentation [1]-[4].

Besides this introductory chapter, the remaining of this document is organized as follows.

In Chapter 2 the main SnowSAR system parameters are summarized, and the SnowSAR on-board system configuration during the acquisitions is described.

Chapter 3 provides the data format for some acquisition files used in the image processing phase.

Chapter 4 deals with the Digital Elevation Models adopted to perform the SAR processing on the acquired data.

Chapter 5 explores the details of the acquisition flights performed during the SnowSAR measurement campaign, with particular attention on those which are considered in this document; some processed images are given as examples.

Following the reference chapter, in the Annex A the Matlab source codes are finally given.

2 The SnowSAR system

In table I an overview is given summarizing important radar system parameters of the SnowSAR instrument.

Table 1 – Radar system parameters

PARAMETER	X-Band		Ku-Band	
Geometry				
Altitude [ft, m]	5500 / 1670			
Velocity [kn]	~ 80			
Antenna (one way single pol)				
	V	H	V	H
Elevation aperture [°]	12	17	8	12
Azimuth aperture [°]	17	12	12	8
Waveform				
Modulation	FMCW			
Polarization mode	VV/VH		VV/VH	
Peak power [W]	1		1	
Actual PRF [Hz]	1400		1400	
Sampling rate [MHz]	25		25	
Bandwidth [MHz]	100		100	
Processed wavelength [m]	0.0313		0.0174	
Processed bandwidth [MHz]	95		95	
Range pixel spacing [m]	2		2	
Azimuth pixel spacing [m]	2		2	
Near ground range [m]	850		850	

The SnowSAR system has been installed inside the fuselage of a Cessna 208B, the same adopted during the testing phase in the Netherlands in February 2011, see Figure 1. Besides the capability of flying with icing conditions, an important feature of this kind of airplane is given by its big side cargo door: this offers a considerable un-obstructed aperture for

mounting the radar antennas away from the wings without the modification of the structure and of the aerodynamic profile of the airplane.



Figure 1. SnowSAR airborne platform, a Cessna 208 Grand Caravan from the National Paracentrum Teuge.

Four standard-gain horn dual polarimetric antennae are used by the SnowSAR: 2 for X-band (1 transmitting and 1 receiving antenna) and 2 for the Ku-band (1 transmitting and 1 receiving antenna). They have been mounted on a dedicated structure, allowing a pointing direction in the elevation plane (look angle) of 40° . A Lexan polycarbonate layer protects the antennae from the draughty flying conditions. The SnowSAR antennae set-up on board of the aircraft is sketched in Figure 2, where lengths are given in centimetres. Figure 2 (a) shows the antennae configuration on the mounting frame. For each of the two bands, X and Ku, both the transmitting (TX) and receiving (RX) antennae are shown, together with their (square) aperture dimension and relative spacing. This configuration has been chosen (based on antennae coupling minimization) among different options which have been tried during the testing phase in Teuge.

A dedicated GPS-IMU integrated system (Novatel SPAN-CPT) has been installed on board of the airplane for high-accuracy trajectory reconstruction by post-processing techniques.

Figure 2 (b) represents a top view of the tail of the aircraft, where the distances between IMU unit and antenna mounting frame can be appreciated. It has to be noted how the pointing direction of the SnowSAR antennas onboard the aircraft were not perpendicular to the direction of flight: an estimated squint angle of 5° toward the rear of the airplane is

introduced, to follow the shape of the airplane fuselage and to minimize the blockage of the luggage door and of the airplane floor.

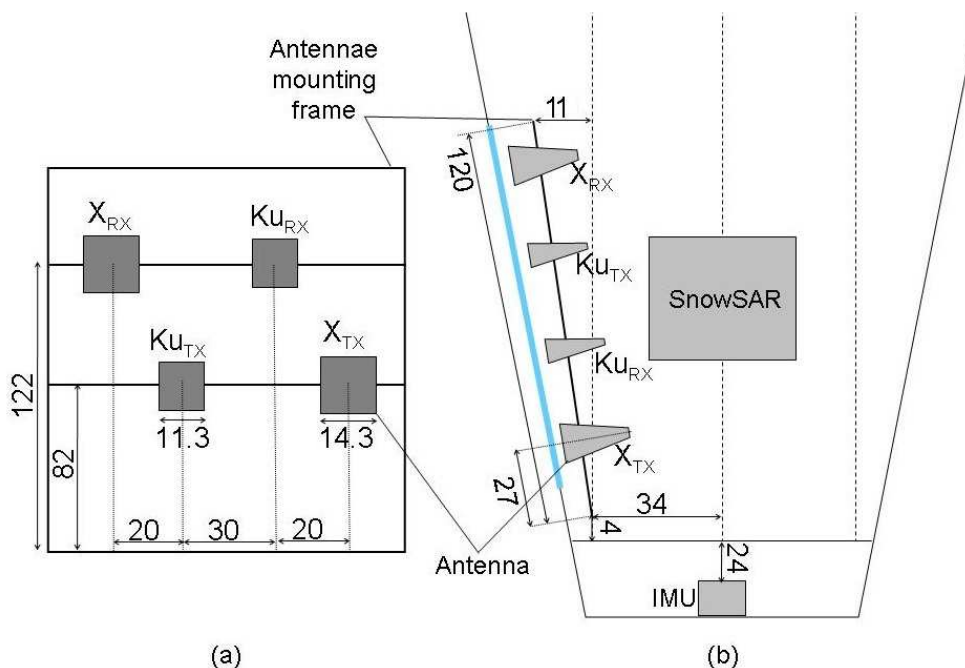


Figure 2. SnowSAR antennae set up on board the aircraft: (a) mounting configuration from a side view; (b) top view of the tail of the aircraft, where displacement between SnowSAR antennae and IMU can be estimated. Dimensions are in cm.

2.1 Acquisition geometry

In Figure 3 the acquisition geometry is represented for the Finnish SnowSAR campaign. On board of the Cessna 208 the SnowSAR system is characterized by a left-side observation angle; as mentioned, the antennae are mounted to look at an angle of 40° with respect to nadir direction. The designed aircraft altitude during acquisitions is 5500 ft (ca. 1,7 Km). This results in a distance from Nadir of about 4600 ft (ca. 1.4 km) of the antenna pointing direction. The actual radar swath width depends on the considered frequency, having the X

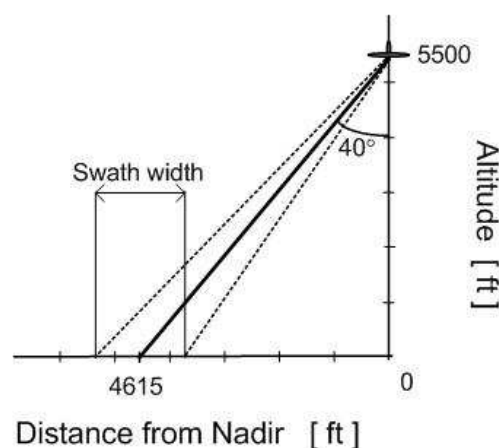


Figure 3. SnowSAR acquisition geometry.

band sub-system a larger antenna patterns than the Ku band one. However, a swath width of about 500 metres can be conveniently considered for both the frequencies bands.

3 Data format

The following describes the format of the delivered data.

3.1 The Detected Image file

The *Detected Image* file contains the processed multilooked image geocoded on a UTM grid.

The file starts with a header followed by the actual data. The file structure is:

ny	int16	the number of elements per range line
dy_ml	double	the pixel spacing (in meter) along the cross-track direction (ground range direction)
y0_ml	double	ground range value (in meter) of the first range element
dx_ml	double	the pixel spacing (in meter) along the along-track direction (azimuth direction)
x0_ml	double	azimuth value (in meter) of the first azimuth element
Zone_UTM_ml	double	UTM zone number of the UTM grid
Emisphere_UTM_ml	double	Earth Emisphere (0 for North, 1 for South)
UTM_0_0_x_ml of	double	UTM easting coordinate of the first element of the image
UTM_0_0_y_ml	double	UTM northing coordinate of the first element of the image
orbit_heading_ml	double	orientation in the UTM grid of the geocoded image
det_image_ml	single	multilooked detected image [values in dB]

3.2 The Orbit file

The *Orbit* file contains the time, position and attitude of the antenna phase centre during the whole data take. It is arranged as an array of structures:

time	double	GPS time - [seconds]
x	double	x coord. in the local reference system [m]
y	double	y coord. in the local reference system [m]
z	double	z coord. in the local reference system [m]
yaw	double	yaw in the local reference system [rad]

pitch	double	pitch in the local reference system [rad]
roll	double	roll in the local reference system [rad]

3.3 The Orbit Image file

The *Orbit Image* file provides the index information of the orbit file corresponding to the position within the trajectory where each pixel of the detected multilooked image has been focused. The file has the same structure as the *Detected Image* file and it contains a matrix with the same dimension as the detected multilooked image. By reading a value in the *Orbit Image* file, one can interpolate for the corresponding position and attitude value. The file format is:

ny	int16	number of elements per range line
dy_ml	double	pixel spacing (in meter) along the cross-track direction (ground range direction)
y0_ml	double	ground range value (in meter) of the first range element
dx_ml	double	the pixel spacing (in meter) along the along-track direction (azimuth direction)
x0_ml	double	azimuth value (in meter) of the first azimuth element
Zone_UTM_ml	double	UTM zone number of the UTM grid
Emisphere_UTM_ml	double	Earth Hemisphere (0 for North, 1 for South)
UTM_0_0_x_ml	double	UTM easting coordinate of the first element of the image
UTM_0_0_y_ml	double	UTM northing coordinate of the first element of the image
orbit_heading_ml	double	orientation in the UTM grid of the geocoded image
orb_image_ml	single	orbit image [GPS time in second]

3.4 The Equivalent Number of Look (ENL) Image file

The *Equivalent Number of Look (ENL)* Image file contains the calculated ENL derived directly from the intensity of the SAR image. The ENL depends on the averaged area, in this case 10x10 meter, and by the homogeneity of the imaged area.

ny	int16	the number of elements per range line
dy_ml	double	the pixel spacing (in meter) along the cross-track direction (ground range direction)
y0_ml	double	ground range value (in meter) of the first range element
dx_ml	double	the pixel spacing (in meter) along the along-track direction (azimuth direction)
x0_ml	double	azimuth value (in meter) of the first azimuth element
Zone_UTM_ml	double	UTM zone number of the UTM grid
Emisphere_UTM_ml	double	Earth Emisphere (0 for North, 1 for South)
UTM_0_0_x_ml	double	UTM easting coordinate of the first element of the image
UTM_0_0_y_ml	double	UTM northing coordinate of the first element of the image
orbit_heading_ml	double	orientation in the UTM grid of the geocoded image
ENL_ml	single	Equivalent Number of Looks image

3.5 The Normalization Image file

The normalization factor image file is related to the back projection processing. The matrix contains the number of pulses used for focusing a certain pixel weighted by the processing windows.

ny	int16	the number of elements per range line
dy_ml	double	the pixel spacing (in meter) along the cross-track direction (ground range direction)
y0_ml	double	ground range value (in meter) of the first range element
dx_ml	double	the pixel spacing (in meter) along the along-track direction (azimuth direction)
x0_ml	double	azimuth value (in meter) of the first azimuth element
Zone_UTM_ml	double	UTM zone number of the UTM grid
Emisphere_UTM_ml	double	Earth Emisphere (0 for North, 1 for South)
UTM_0_0_x_ml of	double	UTM easting coordinate of the first element of the image
UTM_0_0_y_ml	double	UTM northing coordinate of the first element of the image
orbit_heading_ml	double	orientation in the UTM grid of the geocoded image
norm_ml	single	Equivalent Number of Looks image

3.6 GeoTIFF files

Some of the information delivered in the previous described format is also delivered in a GeoTIFF format for easy interpretation and comparison with other geographic data.

The TIFF standard used is the one according to revision 6.0 [6].

The GeoTIFF fields are encoded as described in the guidelines of www.remotesensing.org.

The GeoTIFF files relative to the SAR images contains data encoded as unsigned integer with 8 bits: 0 corresponds to -40 dBm^2 , 255 corresponds to 20 dBm^2 , linearly and uniformly spaced.

The GeoTIFF file relative to the DEM contains data encoded as signed integer with 16 bits. The data unit is decimeter.

4 Digital Elevation Model (DEM)

In order to perform the SAR processing on the acquired data, Digital Elevation Models (DEMs) of the observed area have been used. These have been obtained from the National Land Survey of Finland (NLS) [5]. The DEMs are originated from laser scanning data acquired in 2010 with a pixel spacing of 2 meters; the elevation accuracy is estimated up to 15 centimetres. In Figure 4 an example is given of such a DEM. The original coordinate system is ETRS-TM35FIN; for convenience it has been transformed in WGS84 geographic (Lat, Lon) during the SAR processing.

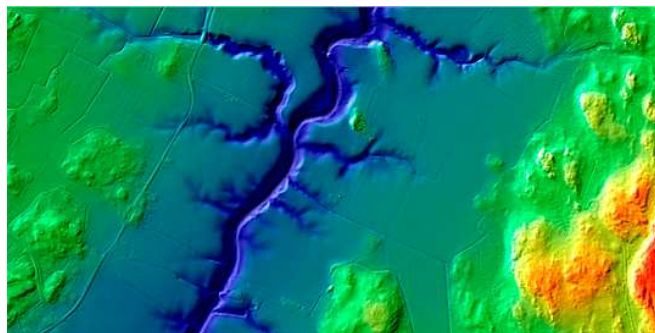


Figure 4. Example of a 2 meter grid DEM purchased from NLS.

Next Figure 5 shows the overlapping among the SnowSAR acquisition area during the measurement campaign (in yellow), and the available data coverage for the NLS DEM (squared map), i.e. the area U4344, blocks C, D, E, F.



Figure 5. Overlapping between SnowSAR data (yellow rectangle) and the available DEM data (square map).

4.1 The Digital Elevation Mode (DEM) file

The *Digital Elevation Model (DEM)* file contains the DEM used for the SAR processing of the data. The structure of the file is similar to that of the *Detected Image* file. The DEM matrix has the same dimension of the multilooked Detected Image. The file structure is:

ny	int16	the number of element per range line
dy_ml	double	the pixel spacing (in meter) along the cross-track direction (ground range direction)
y0_ml	double	ground range value (in meter) of the first range element
dx_ml	double	the pixel spacing (in meter) along the along-track direction (azimuth direction)
x0_ml	double	azimuth value (in meter) of the first azimuth element
Zone_UTM_ml	double	UTM zone number of the UTM grid
Emisphere_UTM_ml	double	Earth Emisphere (0 for North, 1 for South)
UTM_0_0_x_ml	double	UTM easting coordinate of the first element of the image
UTM_0_0_y_ml	double	UTM northing coordinate of the first element of the image
orbit_heading_ml	double	orientation in the UTM grid of the geocoded image
DEM	single	DEM [meter, over WGS84 ellipsoid]

5 SAR data set

The first measurement campaign for the SnowSAR system has been performed in Lapland, Finland, in March 2011. In this period the Lappish landscape is still covered by winter snows and temperatures are below zero for most of the day. In Figure 6 an aerial view of the town of Rovaniemi, capital of Lapland, is depicted, shot during a validation flight within the SnowSAR campaign. As it can be appreciated even rivers and water basins are still frozen and covered by snow.



Figure 6. Aerial view of Rovaniemi, Finland, shot during a test-validation flight on the 13th of March 2011, first operational day of the SnowSAR measurement campaign.

MetaSensing operational base has been set in the Rovaniemi airport. The acquisition area for the SnowSAR measurements is about 100 Km more on the North, on an area close to the town of Sodankyla (where the Artic Research Centre, ARC of the Finnish Meteorological Institute, FMI, is located), between the river Kitinen and the lake Orajarvi. In Figure 5. Overlapping between SnowSAR data (yellow rectangle) and the available DEM data (square map). the zone interested by the SnowSAR acquisition campaign is shown as a yellow area on a Google Earth image: it measures about 60 Km² and it mainly consists of open and forest bogs.

5.1 Corner reflectors

For purposes of in-flight antenna characterization and radar calibration, 4 trihedral reflectors have been used during the campaign. The side of the square face is 30 cm long, resulting in a

RCS in excess of 20 dBm^2 at X-band and of 25 dBm^2 at Ku-band. They have been deployed by FMI in proximity of the ARC in Sodankyla, in correspondence of the acquisition strip number 2. The four corner reflectors have been placed on the following points (decimal coordinates)

#1: 67.3612 N, 26.6303 E

#3: 67.3606 N, 26.6314 E

#2: 67.3622 N, 26.6292 E

#4: 67.3616 N, 26.6292 E

Their deployment is represented in Figure 7, where the FMI-ARC centre can be also located; in the figure the yellow strip represents the ideal SAR coverage for the acquisition flight Nr. 2, see Figure 8. The trihedral reflectors on the ground were oriented azimuthally to maximize their RCS in the direction that is orthogonal to the flight track. However, due to magnetic declination phenomenon, a 10° offset rotation resulted, of the direction of maximum RCS with respect to the direction that was orthogonal to the flight track. When accommodated on the terrain covered in snow and ice, the corner reflectors were affected by minor misalignments, such as a roll tilt and a pitch tilt of the free-vertex, with respect to the surface of deployment. The roll and pitch tilts were measured respectively $0^\circ (+/-1^\circ)$ and $1.5^\circ (+/-1^\circ)$ nose-up.



Figure 7. Trihedral corner reflectors displacement during the SnowSAR campaign on the 15th of March.

5.2 Data take description

With the geometry previously described in paragraph 2.1, the desired acquisition area (see Figure 5) has been covered with 20 parallel and contiguous acquisition flights, each track being around 7.5 Km long, performed from South to North. Additionally, two acquisition flights have been performed in a direction perpendicular to the other 20, flown from East to West [3].

Among more than 30 data takes performed during the entire measurement campaign, in the present document four acquisition strips are taken into account, performed during the campaign on the 15th of March 2011. Namely, transects nr. 1, nr. 2 (passing by the SnowScat site) and nr. 20 (passing by the lake site); and the number 30 (passing by the SnowScat site, perpendicular to the others). Figure 8 shows the ideal ground stripes. The width of each one measures 500 metres. Table II provides some more details about the considered acquisitions.

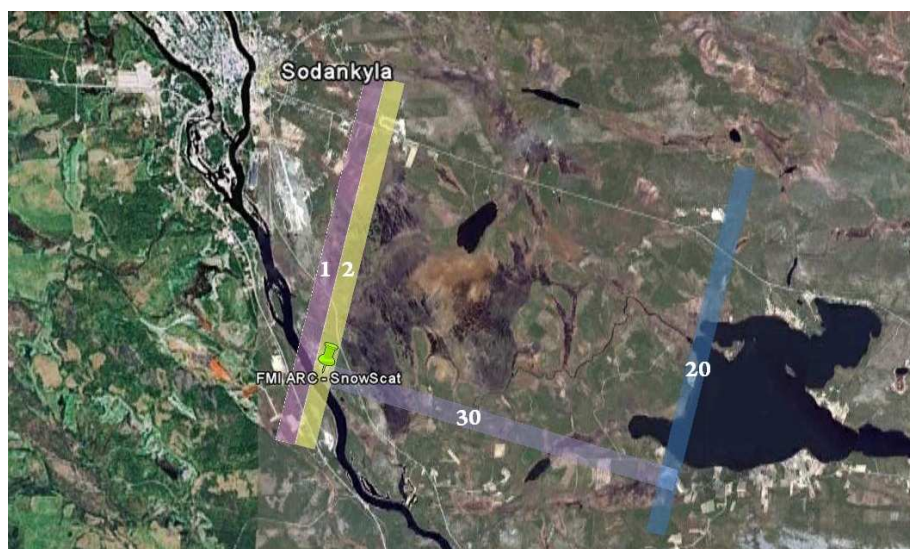


Figure 8. Operational area for the SnowSAR campaign, from Google Earth: ideal land SnowSAR coverage during five different acquisitions, namely nr.1, nr.2, nr. 4, nr. 20 and nr. 30, performed on the 15th of March.

Table II – Acquisition details

Flight ID	Acquisition time	Freq. Band / Polarimetry	Details	Acquisition file ID
2a	7.50	X , Ku / VV, HV	SnowSCAT IOA + Corners	055237
2b	8.02	X, Ku / VV, HV	SnowSCAT IOA + Corners	060210
20	8.24	X , Ku / VV, HV	Lake site: 178-182 (R1)	062415
30	8.30	X , Ku / VV, HV	SnowSCAT IOA; 144-159 (R1)	063249
1	8.50	X , Ku / VV, HV	--	065130

Table 2: SnowSAR measurement campaign on the 15th of March. The ‘acquisition time’ column refers to the beginning of the SnowSAR acquisition, expressed in local time. On the ‘Details’ column the potential overlapping of SnowSAR airborne data with ground measurements performed by the FMI.

5.2.1 Delivered files

The delivered data are relative to five acquisitions. For each acquisition there are four images, VV and HV at X and Ku band. The data for each image are collected in a RAR file, for a total of 20 RAR files.

The list of the zip files is

- 20110315055237_XVV.rar
- 20110315055237_XHV.rar
- 20110315055237_KVV.rar
- 20110315055237_KHV.rar

- 20110315060210_XVV.rar
- 20110315060210_XHV.rar
- 20110315060210_KVV.rar
- 20110315060210_KHV.rar

- 20110315062415_XVV.rar
- 20110315062415_XHV.rar
- 20110315062415_KVV.rar
- 20110315062415_KHV.rar

- 20110315063249_XVV.rar
- 20110315063249_XHV.rar
- 20110315063249_KVV.rar
- 20110315063249_KHV.rar

- 20110315065130_XVV.rar
- 20110315065130_XHV.rar
- 20110315065130_KVV.rar
- 20110315065130_KHV.rar

The following table describes the contents of the 20110315055237_XVV.rar file. The other RAR files have similar content.

Table III – File details

File name	Description
MSAR_ML_dem_20110315055237_XVV.dat	<i>DEM matrix (section 4.1)</i>
MSAR_ML_enl_20110315055237_XVV.dat	<i>ENL matrix (section 3.4)</i>
MSAR_ML_image_20110315055237_XVV.dat	<i>SAR detected image (section 3.1). The image is delivered with a 2x2 meter pixel spacing</i>
MSAR_ML_image_10x10_20110315055237_XVV.dat	<i>SAR detected image (section 3.1). The image is delivered with a 10x10 meter pixel spacing</i>
MSAR_ML_image_not_masked_20110315055237_XVV.dat	<i>SAR detected image (section 3.1). The image is delivered with a 2x2 meter pixel spacing without masking of higher elevation angle. This image is not to be used for calibration analysis in the extended areas. Use the previous two delivered images for calibration analysis</i>
MSAR_ML_norm_20110315055237_XVV.dat	<i>Normalization Image (section 3.4)</i>
MSAR_ML_orbit_20110315055237_XVV.dat	<i>Orbit Image (section 3.3)</i>
orbit_20110315055237.dat	<i>Orbit file (section 3.2)</i>
MSAR_ML_geotiff_20110315055237_XVV.tiff	<i>GeoTIFF file of corresponding detected image (section 3.6)</i>
MSAR_ML_10x10_geotiff_20110315055237_XVV.tiff	<i>GeoTIFF file of corresponding detected image (section 3.6)</i>
MSAR_ML_not_masked_geotiff_20110315055237_XVV.tiff	<i>GeoTIFF file of corresponding detected image (section 3.6)</i>
MSAR_DEM_geotiff_20110315055237_XVV.tiff	<i>GeoTIFF file of DEM (section 3.6)</i>
DEM_20110315055237_XVV.tif	<i>Illustrative TIF image of the DEM</i>

Table 3. Description of the files associated to each acquisition.

5.2.2 Acquisition track Nr. 1

Transect nr. 1 is the most western ground



Figure 9. Ideal ground strip coverage for SnowSAR acquisition flight Nr. 1.

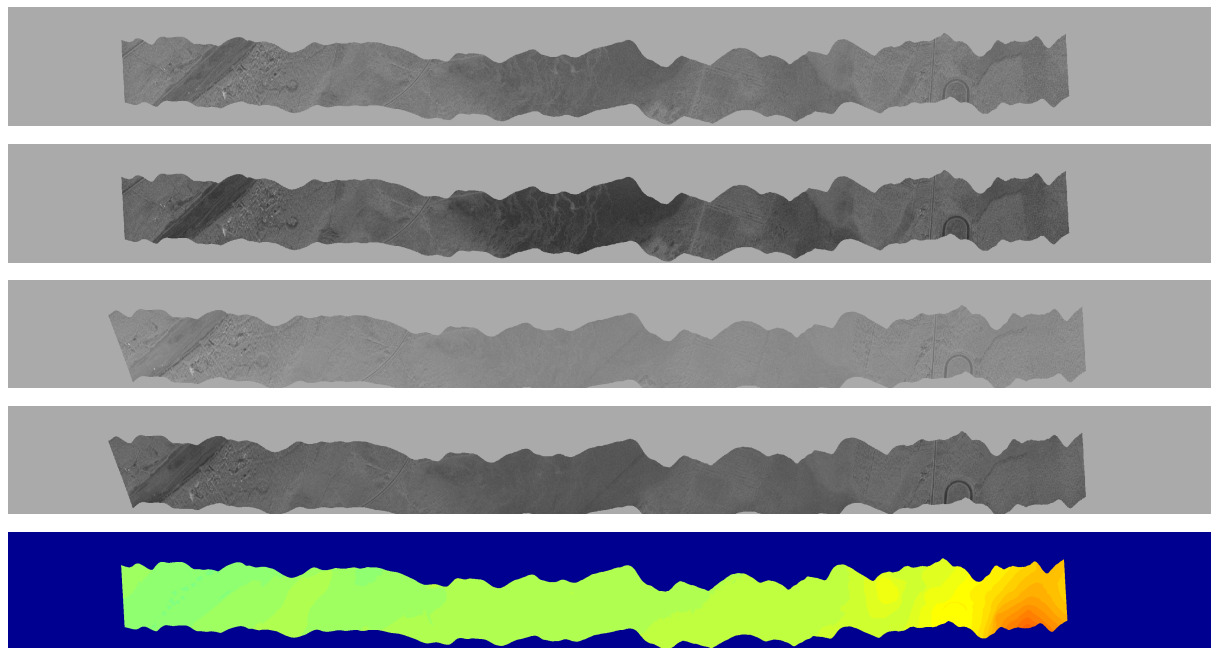


Figure 10. SnowSAR images for transect Nr. 1. Up: X-Band (VV, VH); down: Ku-band (VV, VH) and corresponding DEM

5.2.3 Acquisition track Nr. 2a

As already mentioned, the acquisition track number 2 is of particular relevance because of two reasons: firstly, the calibration reflectors have been placed within its ground swat; secondly, it represents an acquisition track in correspondence of which the FMI-ARC is located, with an Intensive Observation Point (IOP) for ground measurements, at the SnowSCAT site.

Figure 10, taken from Google Earth TM gives an overview of the ideal ground swat for transect nr. 2. In Figure 12 the polarimetric X and Ku images, and the DEM of the same area are depicted. From the DEM, the topography of the monitored area can be appreciated, whereas a difference in altitude of more than 50 meters can be noticed in the right part of the DEM, with respect to the rest of the considered area.



Figure 11. Ideal ground strip coverage for SnowSAR acquisition flight Nr. 2.

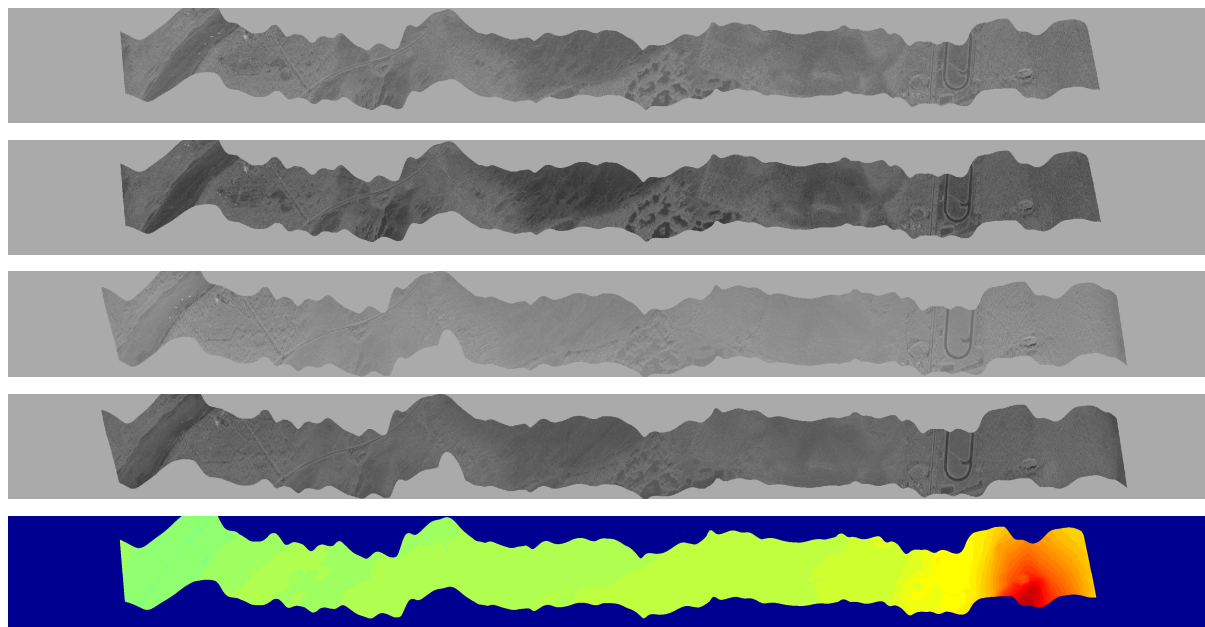


Figure 12. SnowSAR images for transect Nr. 2a. Up: X-Band (VV, VH); down: Ku-band (VV, VH) and corresponding DEM.

5.2.4 Acquisition track Nr. 2b

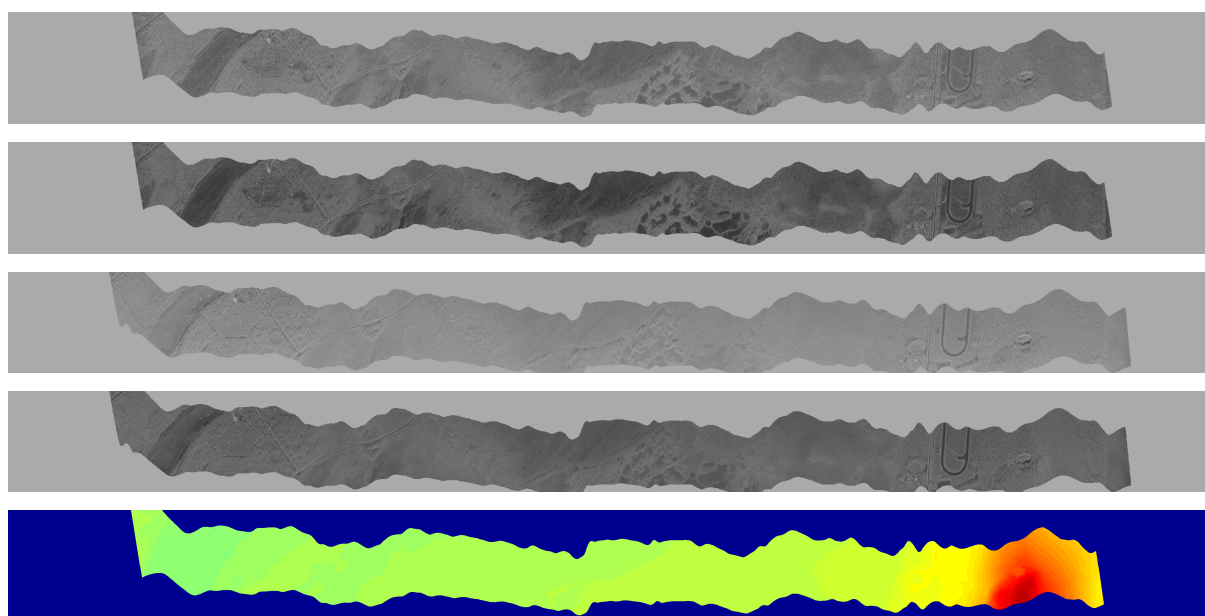


Figure 13. SnowSAR images for transect Nr. 2b. Up: X-Band (VV, VH); down: Ku-band (VV, VH) and corresponding DEM.

5.2.5 Acquisition track Nr. 20

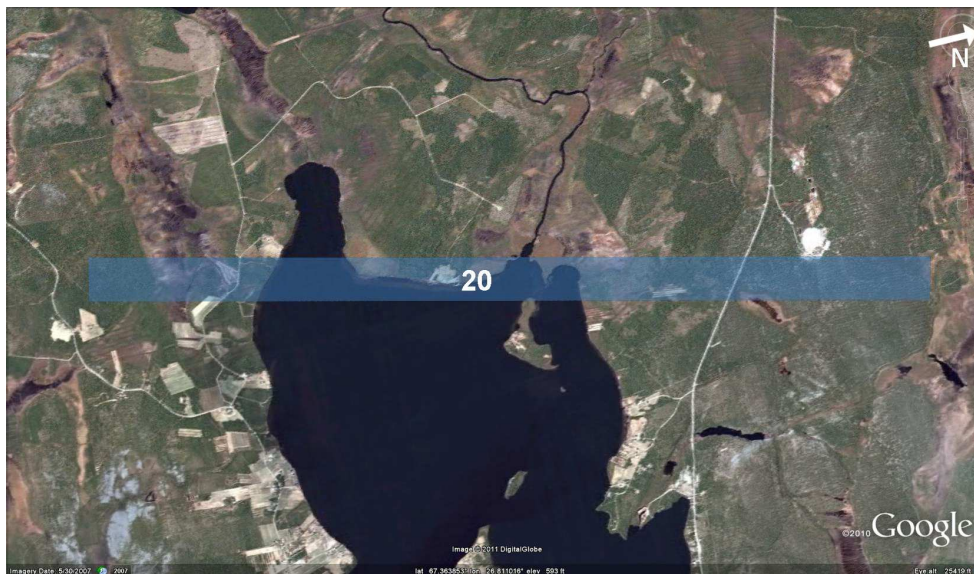


Figure 14. Ideal ground strip coverage for SnowSAR acquisition flight Nr. 20.

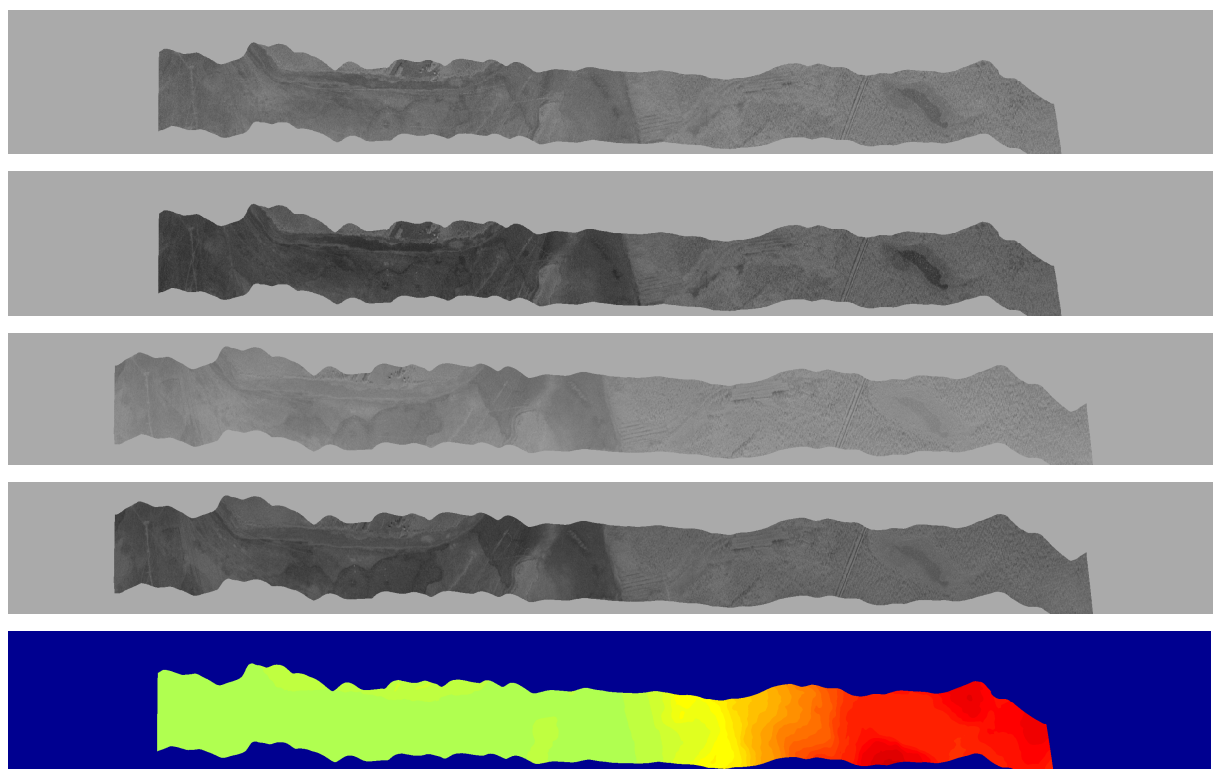
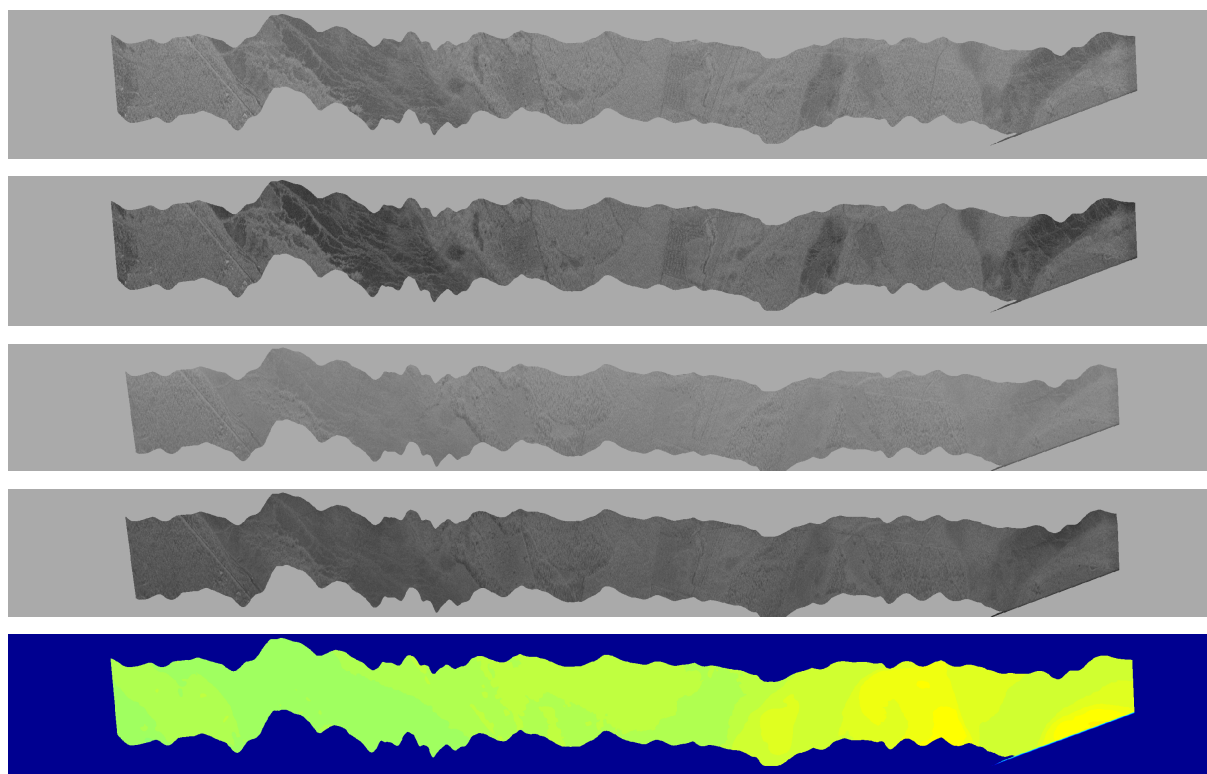


Figure 15. SnowSAR images for transect Nr. 20. Up: X-Band (VV, VH); down: Ku-band (VV, VH) and corresponding DEM.

5.2.6 Acquisition track Nr. 30

Figure 16. Ideal ground strip coverage for SnowSAR acquisition flight Nr. 30.

Figure 17. SnowSAR images for transect Nr. 30. Up: X-Band (VV, VH); down: Ku-band (VV, VH) and corresponding DEM.

	Data Set Description	Page 25 of 33
---	----------------------	---------------

6 References

- [1] M. Davidson; *Technical assistance for the development and deployment of an X- to Ku-band mini-SAR airborne system - Statement of Work (SoW)*; ESA ref: EOP-SM/2100/MWJD-mwjd; Issue 2; Rev. 1; 22 Apr. 2010.
- [2] A. Meta, C. Trampuz; *Technical assistance for the development and deployment of an X- to Ku-band mini-SAR airborne system - Instrument Design and Testing Document*; MetaSensing ref. MS-SnowSAR-D1; Issue 1; 17 Nov. 2010.
- [3] A. Coccia, C. Trampuz, A. Meta; *Technical assistance for the development and deployment of an X- to Ku-band mini-SAR airborne system – Experiment Implementation Plan (with draft campaign report)*; MetaSensing ref. MS-SnowSAR-D4; Issue 1; 4 Apr. 2011.
- [4] C. Trampuz, A. Coccia, E. Imbembo, A. Meta; *Technical assistance for the development and deployment of an X- to Ku-band mini-SAR airborne system – Final Report*; MetaSensing ref. MS-SnowSAR-D7; Issue 1; 11 Jul. 2011.
- [5] <http://www.maanmittauslaitos.fi/en>
- [6] <http://partners.adobe.com/public/developer/en/tiff/TIFF6.pdf>

Annex A - Source codes

`read_det_image.m` Function to read multilooked data

```
clear all;

FileName_DET = 'MSAR_ML_image20110315055237_32_VV.dat'

InputFileName_DET = fopen(FileName_DET, 'r');

if InputFileName_DET == -1
    disp([FileName_DET, ' could not be opened']);
    output_status = -1;
    return ;
end

ny = fread(InputFileName_DET, 1, 'int16')
dy = fread(InputFileName_DET, 1, 'double')
y0 = fread(InputFileName_DET, 1, 'double')
dx = fread(InputFileName_DET, 1, 'double')
x0 = fread(InputFileName_DET, 1, 'double')
Zone_UTM = fread(InputFileName_DET, 1, 'double');
Emisphere_UTM = fread(InputFileName_DET, 1, 'double');
UTM_0_0_x = fread(InputFileName_DET, 1, 'double')
UTM_0_0_y = fread(InputFileName_DET, 1, 'double')
orbit_heading = fread(InputFileName_DET, 1, 'double')

[det_image sample_count] = fread(InputFileName_DET, [ny inf], 'single');

if sample_count == 0
    output_status = -2;
    return ;
end

fclose('all');

[ny nx] = size(det_image);

axis_y = [0:ny-1]*dy + y0;
axis_x = [0:nx-1]*dx + x0;

figure(46363);
imagesc(axis_x, axis_y, det_image);
title('SAR image');
xlabel('Along track - [m]');
ylabel('Cross track - [m]');
axis equal;
colorbar;
```

read_DEM_image.m

Function to read DEM data

```
clear all;

root      = '';
FileName  = 'MSAR_ML_dem20110315055237_32_VV.dat';
FileName_DEM = [root, FileName];

InputFileName_DEM = fopen(FileName_DEM, 'r');

if InputFileName_DEM == -1
    disp([FileName_DEM, ' not found']);
    output_status = -1;
    return ;
end

ny      = fread(InputFileName_DEM, 1, 'int16');
dy      = fread(InputFileName_DEM, 1, 'double');
y0      = fread(InputFileName_DEM, 1, 'double');
dx      = fread(InputFileName_DEM, 1, 'double');
x0      = fread(InputFileName_DEM, 1, 'double');
Zone_UTM      = fread(InputFileName_DEM, 1, 'double');
Emisphere_UTM = fread(InputFileName_DEM, 1, 'double');
UTM_0_0_x     = fread(InputFileName_DEM, 1, 'double');
UTM_0_0_y     = fread(InputFileName_DEM, 1, 'double');
orbit_heading = fread(InputFileName_DEM, 1, 'double');

[dem_image sample_count] = fread(InputFileName_DEM, [ny inf], 'single');
if sample_count == 0
    output_status = -2;
    return ;
end

fclose('all');

[ny nx] = size(dem_image);

axis_y = [0:ny-1]*dy + y0;
axis_x = [0:nx-1]*dx + x0;

figure(46363);
imagesc(axis_x, axis_y, dem_image);
title('DEM');
xlabel('Along track - [m]');
ylabel('Cross track - [m]');
axis equal;
colorbar;
```

read_orbit.m Function to read orbit file

```
clear all;

FileName      = 'orbit_20110315055237_32.dat'
text_FileName = [root, 'orbit_', FileName]
fid_orbit     = fopen(text_FileName, 'r');

if fid_orbit == -1
    disp([text_FileName, ' could not be opened'])
    return;
end

matrix = fread(fid_orbit, [7, inf], 'double');

% in the 'matrix' the rows report:
% [t_a, x_a, y_a, z_a, yaw_a, pitch_a, roll_a]

fclose(fid_orbit);

t_a = matrix(1,:);      % given in GPS seconds
x_a = matrix(2,:);
y_a = matrix(3,:);
z_a = matrix(4,:);

yaw_deg_a  = matrix(5,:)*180/pi;
pitch_deg_a = matrix(6,:)*180/pi;
roll_deg_a  = matrix(7,:)*180/pi;

figure(3241);
plot3(x_a, y_a, z_a);
grid on
xlabel('Along track - [m]');
ylabel('Cross track - [m]');
zlabel('Height - [m]');
```

read_geometry.m Example for retrieving elevation angle and other geometry information

```
clear all;

FileName_DET = 'MSAR_ML_image20110315055237_32_VV.dat';
FileName_DEM = 'MSAR_ML_dem20110315055237_32_VV.dat';
FileName_ORB = 'MSAR_ML_orbit20110315055237_32_VV.dat';
FileName_orbit = 'orbit_20110315055237_32.dat';

root_proc = [];

InputFileID_ML = fopen([root_proc, FileName_DET], 'r');
InputFileID_ORB = fopen([root_proc, FileName_ORB], 'r');
InputFileID_DEM = fopen([root_proc, FileName_DEM], 'r');
fid_orbit = fopen([root_proc, FileName_orbit], 'r');

MIN_VAL_DET = -80;

READ_FLAG = 0;
nx = 0;

ny = fread(InputFileID_ML, 1, 'int16');
dy = fread(InputFileID_ML, 1, 'double');
y0 = fread(InputFileID_ML, 1, 'double');
dx = fread(InputFileID_ML, 1, 'double');
x0 = fread(InputFileID_ML, 1, 'double');
Zone_UTM = fread(InputFileID_ML, 1, 'double');
Emisphere_UTM = fread(InputFileID_ML, 1, 'double');
UTM_0_0_x = fread(InputFileID_ML, 1, 'double');
UTM_0_0_y = fread(InputFileID_ML, 1, 'double');
orbit_heading = fread(InputFileID_ML, 1, 'double');

if ~READ_FLAG

    while 1
        temp_pos = fseek(InputFileID_ML, ny*4, 0);
        if temp_pos == -1
            break;
        end
        nx = nx + 1;
    end
    fseek(InputFileID_ML, 74, -1);
    READ_FLAG = 1;
end

fseek(InputFileID_ORB, 74, -1);
fseek(InputFileID_DEM, 74, -1);

x_ax = min(x0):dx:max(x0 + dx.*(nx-1));
pos_val = [];

[det_image sample_count] = fread(InputFileID_ML, [ny inf], 'single');
% continues on next page
```



```
% continues from previous page
x_ac = zeros(ny, nx);
y_ac = zeros(ny, nx);
z_ac = zeros(ny, nx);

el_ang = zeros(ny, nx);
az_ang = zeros(ny, nx);
look_ang = zeros(ny, nx);

fd_mat = zeros(ny, nx);

x_ac(pos_val) = orbit_ac(2, pos_orbit);
y_ac(pos_val) = orbit_ac(3, pos_orbit);
z_ac(pos_val) = orbit_ac(4, pos_orbit);

r(pos_val) = sqrt( (orbit_ac(2, pos_orbit).' - im_x(pos_val)).^2 +
                  (orbit_ac(3, pos_orbit).' - im_y(pos_val)).^2 +
                  (orbit_ac(4, pos_orbit).' - dem_image(pos_val)).^2 );

r_zy(pos_val) = sqrt( (orbit_ac(3, pos_orbit).' - im_y(pos_val)).^2 +
                    (orbit_ac(4, pos_orbit).' - dem_image(pos_val)).^2 );

el_ang(pos_val) = acos((orbit_ac(4, pos_orbit).' -
                      dem_image(pos_val))./r(pos_val)) - orbit_ac(7,
                      pos_orbit).');

az_ang(pos_val) = atan(( im_x(pos_val) - orbit_ac(2,
                      pos_orbit).') ./ r_zy(pos_val)) - orbit_ac(5, pos_orbit).');

look_ang(pos_val) = atan(( im_y(pos_val) - orbit_ac(3,
                      pos_orbit).') ./ r_zy(pos_val));

output_status = 1;

az_n_min = 1;
az_n_max = nx;
deg_el_min = 38;
deg_el_max = 42;
deg_az_min = -10;
deg_az_max = 10;
y_ac_min = -25;
y_ac_max = 25;

mask_el = (el_ang(:,az_n_min:az_n_max,1)*180/pi > deg_el_min) &
          (el_ang(:,az_n_min:az_n_max,1)*180/pi < deg_el_max);

mask_az = (az_ang(:,az_n_min:az_n_max,1)*180/pi > deg_az_min) &
          (az_ang(:,az_n_min:az_n_max,1)*180/pi < deg_az_max);

mask_ya = (y_ac(:,az_n_min:az_n_max,1) > y_ac_min) &
          (y_ac(:,az_n_min:az_n_max,1) < y_ac_max);

mask = mask_el.*mask_az.*mask_ya;

nsi = 5;
```

```
% continues on next page
```

```

% continues from previous page
figure(100);
fs1 = subplot(nsi,1,1);
imagesc(det_image(:,az_n_min:az_n_max).*mask);
caxis([-10 10]);
title(fs1, 'Intensity image - [dB]');
colorbar

fs2 = subplot(nsi,1,2);
imagesc(el_ang(:,az_n_min:az_n_max)*180/pi.*mask);
title(fs2, 'Elevation angle - [deg]');
colorbar

fs3 = subplot(nsi,1,3);
imagesc(look_ang(:,az_n_min:az_n_max)*180/pi.*mask);
title(fs3, 'Look angle - [deg]');
colorbar

fs4 = subplot(nsi,1,4);
imagesc(az_ang(:,az_n_min:az_n_max)*180/pi.*mask);
title(fs4, 'Azimuth angle - [deg]');
colorbar

fs5 = subplot(nsi,1,5);
imagesc(y_ac(:,az_n_min:az_n_max).*mask);
title(fs5, 'Cross track trajectory - [m]');
colorbar

```

An example of images generated by this last program is given in the following Figure

